Modelling and Simulation of a Multifunctional PV Electrochemical Storage System

by

Ali Tayyebi Khameneh

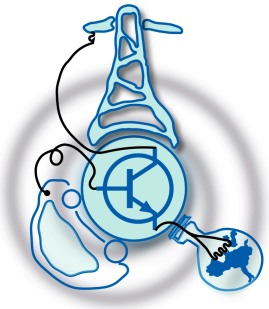

Submitted to the Department of Electrical Engineering, Electronics, Computers and Systems
in partial fulfillment of the requirements for the degree of

Erasmus Mundus Master Course in Sustainable Transportation and Electrical Power Systems

at the

UNIVERSIDAD DE OVIEDO

September 2016

Author .....

Certified by .....
Pablo García Fernández
Associate Professor at University of Oviedo
Thesis Supervisor

Certified by .....
Johann Mayr
Junior Research Engineer at Austrian Institute of Technology (AIT)
Thesis Supervisor

Modelling and Simulation of a Multifunctional PV Electrochemical Storage System

by

Ali Tayyebi Khameneh

Submitted to the Department of Electrical Engineering, Electronics, Computers and Systems
on 1st of September 2016, in partial fulfillment of the
requirements for the degree of
Erasmus Mundus Master Course in Sustainable Transportation and Electrical Power Systems

Abstract

In this thesis the modelling and simulation of a multifunctional PV electrochemical storage system is performed. Due to presence of two DC power sources, this system belongs to the grid tied hybrid energy storage system (HESS) category. In this work, all the component-level controlling schemes are implemented in order to equip HESS with the functionalities which enables the system to achieve the following objectives:

- Extracting the maximum available photovoltaic (PV) energy
- Controlling the battery energy storage system (BESS) charge-discharge operation
- Controlling the grid tied inverter power flow
- Controlling the grid power injection-absorption (GPIA)
- Providing grid frequency-voltage regulation (GFVR) services

These objectives are achieved by implementing the necessary controllers and algorithms in Matlab/Simulink environment such as, PV maximum power point tracking (MPPT), BESS charge-discharge management (CDM), BESS charge-discharge controller (CDC), DC link voltage controller (DCVC), inverter current control (ICC) and combined GPIA and GFVR controller. Moreover, the HESS component models are presented in detail. Furthermore, the model performance is validated by laboratory verification.

Thesis Supervisor: Pablo García Fernández
Title: Associate Professor at University of Oviedo

Thesis Supervisor: Johann Mayr
Title: Junior Research Engineer at Austrian Institute of Technology (AIT)

Acknowledgments

This master thesis had been fulfilled under the agreement made between the Erasmus Mundus STEPS program and the Austrian Institute of Technology GmbH.

The author of this thesis would like to offer special thanks to the STEPS coordinating committee for all the scientific and motivational support given prior to and during the thesis time-frame. Specifically, I am grateful to Prof. Pablo García Fernández who approved the thesis proposal and guided me as the academic supervisor.

I would also like to especially thank my supervisor at AIT, Johann Mayr, for his advices, comments, and the huge time and effort he spent on helping me to carry out this thesis.

Moreover, I would like to express my appreciation for the AIT Energy Department research team with special thanks to Johannes Kathan who helped me feel as a team member while working on the LEAFS project and Christian Messner who provided technical guidance through the laboratory test sessions.

Contents

List of Figures

List of Tables

List of Abbreviations

AIT	Austrian Institute of Technology
BBBC	Bidirectional Buck-Boost Converter
BESS	Battery Energy Storage System
BRCG	Battery Reference Current Generator
CDC	Charge-Discharge Controller
CDM	Charge-Discharge Management
DCC	DC Link Charger
DCPR	DC Power Regulation
DCVC	DC Link Voltage Controller
DUT	Device Under Test
GPIA	Grid Power Injection-Absorption
GFVR	Grid Frequency-Voltage Regulation
GPMU	Grid Power Management Unit
HESS	Hybrid Energy Storage System
HVDC	High Voltage Direct Current
IC	Incremental Conductance
ICC	Inverter Current Controller
LV	Low Voltage
MP	Measurement Point
MPP	Maximum Power Point
MPPT	Maximum Power Point Tracking
NPC	Neutral Point Clamped
PCC	Point of Common Coupling
PFC	Power Flow Control
PLL	Phase Locked Loop
P&O	Perturb and Observe
PV	Photovoltaic
PVGU	PV Generation Unit
SCADA	Supervisory Control And Data Acquisition
SCO	Self Consumption Optimization
SoC	State of Charge
STC	Standard Test Condition

Chapter 1

Introduction

In this thesis the modelling and simulation of a multifunctional PV electrochemical storage system is performed. Due to the presence of two DC power sources (i.e. PV and BESS), this system belongs to the grid tied hybrid energy storage system (HESS) category. For household applications HESS must be equipped with functionalities which enable the system to provide necessary services to the HESS owner and the LV grid network. The required functionalities for the household HESS are the followings:

- Extracting the maximum available photovoltaic (PV) energy
- Controlling the battery energy storage system (BESS) charge-discharge operation
- Providing suitable household load profile tracking
- Controlling the grid tied inverter power flow
- Controlling the grid power injection-absorption (GPIA)
- Providing grid frequency-voltage regulation (GFVR)

The objectives are achieved by implementing the following controlling scheme and algorithms in Matlab/Simulink environment:

- PV maximum power point tracking (MPPT)
- BESS charge-discharge management (CDM)
- BESS charge-discharge controller (CDC)
- DC link voltage controller (DCVC)
- Inverter current control (ICC)
- Combined GPIA and GFVR controller

All the implemented features and model components results in a full simulation of HESS behaviour which can be also also validated with the lab testing data.

1.1 Contribution to the LEAFS Project

This master thesis is fulfilled as a part of one of the ongoing AIT research projects which is called Integration of Loads and Electric storage systems into Advanced Flexibility Schemes for LV networks (LEAFS). In this project the effect of the large-scale utilization of household HESS and central storage systems on LV grid is evaluated. And the flexibility scheme is integrated to the LV grid operation by actively controlling the household HESS and facilitating dynamic communication between the virtual power plant operator and distributed HESS and a centralized storage systems.

The result of this thesis will be used in future developments as the core model for simulations prior to lab testing. Furthermore, since the household HESS model is modularized and designed in the per-unit system, this model can be up-scaled to simulate the functional behaviour of central storage systems.

Chapter 2

Hybrid Energy Storage System Description

In this chapter the HESS topology is introduced. Moreover due to presence of two DC power sources (PV and battery energy storage) there is a variety of possible coupling methods. In this chapter only two possibility are discussed. Furthermore, a brief review over the measurement reference frame based on the power flow through the system.

2.1 HESS Coupling

2.1.1 DC Coupling

The HESS topology chosen for this thesis is illustrated in Fig. 2-1. This topology is categorized as a general DC coupled system. with this configuration the PV and BESS are linked together via a DC capacitor and tied to the grid through an inverter stage. In this case, the grid tied inverter must be capable of managing overall PV and BESS power. Moreover, there is just a single power path from DC to AC side. One of the advantages of this coupling is the fact that there is a power path available from PV to BESS on the DC side, which makes the system suitable for storing the excess PV power must be stored in BESS. In this case the power does not pass through the AC side eliminating the inverter related losses.

As depicted in Fig. 2-1, The DC coupled HESS topology adopted in this thesis includes the following components:

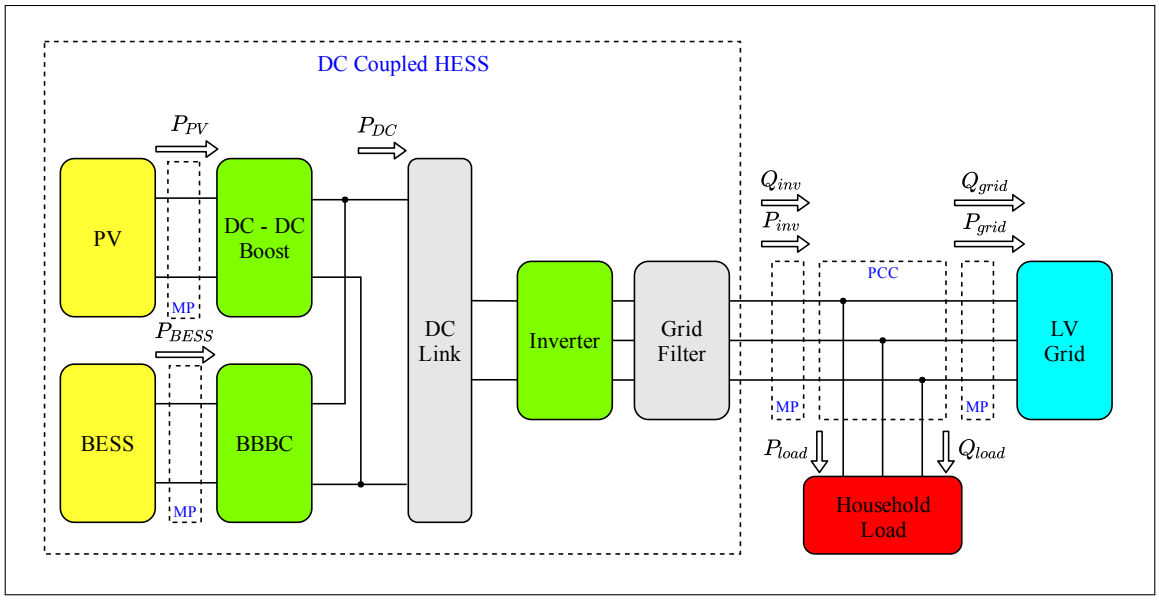

Figure 2-1: Schematic of DC coupled HESS tied to the LV grid.

- PV
- BESS
- DC - DC boost
- Bidirectional buck-boost converter (BBBC)
- DC link
- Inverter
- Grid filter
- Household load
- LV grid

The corresponding model for each component is discussed in chapter 3. Additionally, system functionalities and control design are presented in chapters 4 and 5.

2.1.2 AC Coupling

HESS can be also coupled at the AC side. An example of this coupling method is shown in Fig. 2-2. In this topology there is an individual inverter for PV and BESS, which allows two separate DC to AC power paths. This is beneficial in the sense of redundancy, however employing two inverters may not be the most cost efficient solution. This topology is suitable for the applications where the BESS direct charge-discharge from the grid is desired.

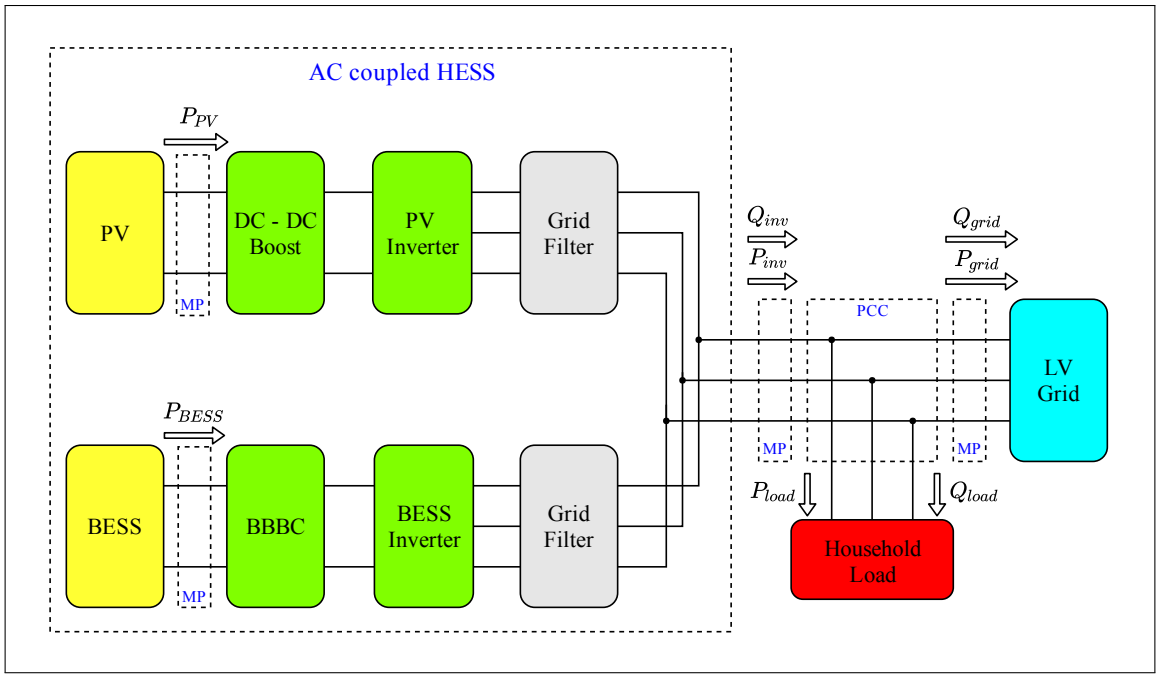

Figure 2-2: Schematic of AC coupled HESS tied to the LV grid..

2.2 Reference Frame and Measurement Points

The reference frame for DC coupled HESS is defined based on the power flow arrows shown in Fig. 2-1. Power and current flows in the direction of the arrow are assigned positive. As it is shown in the figure, there are four measurement points for the HESS. Measuring power at the both sides of PCC leads to obtaining an indirect measurement of household load consumption.

Chapter 3

HESS Components Model

3.1 DC Side components

In this section the modelling methods for HESS DC side components (including PV, BESS, PV DC -DC boost, BBBC and DC link) are presented.

3.1.1 PV Generation

A PV module consists of a number of individual PV cells connected in series and in parallel. Similarly, modules can be connected to form a PV string. Within a string modules can also be connected in series and in parallel. The series connection increases the voltage and the parallel connection increases the current. Usually, modules are connected mostly in series to achieve higher voltage levels and therefore decrease the current, which leads to lower losses on the line connection. The power processing device (converter) must be able to handle the voltage and current levels of the strings. Therefore the string voltage V_{string} is equal to the number of serial modules in string N_{sm} times the module voltage V_{mod}. And the overall string output current I_{string} can be evaluated by a single module current I_{mod} multiplied by the number of parallel connections N_{pm}. Similarly, the module voltage and current can be identified in terms of a single PV cell voltage V_{cell}, cell current I_{cell}, number of serial cells in a module N_{sc} and number of parallel cells in a module N_{pc}.

As a result, the string voltage and current can be described in terms of cell current and voltage:

$$V_{string} = N_{sm}.V_{mod} = N_{sm}.(N_{sc}.V_{cell}) \tag{3.1}$$

$$I_{string} = N_{pm}.I_{mod} = N_{pm}.(N_{pc}.I_{cell}) \tag{3.2}$$

In a same way, multiple strings can be connected in series and in parallel to form a PV

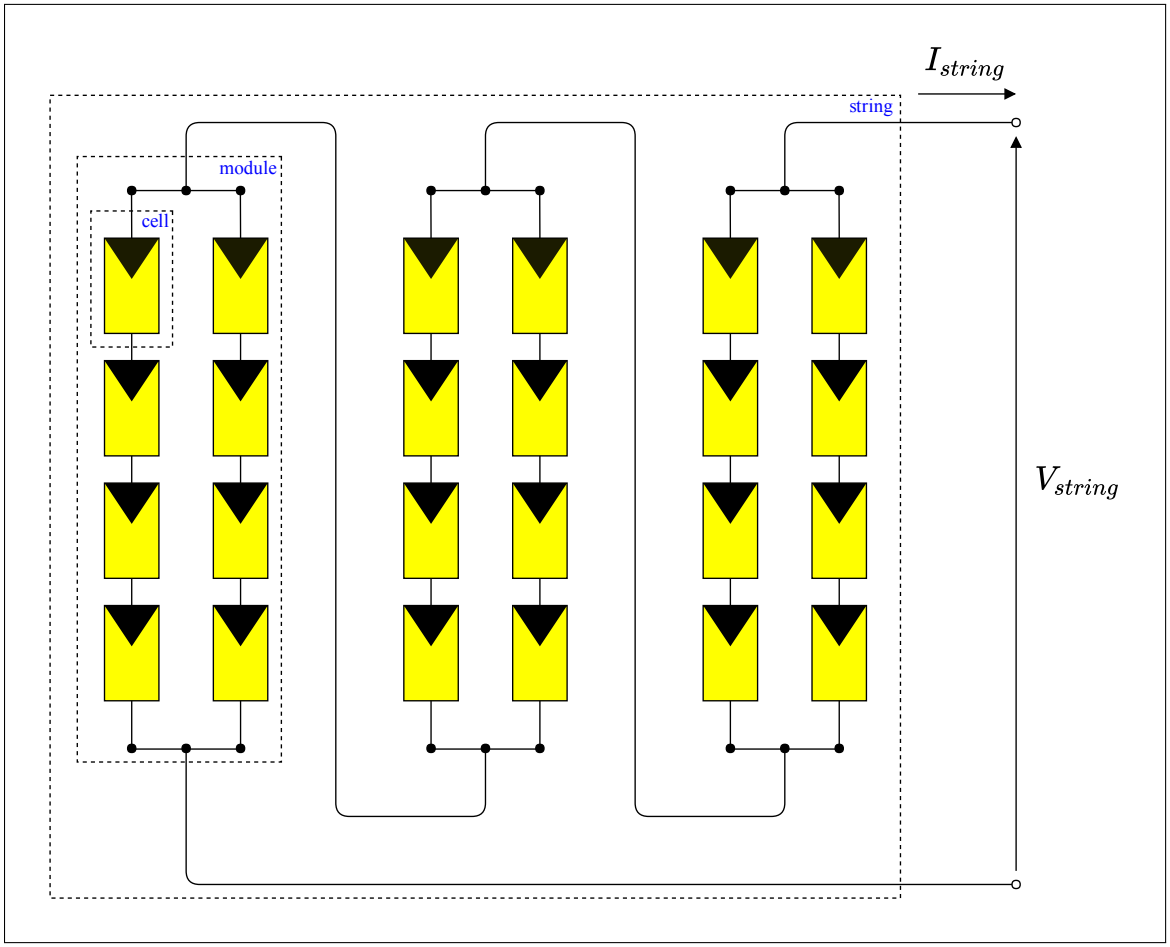

Figure 3-1: PV string consist of serial module connections.

generation unit. In this thesis the partial shading and non-uniform environmental conditions are neglected. Thus, the up-scaling from cell to the string based on (3.1 and 3.2) are valid, under the hypotheses that the cells are identical and they operate with the same temperature and irradiance. Hereafter, the term PV stands for PV generation unit.

PV Characteristics Curves

The characteristic curves of PV include $I-V$ and $P-V$ as shown in Fig. 3-2. These curves are normalized with respect to the standard test conditions (STC) values for temperature (T) and irradiance (G). The Fig. 3-2 shows that the maximum power point (MPP) is strongly dependent on irradiance and temperature.

Ideal and Single Diode Model

In order to formulate a circuit model for the PV we may derive the model governing equations for a single cell and then rescale the model based on the discussion in Section 3.1.1. By considering the $I-V$ characteristic, intuitively we can observe that the behaviour can be explained by a constant current and a decaying factor (Fig. 3-3). This behaviour can be modelled with a constant current source in parallel with a diode. It should be taken into account that this ideal model is only valid under no-loss condition. In this model, the parallel diode current I_d reflects the physical behaviour of the cell $p-n$ junction and the current source models the photocell current I_{ph}, which is dependent on the temperature and irradiance changes, this is shown by:

$$I_{ph} = I_{ph,STC}.\frac{G}{G_{STC}}.[1+\alpha.(T-T_{STC})] \tag{3.3}$$

Where the subscript STC identifies the values in standard test condition and α is the temperature coefficient:

$$\alpha = \left.\frac{dI}{dT}\right|_{STC} \tag{3.4}$$

Therefore the $I-V$ shown in Fig. 3-2 can be expressed by:

$$I = I_{ph} - I_{sat}.(e^{\frac{V}{\eta.V_t}} - 1) \tag{3.5}$$

Where η is the ideality factor. Furthermore, V_t and I_{sat} are respectively the thermal voltage and diode saturation current expressed by:

$$V_t = \frac{k.T}{q} \tag{3.6}$$

$$I_{sat} = C.T^3.e^{-\frac{Egap}{K.T}} \tag{3.7}$$

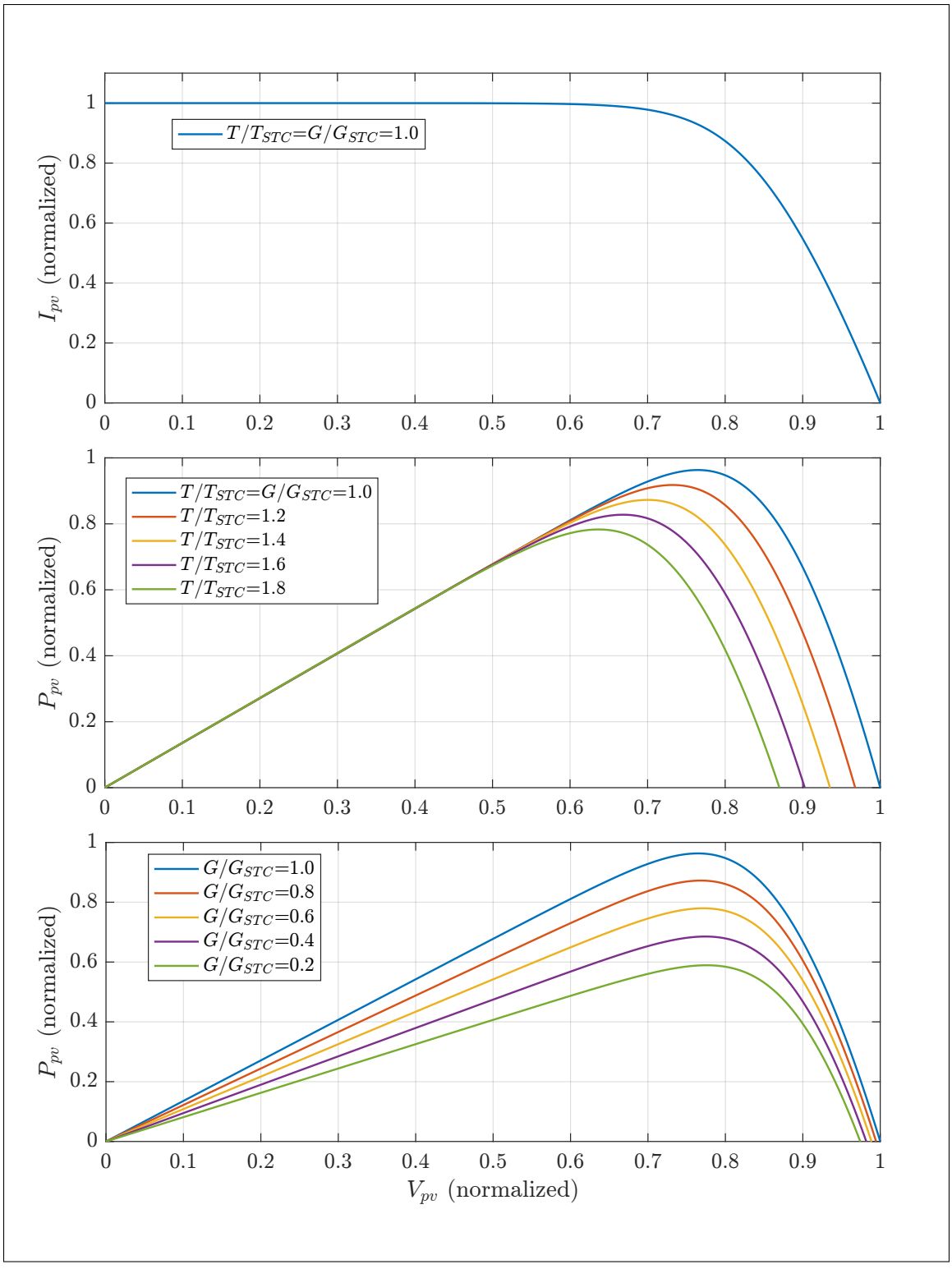

Figure 3-2: PV current vs. voltage under STC (top), PV power vs. voltage under temperature increment (middle) and irradiance decrement (bottom).

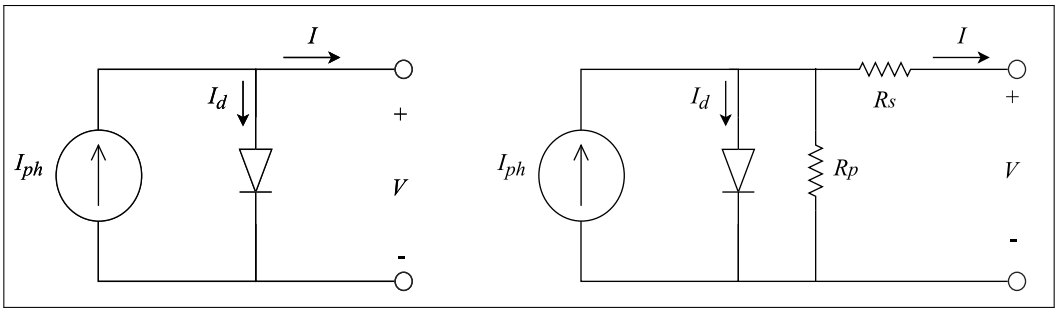

Figure 3-3: PV ideal model (left) and single diode model (right).

Where q is the electron charge and k is the Boltzmann constant.

In order to make the model more realistic the losses can be considered by a series R_s and parallel Rp resistances (Fig. 3-3). R_s represents the semiconductor losses corresponding to the $p-n$ junction and R_p the internal cell resistance. By introduction of R_s and R_p the modified version of (3.5) is obtained:

$$I = I_{ph} - I_{sat}.(e^{\frac{V+I.R_s}{\eta.V_t}} - 1) - \frac{V + I.R_s}{R_p} \tag{3.8}$$

The main effects of these losses can be seen as the $I-V$ curve slope variation close to V_{oc} (corresponding to R_s) and close to I_{sc} (corresponding to R_p). Hence they are approximated by:

$$R_s = -\left.\frac{dV}{dI}\right|_{V=V_{oc}} \qquad \text{and} \qquad R_p = -\left.\frac{dV}{dI}\right|_{I=I_{sc}} \tag{3.9}$$

This model can be served as the base idea to develop the double diode model which integrates better loss consideration in the circuit. This model alongside the parameters identification are intensively discussed in [1].

PV Linearized Model

PV current-voltage relation expressed by (3.5) is clearly a non-linear equation. In this subsection the linearized PV model is described. It is desired to keep PV working close to MPP. As it is suggested in [2] a linear approximation of $I-V$ curve around MPP can linearize the model. Therefore (3.5) is approximated by its tangent line at V_{MPP} (Fig. 3-4) and the derivative of (3.5) is evaluated at MPP:

$$m = \left.\frac{dI}{dV}\right|_{MPP} = -\frac{I_{sat}}{\eta.V_t}.(e^{\frac{V_{MPP}+I_{MPP}.R_s}{\eta.V_t}}) - \frac{1}{R_p} \tag{3.10}$$

Consequently, the linear $I-V$ behaviour around MPP is expressed by:

$$I = m.V + (-m.V_{MPP} + I_{MPP}) \tag{3.11}$$

and the equivalent circuit model of (3.11) is a DC voltage source connected in series with a

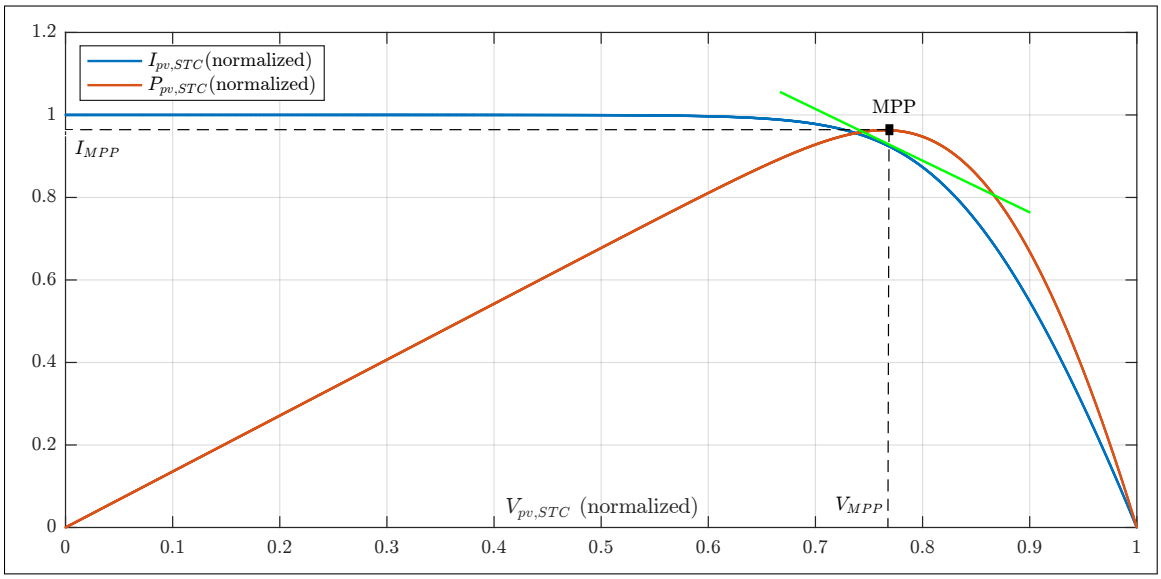

Figure 3-4: PV $I-V$ curve linearization.

negative resistance (dynamic resistance):

$$V_m = V_{MPP} - \frac{I_{MPP}}{m} \tag{3.12}$$

$$R_m = -\frac{1}{m} \tag{3.13}$$

3.1.2 Battery Energy Storage System

In this section a generic model of a BESS is introduced which is based on the modelling method presented in [3] and [4]. The simplest way to model a battery is by using a controlled voltage source E_{bat} connected in series with resistance R_{bat}. This simple model is valid under the assumption that the charge and discharge characteristics are identical. This BESS model can be expressed by the following equations:

$$V_{bat} = E_{bat} - R_{bat}.I_{bat} \quad , \quad SoC = G(I_{bat}) = 100.\left(1 - \frac{\int I_{bat}.dt}{Q}\right) \tag{3.14}$$

In which E_{bat} is a non-linear function of state of charge (SoC):

$$E_{bat} = F(SoC) = E_0 - K.\left(\frac{1 - SoC}{SoC}\right).Q + V_{exp}.e^{-C_{exp}.(1-SoC).Q} \tag{3.15}$$

Where E_0 is the battery constant voltage, K is the polarization voltage, V_{exp} is the exponential zone voltage, C_{exp} is the exponential capacity and Q is the battery capacity. Equations (3.14) and (3.15) are the basis of the battery circuit model shown in Fig. 3-5. Moreover, a generic BESS discharge curve (1.3 Votls and 6.5 Ah with 1 Amp discharge current) is plotted. The BESS parameters identification method is discussed in [4].

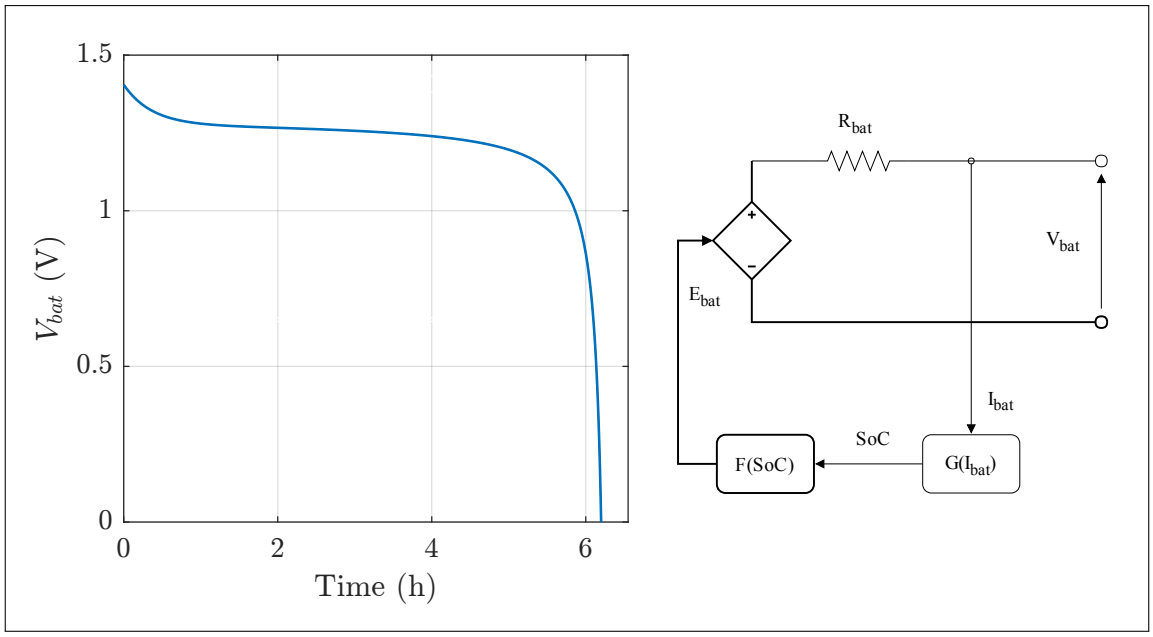

Figure 3-5: Generic BESS discharge curve (left), BESS circuit model (right).

3.1.3 PV DC - DC Boost

In many PV applications for HESS, the DC link nominal voltage is higher than PV open circuit voltage. Therefore, a step-up DC-DC converter is connected in series with the PV string (Fig. 3-6). Moreover, as it is discussed in the Chapter 4, this intermediate stage helps to extract the maximum available energy from the PV. State space averaging method is adopted to model the PV DC - DC boost converter. For this purpose, a linearized PV model introduced in Section 3.1.1 is used. The converter output stage for the HESS is DC link capacitor. Due to the presence of the DC link voltage controller (DCVC), the DC link

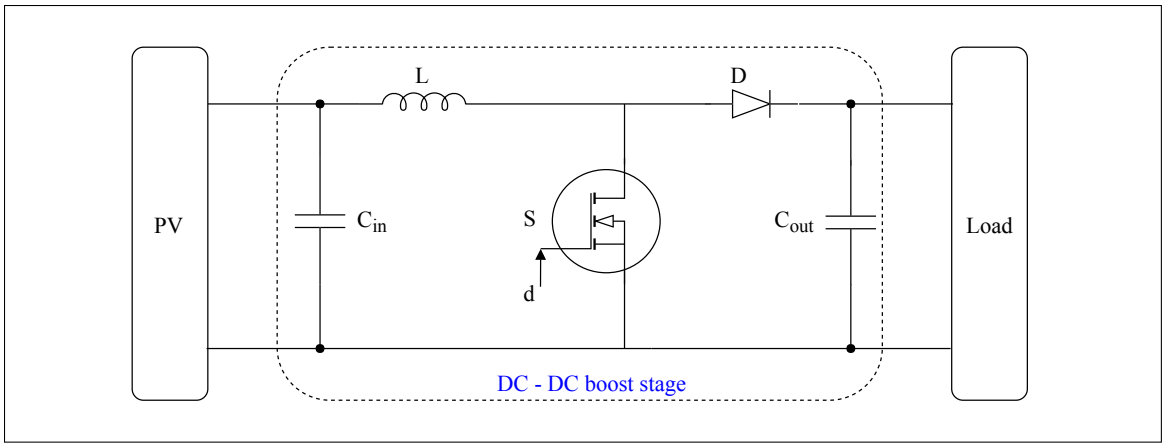

Figure 3-6: PV DC - DC boost converter.

imposes a constant voltage V_{DC} at the boost output stage. Therefore, the dynamics of output capacitor C_{out} can be neglected. Also in this analysis the parasitic components of boost capacitors are ignored and the switching devices (diode D and switch S) are considered to be ideal. Fig. 3-7 shows the circuit topology when the switch is on and off. By considering

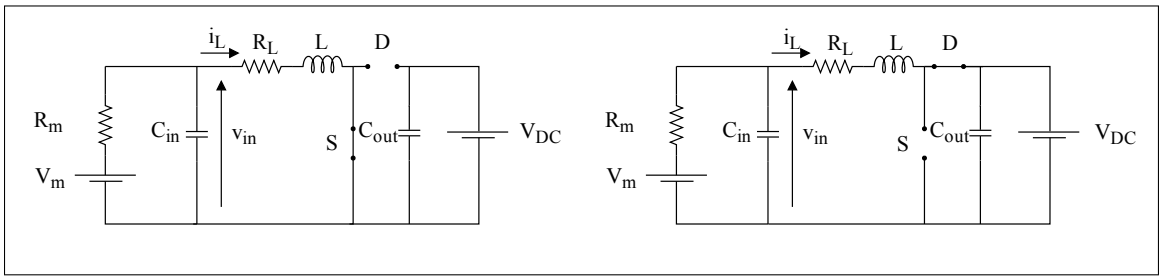

Figure 3-7: PV DC - DC boost converter circuit, S: on (left), S: off (right).

the i_L and v_{in} as state variables and V_m and V_{DC} as inputs:

$$x = \begin{bmatrix} i_L \\ v_{in} \end{bmatrix} \quad \text{and} \quad u = \begin{bmatrix} V_m \\ V_{DC} \end{bmatrix} \tag{3.16}$$

For the switch-on period, the states equation is written as:

$$\frac{dx}{dt} = A_1 x + B_1 u \tag{3.17}$$

Where:

$$A_1 = \begin{bmatrix} \frac{-R_L}{L} & \frac{1}{R_L} \\ \frac{-1}{C_{in}} & \frac{-1}{C_{in}.R_m} \end{bmatrix} \quad \text{and} \quad B_1 = \begin{bmatrix} 0 & 0 \\ \frac{1}{C_{in}.R_m} & 0 \end{bmatrix} \tag{3.18}$$

And for the switch-off period, state equation is:

$$\frac{dx}{dt} = A_2 x + B_2 u \tag{3.19}$$

where:

$$A_2 = \begin{bmatrix} \frac{-R_L}{L} & \frac{1}{R_L} \\ \frac{-1}{C_{in}} & \frac{-1}{C_{in}.R_m} \end{bmatrix} \quad \text{and} \quad B_2 = \begin{bmatrix} 0 & \frac{-1}{R_L} \\ \frac{1}{C_{in}.R_m} & 0 \end{bmatrix} \tag{3.20}$$

Consequently, the state space averaged equation can be written as:

$$\frac{\Delta x}{T} = \frac{d\bar{x}}{dt} = (A_1 d + A_2(1-d))\bar{x} + (B_1 d + B_2(1-d))\bar{u} \tag{3.21}$$

Where d and T are the boost duty and switching period. Clearly, due to time varying nature of d, x and u the system of equations (3.21) is non-linear. Thus, to linearize the system these variables are substituted by their perturbed steady state values:

$$x = X + x_p \quad , \quad u = U + u_p \quad , \quad d = D + d_p \tag{3.22}$$

Where d_p , x_p and u_p are small perturbation from the steady state values. Now, by replacing the $\bar{d}$, $\bar{x}$ and $\bar{u}$ with (3.22) in (3.21) and eliminating the second order terms, the linearized time invariant version of (3.21) is resulted:

$$\frac{dx_p}{dt} = ((A_1 - A_2)X + (B_1 - B_2)U)d_p \tag{3.23}$$

By applying the Laplace transform, the following transfer functions can be obtained:

$$G_{i_L d} = \left.\frac{i_{Lp}(s)}{d_p(s)}\right|_{u_p=0} \quad , \quad G_{v_{in} d} = \left.\frac{v_{inp}(s)}{d_p(s)}\right|_{u_p=0} \quad , \quad G_{v_{in} i_L} = \frac{\left.\frac{v_{inp}(s)}{d_p(s)}\right|_{u_p=0}}{\left.\frac{i_{Lp}(s)}{d_p(s)}\right|_{u_p=0}}. \tag{3.24}$$

$G_{i_L d}$ can be used for the inner control loop to regulate the inductor current. And $G_{v_{in} i_L}$ can be used in the outer control loop to regulate the input voltage. Although it is discussed in Section 5.1.1, in this thesis it is desired to directly control the input voltage via the duty cycle of the converter, therefore $G_{v_{in} d}$ is of interest here. This transfer function can be evaluated as:

$$G_{v_{in} d} = \frac{k}{s^2 + 2\zeta.\omega_n.s + \omega_n^2} \tag{3.25}$$

Where:

$$k = \frac{V_{DC}}{L.C_{in}} \quad , \quad \omega_n = \sqrt{\frac{R_m - R_L}{R_m.L.C_{in}}} \quad , \quad \zeta = \frac{R_m.L.C_{in} - L}{2R_m.L.C_{in}\omega_n} \tag{3.26}$$

As discussed in previous section, usually the PV model linearization point is close to MPP (see Fig. 3-4, where $V_{MPP} = 0.78 V_{pv,oc}$). But it should be taken into account that changing the linearization point of the PV model (resulting in different R_m values), can slightly affect the dynamics of the input voltage defined by (3.25). The influence of linearization point variation is shown in Fig. 3-8. This issue is comprehensively discussed in [5]. Furthermore, the analysis of (3.26) for a PV battery charger system is presented in Section 5.1.1.

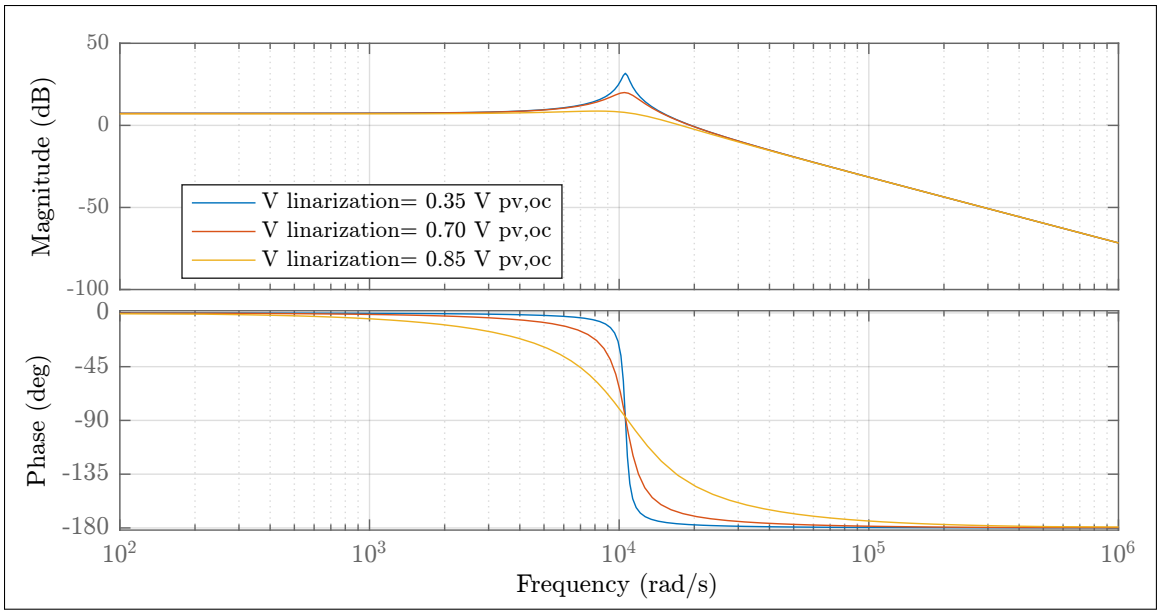

Figure 3-8: Linearization point deviation effect on $G_{v_{in} d}$.

3.1.4 Bidirectional Buck-Boost Converter

Adopting BBBC topology as an intermediate stage to interface battery with the rest of HESS system, allows a controlled bidirectional power flow between battery and DC link capacitor. This stage is the necessary component to implement CDC which regulates battery current. The adopted BBBC topology in this thesis is illustrated in Fig. 3-9. considering different

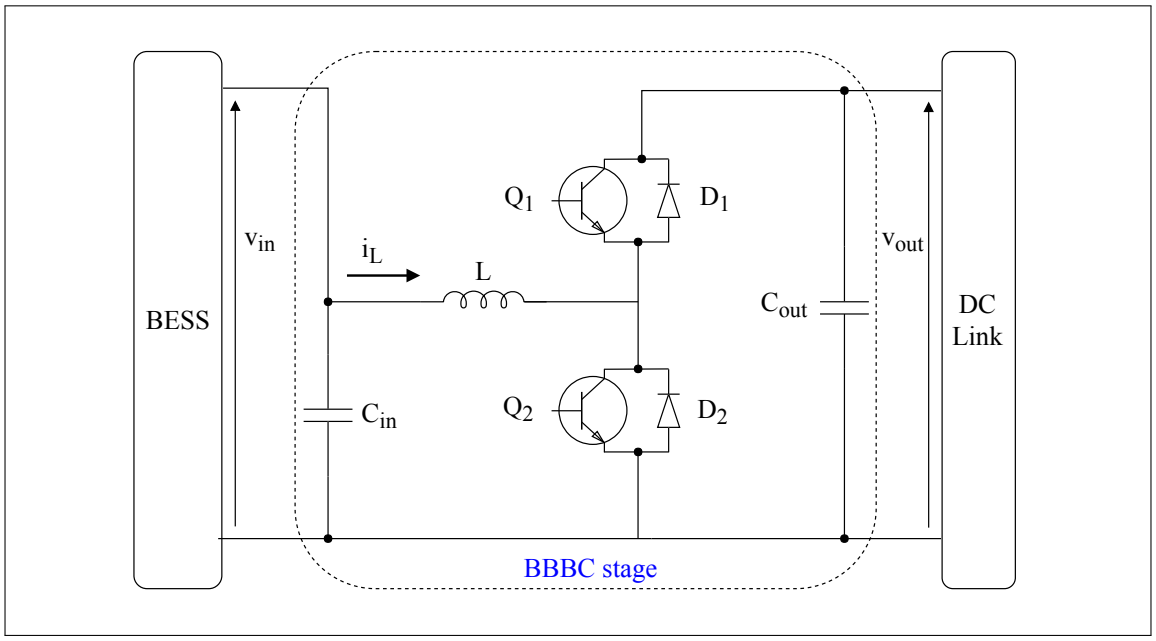

Figure 3-9: Bidirectional buck-boost converter.

voltage levels for BESS and load (in the case of HESS, load is DC link capacitor) four modes of operation Fig. 3-10 can be identified for the system shown in Fig. 3-9. It must be kept in mind that Q_1 and Q_2 are switched via complementary switching functions. Let the DC link reference voltage regulated by DCVC be higher than BESS nominal voltage, thus the BBBC operational modes are:

- mode 1: system operates as boost converter and BESS charges the inductor.
  (Q_1: off , Q_2: on, D_1 and D_2: reverse biased)
- mode 2: BESS delivers power to DC link capacitor.
  (Q_1: off, Q_2: off, D_1: conducting, D_2: reverse biased)
- mode 3: system operates in buck mood. DC link capacitor delivers power to BESS.
  (Q_1: on, Q_2: off, D_1: and D_2: reverse biased)
- mode 4: inductor discharge the stored energy in BESS.
  (Q_1: off, Q_2: off, D_1: reverse biased and D_2: conducting)

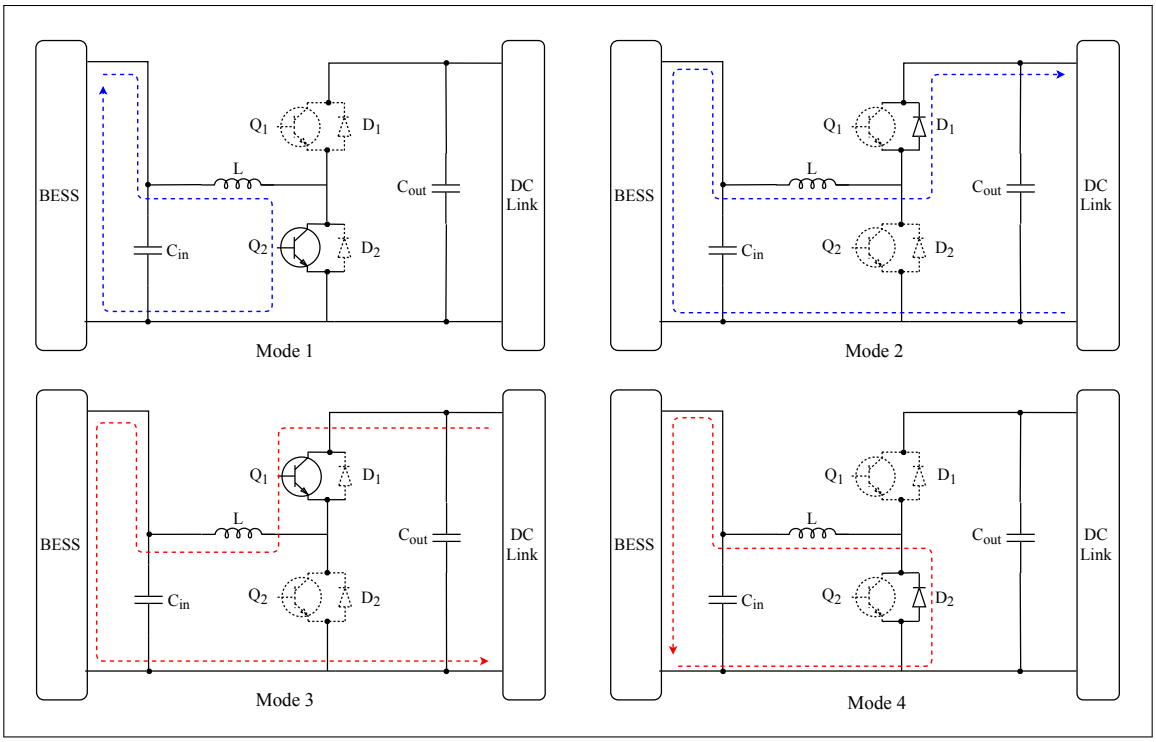

Figure 3-10: BBBC switching modes.

In order to formulate the BBBC model, the same methodology as PV boost converter is taken. For this purpose, v_{in} , v_{out} and i_L can be considered as state variables, and with the same previously mentioned steps $G_{v_{in}d}$, $G_{v_{out}d}$ and G_{i_Ld} can be derived [6]. As it is depicted in Fig. 3-9 BBBC input and output stages are connected with BESS and DC link. Thus, these stages impose roughly constant voltages (V_{bat} and V_{DC}) over C_{in} and C_{out}. Hence, the dynamics of these capacitors can be neglected. This in turn results in a first order transfer function G_{i_Ld} and inductor steady state current expression, represented by:

$$G_{i_Ld} = \frac{i_L(s)}{d(s)} = \frac{V_{DC}}{L.s + R_L} \quad , \quad I_L = \frac{D.V_{DC} - V_{bat}}{R_L} \tag{3.27}$$

Where R_L is the inductor series resistance and D is steady state duty cycle. This transfer function will be used in Chapter 5 to design CDC which regulates battery current.

3.1.5 DC Link

In this thesis the DC Link is modelled with a capacitive voltage divider which is shown in Fig. 3-11. In which the capacitive voltage divider mid-point is connected to the inverter neutral point. Ideally, this topology divides DC link reference voltage into half. This is

valid if the inverter AC side currents are balanced and the three-phase modulating signals are perfectly symmetric. Moreover, it is assumed that the divider capacitors are perfectly identical in terms of their manufacturing tolerance and parasitic components. If these assumption are violated, then the capacitors voltages experience a drift from their ideal values $\frac{V_{DC}}{2}$. Which in turn affects the inverter output voltage levels. To address this issue, a voltage equalizing scheme must be adopted. This can be done with employing an auxiliary circuit which balances the stored charges in two capacitors [7]. Alternatively, it can be also done by manipulating the modulating signals in order to inject a DC current component into the inverter midpoint which balances the capacitive voltages [8].

3.2 Inverter

Grid tied inverters might be considered as the most crucial components in the sense of power flow control in HESS applications. The inverter stage facilitates the bidirectional power flow between DC and AC side. Moreover, the inverter control is in charge of synchronizing its output voltage to the grid voltage, to avoid faulty conditions. In the following, the switching model for HESS inverter is presented.

3.2.1 NPC Topology

The main problem regarding the two-level full-bridge inverter would be the high voltage which the switches must withstand during the off state. Especially, by the development of high voltage direct current (HVDC) technologies, the DC voltage limit can be considerably high, and usually the state of art switches which are suitable for HVDC application are expensive. One way to address this issue is to connect multiple switches in series to lower the required rating for each switch. Although this seems to be feasible solution, this design requires completely identical gating signals for the series switches, which in fact is hard to achieve because of the gating circuits manufacturing tolerances. To counteract this the nuetral point clamped (NPC) topology is introduced, in which the off-voltage over each switch is a fraction (depending on the multi-level structure) of the DC link voltage. In this thesis the three-level NPC topology is adopted and its model is briefly discussed in the following. A half-bridge schematic diagram of the three-level NPC inverter is shown in Fig. 3-12. In NPC topology each leg includes a couple of embedded two-level half-bridges

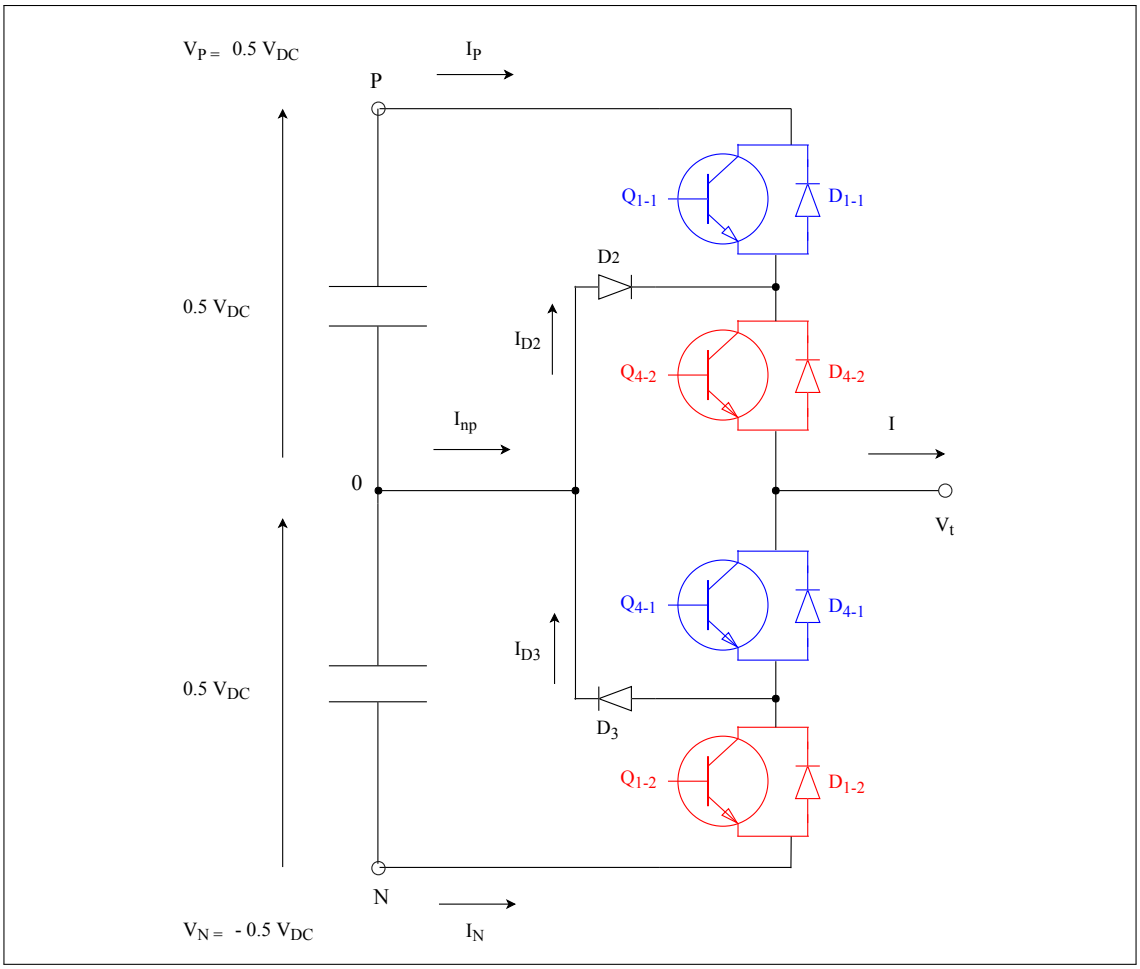

Figure 3-11: Half-bridge three-level NPC inverter schematic diagram.

(identified by switch pairs (1-1,4-1) and (1-2,4-2). It should be considered that the overall DC link voltage is divided in half by a serial connection of two identical capacitors. The mid-point of the DC side (neutral point) which is connected to the clamping diodes is considered as measurement reference. To analyze the operation of the NPC inverter let us define the generic switching function as:

$$s(t) = \begin{cases} 1 & \text{if switch is on} \\ 0 & \text{if switch is off} \end{cases} \tag{3.28}$$

To avoid short circuit occurrence the switch pairs must operate in complementary mode i.e. when switch 1-1 is on then 4-1 must be off. This behaviour can be described by the

corresponding switching functions:

$$s_{1-1} + s_{4-1} = 1 \qquad \text{and} \qquad s_{1-2} + s_{4-2} = 1 \tag{3.29}$$

Three-level Terminal Voltage Generation

In this part, firstly the positive terminal voltage generation is explained. For this case the following switching state for pair (1-2,4-2) is assumed:

$$\bar{s}_{1-2,4-2} = \begin{cases} s_{1-2} = 0 \\ s_{4-2} = 1 \end{cases} \tag{3.30}$$

and for the other switch pair (1-1,4-1):

$$s_{1-1,4-1} = \begin{cases} s_{1-1} = 1 \\ s_{4-1} = 0 \end{cases} \tag{3.31}$$

Then by regarding the direction of terminal current i, two possible scenarios exist: if $i_p > 0$ then Q_{1-1} conducts and if $i_p < 0$ then D_{1-1} conducts. So regardless of direction of the terminal current for the switching state defined by (3.31) the terminal voltage is $V_t = V_P = \frac{V_{DC}}{2}$. And for the complementing switching state of (3.31):

$$\bar{s}_{1-1,4-1} = \begin{cases} s_{1-1} = 0 \\ s_{4-1} = 1 \end{cases} \tag{3.32}$$

If $i_p > 0$ then D_2 conducts and if $i_p < 0$ then Q_{4-1} and D_3, so regardless of the terminal current sign $V_t = 0$.

The analysis for negative terminal voltage generation follows the same steps. For this case, firstly the switching state (3.32) is assumed for the pair (1-1,4-1). Consequently the analysis is done for states (3.30) and its complement, which is:

$$s_{1-2,4-2} = \begin{cases} s_{1-2} = 1 \\ s_{4-2} = 0 \end{cases} \tag{3.33}$$

Under the condition (3.32) by checking both output current directions, it is possible to conclude that when (3.33) is valid then $V_t = V_N = \frac{-V_{DC}}{2}$. And when (3.30) is valid then $V_t = 0$. The NPC circuit diagram corresponding to these operational modes is shown in Fig. 3-12. Thus the output voltage can achieve three voltage levels $(\frac{V_{DC}}{2}, 0, \frac{-V_{DC}}{2})$. In the

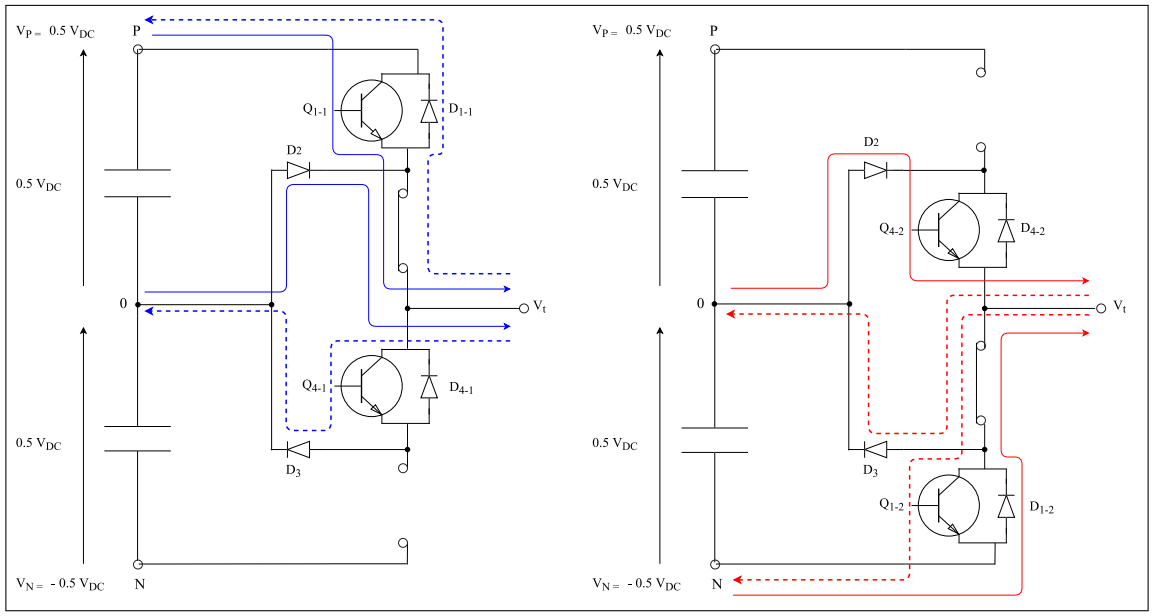

Figure 3-12: Three-level voltage generation, positive voltage (left), negative voltage(right), positive and negative output current shown with solid and dashed line.

next section the modulation scheme is briefly reviewed.

Pulse Width Modulation Scheme

The pulse width modulation (PWM) scheme for a three-level half-bridge NPC must guarantee the gating signal coordination between the embedded two-level half-bridges (Fig. 3-12). Moreover, it must be capable of controlling the positive and negative average AC side terminal voltage V_t. The PWM scheme shown in Fig. 3-13 is capable of fulfilling these requirements. In this scheme a unipolar carrier signal is adopted due to the fact that the switch pairs (1-1,4-1) and (1-2,4-2) must generate either a positive or negative terminal voltage. In order to generate switching functions, the modulating signal m and $-m$ are compared with the unipolar carrier. In this case if m is greater than the carrier turn-on command is assigned to switch 1-1 and 4-1 is turned off. It is clear that in this case $-m$ is lower than the carrier, hence switch 1-2 is off and switch 4-2 is on. This is equivalent to the circuit diagram shown in Fig. 3-12 for positive voltage generation. If $-m$ is greater than

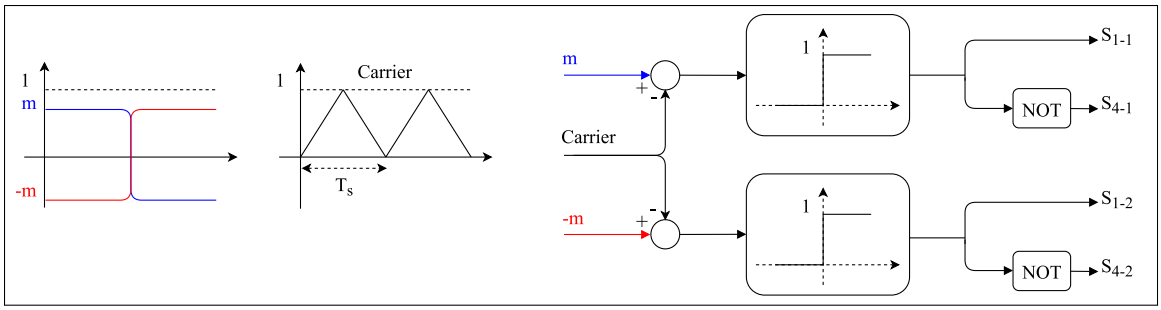

Figure 3-13: NPC PWM scheme.

carrier switch 1-2 is on and 4-2 is off, while 1-1 is off and 1-4 is on. This case is equivalent to negative voltage generation circuit diagram in Fig. 3-12. Switching function generation for positive and negative m is shown in 3-14.

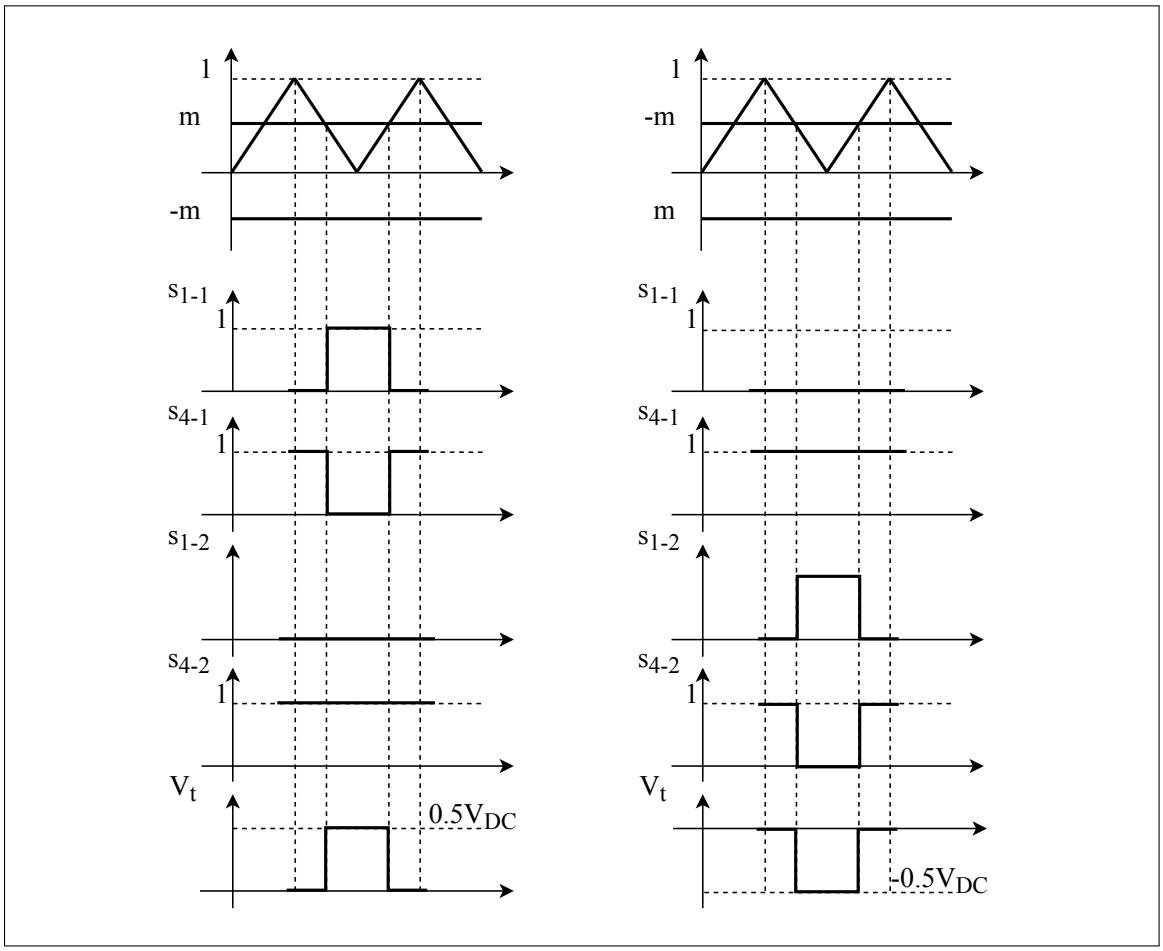

Figure 3-14: NPC switching functions generation. Positive modulating signal(left), negative modulating signal(right).

As shown in Fig. 3-14 the length of time period in which switch 1-1 is on, is proportional to the magnitude of m. A higher m keeps the switch 1-1 to stay on and switch 4-1 to stay off for a longer time. Thus it increases the time interval in which $V_t = \frac{V_{DC}}{2}$. This means that the average terminal voltage is proportional to m. And since the rate of variation for m is much smaller than carrier frequency, the average terminal voltage can be approximated by:

$$\bar{V_t} = m(t).\frac{V_{DC}}{2} \tag{3.34}$$

This argument is valid also when m is negative. In the next section the three-phase three-level NPC topology is introduced.

Three-Phase Three-Level NPC Inverter

Three-phase three-level NPC includes three identical NPC half-bridges shown in Fig. 3-11. In this topology each half-bridge corresponds to one of the AC side phases, and it allows a bidirectional power flow between DC and AC sides. The governing equation for this

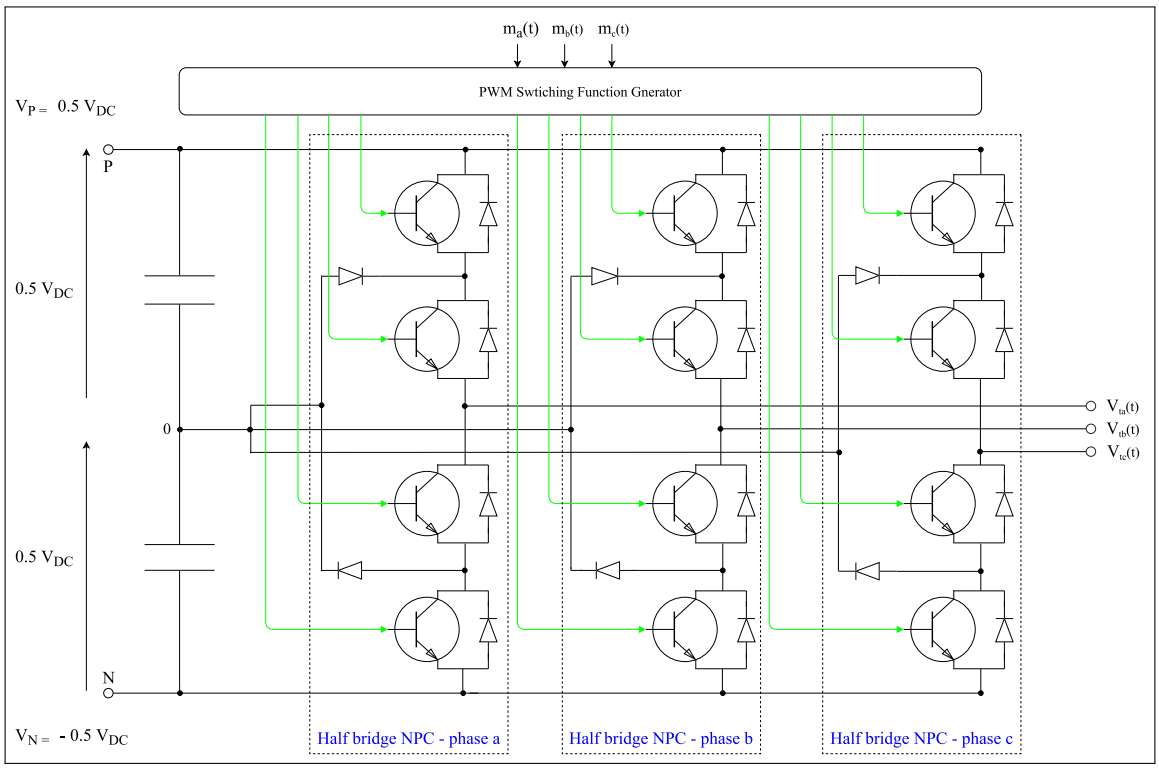

Figure 3-15: Three-phase three-level NPC topology.

topology is based on (3.34) but extended to three-phase system:

$$\begin{aligned} V_{t,a}(t) &= m_a(t).\frac{V_{DC}}{2} \\ V_{t,b}(t) &= m_b(t).\frac{V_{DC}}{2} \\ V_{t,c}(t) &= m_c(t).\frac{V_{DC}}{2} \end{aligned} \tag{3.35}$$

Where subscripts a ,b and c stand for respective phases and the average bar is dropped for simplicity. And the corresponding modulating signals are 120 degrees shifted in phase with respect to each other:

$$\begin{aligned} m_a(t) &= \hat{m}(t).\cos[\varepsilon(t)] \\ m_b(t) &= \hat{m}(t).\cos[\varepsilon(t) - \frac{2\pi}{3}] \\ m_b(t) &= \hat{m}(t).\cos[\varepsilon(t) - \frac{4\pi}{3}] \end{aligned} \tag{3.36}$$

where $\varepsilon(t)$ contains the angular frequency and initial phase information. In this topology, if balanced modulating signals are provided, the three-phase voltages appear at the AC side inverter terminals. The phase and amplitude of the three-phase modulating signals in (3.36) can be modified to regulate the terminal voltages as desired.

3.3 AC Side Components

In this section the HESS AC side components model (which includes grid filter, household load and LV grid model) are explained.

3.3.1 Grid Filter

As it was discussed in Section 5.26, the three-phase three-level NPC inverter provides controlled switched voltages at its AC side terminals. Due to the switching nature of these voltages, inverter output current contains a wide range of harmonics. Thus, before interconnecting the NPC inverter with the grid, a low pass filter is required as an intermediate stage. This filter stage enables the HESS to meet the grid side current harmonic requirement.

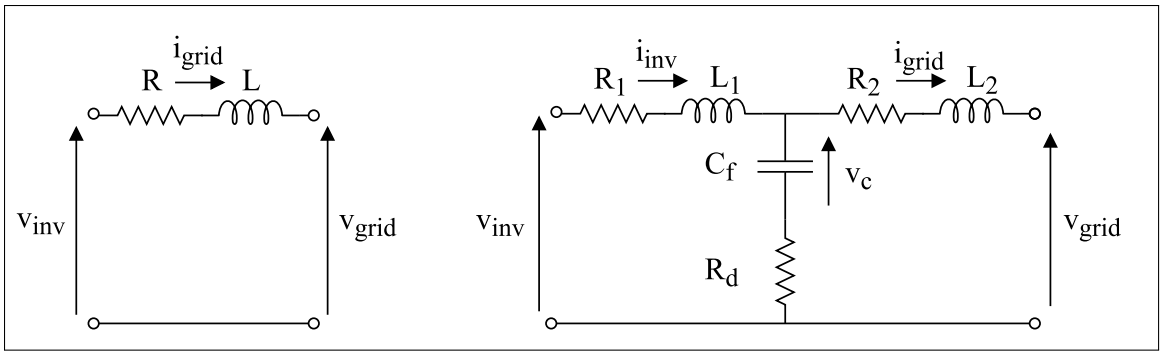

Figure 3-16: Per-phase grid filter circuit topologies, RL (left), LCL (right).

RL Filter

The simplest option for a grid filter is a RL filter. This topology (Fig. 3-16) requires a very simple control design, since the filter transfer function is first order.

$$H_{RL} = \frac{v_{inv}(s)}{i_{grid}(s)}\bigg|_{v_{grid}(s)=0} = \frac{1}{L.s + R} \tag{3.37}$$

The amplitude response of (3.37) decreases with -20 dB/dec for all the frequencies above the corner frequency. And it is suitable for very high switching frequency applications. But if faster dynamic response is required or lower switching frequency is chosen this filter will not be effective. Furthermore, the series resistance considerably increases filter losses. To counteract these issues the LCL topology can be adopted.

LCL Filter

The LCL filter topology is shown in Fig. 3-16. Its main advantage over RL filter is higher attenuation (-40 dB/dec) above the corner frequency. In order to derive the filter transfer function, let v_c , i_{inv} and i_{grid} be the state space variables, then state equations can be written as:

$$\begin{aligned}
\frac{dv_c}{dt} &= \frac{i_{inv} - i_{grid}}{C_f} \\
\frac{di_{inv}}{dt} &= \frac{1}{L_1}.(v_{inv} - v_c - R_d.(i_{inv} - i_{grid}) - R_1.i_{inv}) \\
\frac{di_{grid}}{dt} &= \frac{1}{L_2}.(v_c + R_d.(i_{inv} - i_{grid}) - v_{grid} - R_2.i_{grid})
\end{aligned} \tag{3.38}$$

And it can be expressed in matrix form as:

$$\frac{dx}{dt} = Ax + Bu \tag{3.39}$$

where:

$$x = \begin{bmatrix} \frac{dv_c}{dt} \\ \frac{di_{inv}}{dt} \\ \frac{di_{grid}}{dt} \end{bmatrix}, A = \begin{bmatrix} -\frac{R_1+R_d}{L_1} & \frac{R_f}{L_1} & -\frac{1}{L_1} \\ \frac{R_d}{L_2} & -\frac{R_2+R_d}{L_2} & \frac{1}{L_2} \\ \frac{1}{C_f} & -\frac{1}{C_f} & 0 \end{bmatrix}, B = \begin{bmatrix} \frac{1}{L_1} & 0 \\ 0 & \frac{-1}{L_2} \\ 0 & 0 \end{bmatrix}, u = \begin{bmatrix} v_{inv} \\ v_{grid} \end{bmatrix} \tag{3.40}$$

Then by setting the output to the desired state variable (in this case i_{grid}):

$$Y = Cx \quad , \quad C = \begin{bmatrix} 0 & 0 & 1 \end{bmatrix} \tag{3.41}$$

And assigning $v_{grid} = 0$, input voltage to output current transfer function is obtained:

$$H_{LCL} = \frac{v_{inv}(s)}{i_{grid}(s)}\bigg|_{v_{grid}(s)=0} = \frac{Y(s)}{U(s)} = [C(sI - A)^{-1}B] \tag{3.42}$$

Where I is the identity matrix. As R_1 and R_2 are the series resistances of the corresponding inductors and much smaller than the inductance values, they can be neglected. Now by setting the $R_d = 0$ (damping resistance) filter transfer function results in:

$$H_{LCL} = \frac{1}{(L_1.C_f.L_2).s^3 + (L_1 + L_2).s} \tag{3.43}$$

And if $R_d > 0$ damped filter transfer function is:

$$H_{LCL,damped} = \frac{C_f.R_d + 1}{(L_1.C_f.L_2).s^3 + (C_f.(L_1 + L_2)R_d).s^2 + (L_1 + L_2).s} \tag{3.44}$$

The reason why R_d is included in LCL topology is to passively cancel out the gain spike at resonant frequency and smooth out the phase to -180 degree for high frequencies. The magnitude and phase response of (3.37), (3.43) and (3.44) is shown in Fig. 3-17. The discussion presented for LCL filter corresponds to the y-connected three-phase filter in which capacitors are connected to the neutral. The same methodology can be also applied to delta-connected three-phase LCL filter to derive the corresponding transfer function. However, this results in different state space matrices [9].

LCL Filter Design

The LCL filter must meet a number of requirements such as maximum current ripple (ΔI_{Lmax}) as a percentage of the rated current. The desired harmonic attenuation factor k and the maximum power factor deviation x. These requirements help to find L_1 , L_2 and C_f respectively. In order to design filter parameters in the per-unit system, a base impedance and capacitance are defined as:

$$Z_{base} = \frac{V_{LL,rms}}{P_{rated}} \quad , \quad C_{base} = \frac{1}{2.\pi.f_{grid}.Z_{base}} \tag{3.45}$$

Where $V_{LL,rms}$ is the rated line-line RMS voltage at the inverter output, P_{rated} is the inverter rated active power, f_{grid} is the grid frequency. The filter capacitance is calculated as:

$$C_f = x.C_{base} \tag{3.46}$$

Moreover, the inverter output current ripple can be written as a function of L_1:

$$\Delta I_{Lmax} = \frac{2.V_{DC}.m.(1-m)}{3.L_1.f_s} \tag{3.47}$$

In which V_{DC} is DC link voltage, m is inverter modulation factor, f_s is inverter switching frequency. The worst case scenario for (3.48) happens for $m = 0.5$, consequently the maximum ripple is expressed by:

$$\Delta I_{Lmax} = \frac{V_{DC}}{6.L_1.f_s} \tag{3.48}$$

Assuming that i is the constant describing the ratio of the ripple and maximum current (I_{max}):

$$\Delta I_{Lmax} = i.I_{max} \tag{3.49}$$

Then the maximum current is calculated:

$$I_{max} = \frac{\sqrt{2}.P_{rated}}{3.V_{ph,rms}} \tag{3.50}$$

Where V_{ph} is the inverter phase voltage. Then by (3.48), (3.49) and (3.50) L_1 is designed. Now the required current harmonic attenuation can be used to design L_2. Let k be:

$$\frac{I_{gird}(h)}{I(h)} = k \tag{3.51}$$

Where $I(h)$ is the harmonic current generated by the inverter and $I_{grid}(h)$ is the corresponding harmonic portion injected to the grid. Then by adopting the equation presented in [9], L_2 is expressed:

$$L_2 = \frac{1 + \sqrt{\frac{1}{k^2}}}{C_f.(2.\pi.f_S)^2} \tag{3.52}$$

Now by having L_1, L_2 and C_f filter resonant frequency is identified as:

$$f_{resonant} = \frac{1}{2.\pi}.\sqrt{\frac{L_1 + L_2}{L_1.L_2.C_f}} \tag{3.53}$$

As a rule of thumb resonant frequency must lie in the following interval:

$$10.f_{grid} < f_{resonant} < 0.5.f_s \tag{3.54}$$

If this condition is not met at the end of design phase, the procedure should be repeated with modified values of x, i and k.

And the rule of thumb for designing R_d is:

$$R_d = \frac{1}{3.(2.\pi.f_{resonant}).C_f} \tag{3.55}$$

3.3.2 Household Load

In this thesis the household load model is developed by deploying a combination of three-phase balanced active and reactive power (P and Q) load model and three individual single-phase PQ loads. These load modules are interfaced via three single-phase circuit breakers. The actual load profile is fed to load profile generator block. This block decomposes the actual PQ profile into an approximate three-phase balance PQ load and three individual

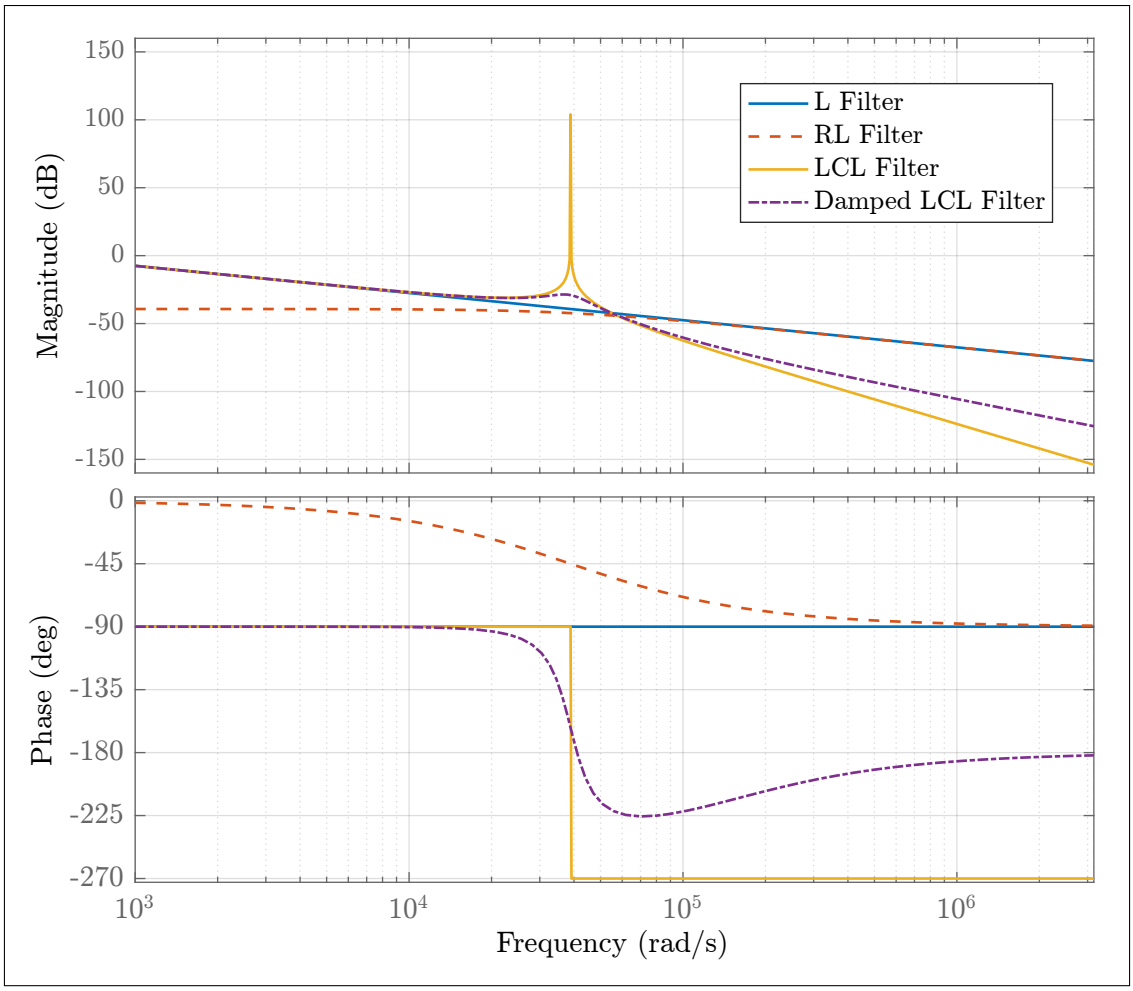

Figure 3-17: Grid filters frequency domain responses.

single-phase PQ values. Consequently, the corresponding PQ settings are fed into dynamic load modules. Moreover, the gating signals are sent to the single-phase breakers. The household load model scheme is illustrated in Fig. 3-18

3.3.3 Low Voltage Grid

The low voltage (LV) grid model consists of an ideal three-phase AC power source of 14.4 kV and 50Hz. Moreover, a typical pole-mounted transformer 150 kVA is included for every single phase. The generation side and the transformer have grounded star connections. This configuration imposes a set of three-phase voltage of 240 V and 50 Hz at PCC. This model is considered to be an stiff equivalent of actual LV network. In other words the grid voltage and frequency dynamics are neglected.

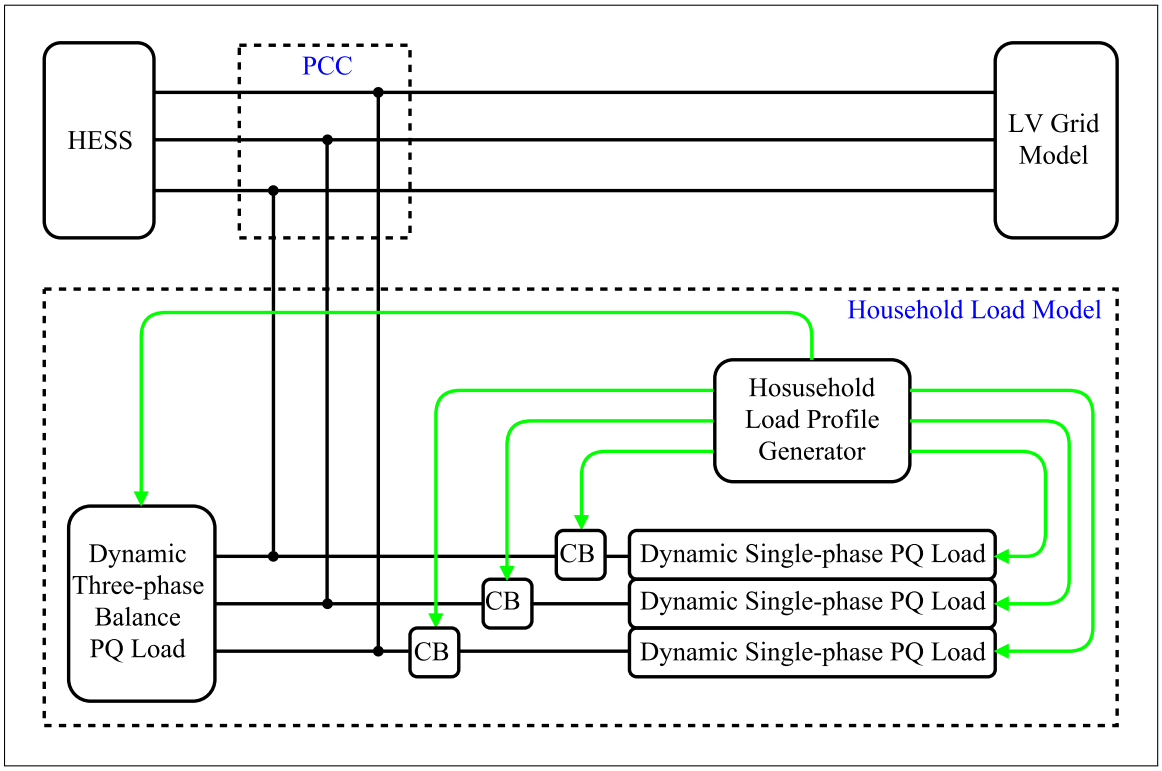

Figure 3-18: Household load model.

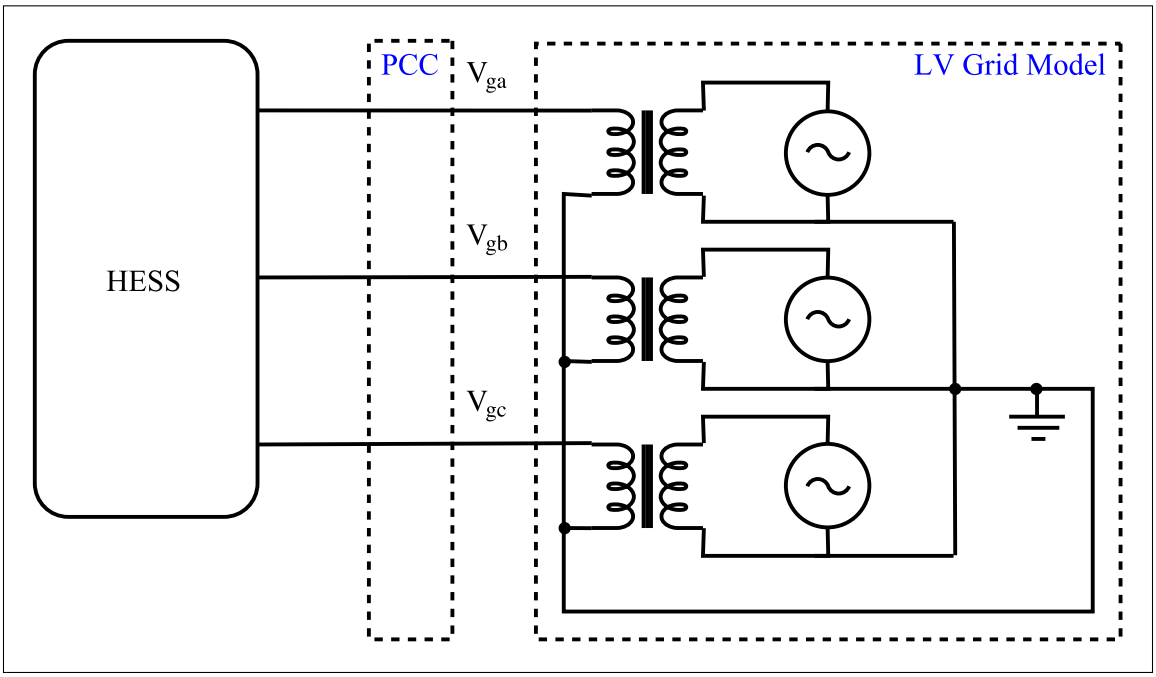

Figure 3-19: Ideal LV grid model.

Chapter 4

HESS Functionalities

In this chapter the required functionalities which the HESS model must provide are introduced. Firstly, the DC side functions are presented and consequently the AC side functions are discussed.

4.1 DC Side Functions

The HESS DC side must perform three main functionalities: The first is maximizing the PV generated power, second one is controlling the BESS SoC level And the third functionality is regulating of the overall DC power according to the HESS AC side demand.

4.1.1 Maximum Power Point Tracking

Regarding the deploying HESS as the only power source in the household, the main issue is the high installation cost even for the smallest sizing. One way to address this issue is to take very deep consideration for system sizing (PV size, battery and inverter rating). And moreover, whatever sizing is chosen for the system, it must be operated with the highest possible efficiency. Thinking about PV in this sense, leads to the idea of possibly extracting the maximum available PV energy. As it was mentioned in Chapter 3 the maximum power point (MPP) of the PV varies according to the uncontrollable irradiance and temperature inputs. If these variables change simultaneously then the MPP can move in a wide range. Therefore, due to this deviation, the direct connection of the PV to the next stage can influence the HESS efficiency to a great extent. This is shown in Fig. 4-1 in which the $P-V$ curves under irradiance variation are depicted for the PV-battery connection. The

crossing point between battery voltage and the $P-V$ curves defines the operating point, which can be far from MPP.

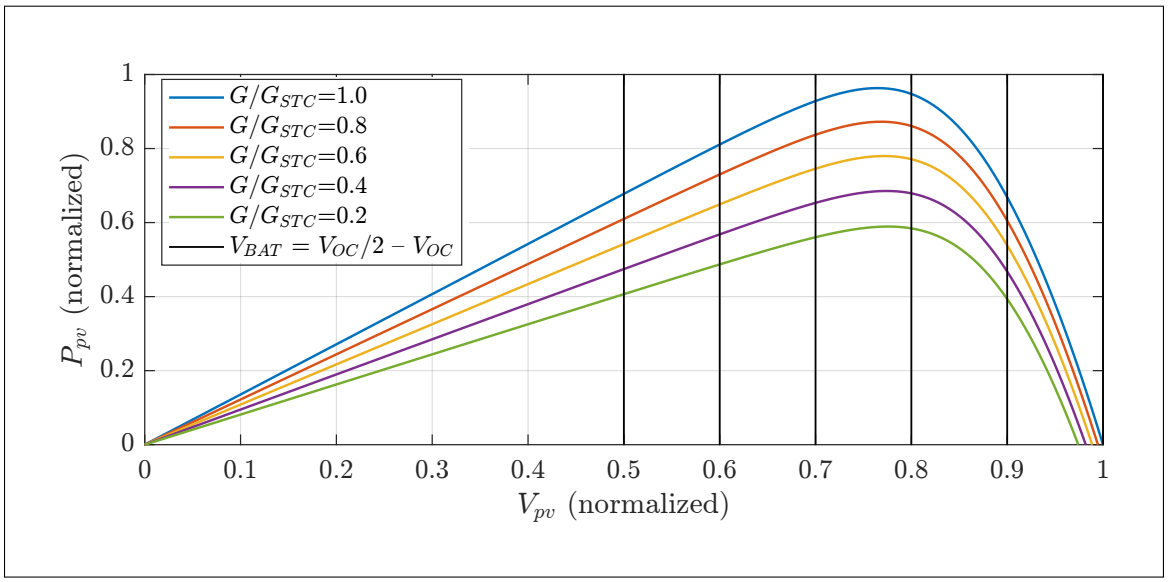

Figure 4-1: $P-V$ curve operating point shift due to the battery terminal voltage variation.

In fact, letting the PV terminal voltage be imposed by the output stage without any further regulation can technically shift the operating point far away from MPP. Therefore the PV system requires an intermediate interface which dynamically adjusts the PV terminal voltage such that the operating point stays as close as possible to the MPP. This regulating technique is known as the maximum power point tracking(MPPT). The simplest way to implement MPPT is to consider a DC - DC converter (Fig. 4-2) between PV and the output stage. Then the converter duty cycle can be considered as a control input to regulate PV voltage by adjusting the converter voltage gain m:

$$V_i = \frac{V_o}{m} \tag{4.1}$$

MPPT can be classified as a dynamic optimization problem, in the sense that the converter duty cycle must be modified simultaneously, therefore it continuously perturbs the PV terminal voltage. As it is proposed by [1] another option for maximizing PV efficiency is to maximize the DC - DC converter efficiency. Hence, shifting the optimization objective to the converter output power. The main problem of this approach is that by having variations in temperature and irradiance the converter operating point also changes. This can move

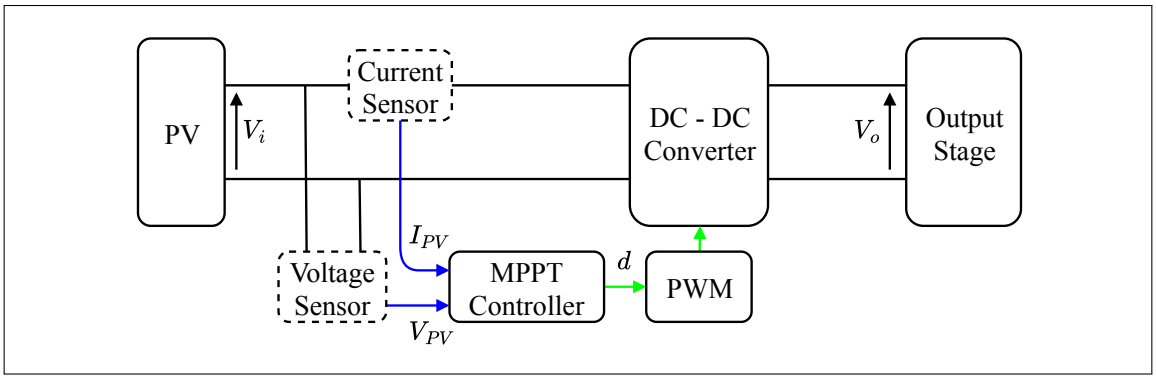

Figure 4-2: PV system interfaced with DC - DC converter as the dynamic PV power optimizer.

the converter operating point far from region of high efficiency. Taking the efficiency profile of the converter into account, there must be a coordination in converter design and the PV estimated maximum power, so that the extraction of maximum PV power by MPPT does not drift the converter operating point out of its efficient band. In the following, a couple of MPPT algorithm is introduced.

Perturb and Observe Method

Usually the temperature and irradiance measurements are not available in PV systems, therefore the majority of MPPT algorithms are designed based on PV current and voltage measurements. The principle idea behind the perturb and observe (P&O) algorithm is that the MPPT controller perturbs one of the system variables in order to change the operating point over time until it hits a maximum. In P&O algorithm the perturbation either directly or indirectly changes the PV output voltage. As it is shown in Fig. 4-2 this can be done by dynamically perturbing the converter duty cycle which consequently perturbs PV voltage based on (4.1). In this case, after the first perturbation the MPPT controller calculates the PV power by having the current and voltage feedbacks. If the PV power had been increased, that means the voltage perturbation was on the right direction (moving the operating point close to MPP). And the next perturbation will be on the same direction (either increasing or decreasing) as long as the PV power increase. When PV power decreases, the algorithm reverses the direction. This algorithm which offers a very simple and robust solution is shown in Fig. 4-3, where x is the perturbed system variable. The P&O influence on the PV operating point is depicted in Fig. 4-4. It shows that depending on the initial operating

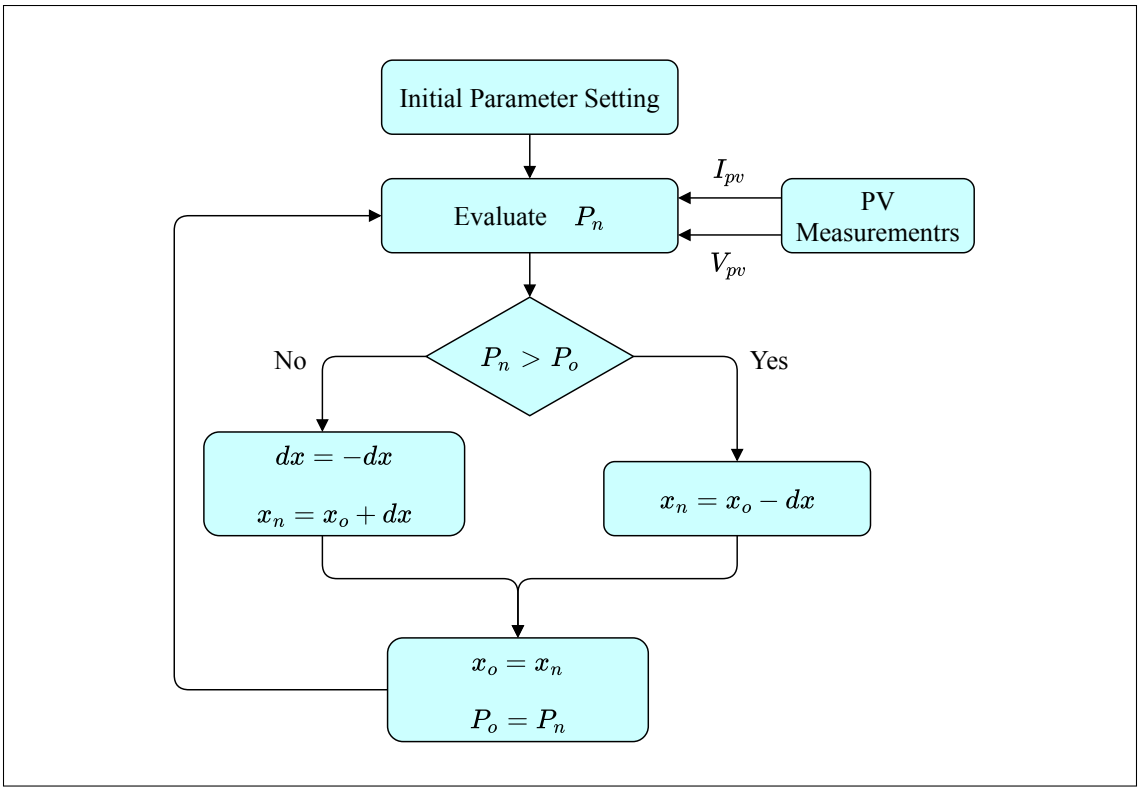

Figure 4-3: P&O algorithm flowchart, subscript n and o stand for new and old values.

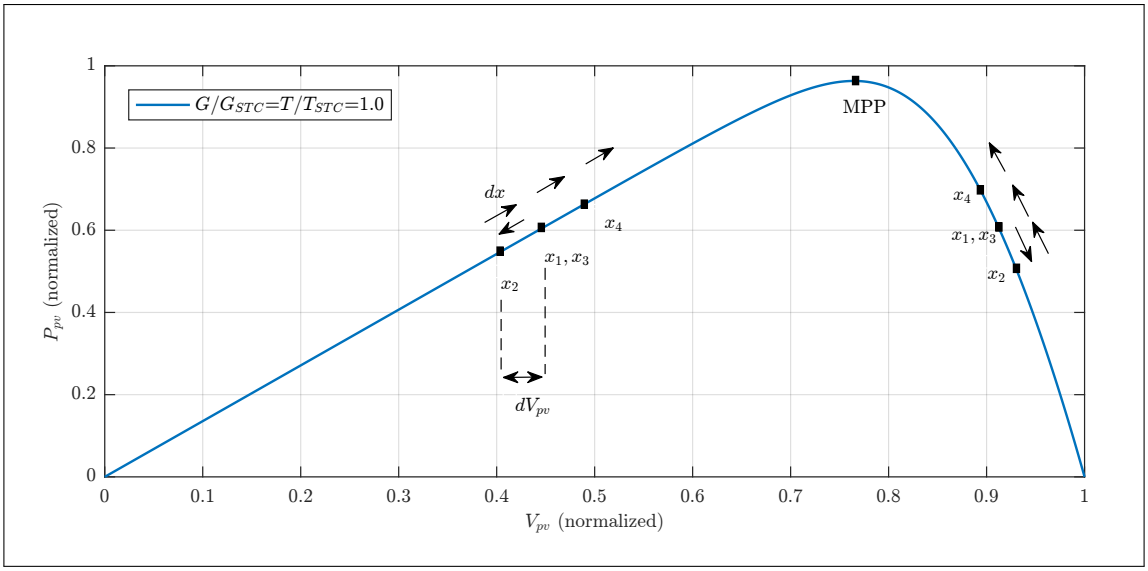

Figure 4-4: P&O influence on PV operation point based on the starting point.

point (left or right side of MPP) and the perturbation direction, four possible scenarios exits which all have to be addressed in order to reach and continue to track MPP.

Incremental Conductance Method

Incremental conductance (IC) MPPT algorithm takes the slope of the $P-V$ curve into account and translates the MPP occurrence into the following equation:

$$\frac{dP}{dV} = \frac{V.I}{dV} \tag{4.2}$$

And since PV current depends on the voltage variation, by taking the partial derivatives of (4.2):

$$I + V.\frac{dI}{dV} = 0 \tag{4.3}$$

Which can be reformulated to:

$$\frac{I}{V} = -\frac{dI}{dV} \tag{4.4}$$

Thus the algorithm reaches MPP when the condition (4.4) is valid, where the left hand side term is conductance G and the right hand side term is the incremental conductance dG. This algorithm has also a perturbating nature, in the sense that the PV voltage is dynamically perturbed with a reasonable step size. And then the value of G before perturbation will be compared with the value of dG after the perturbation, and the MPP is reached when these to values are the same for two consecutive time instants:

$$\frac{I_k}{V_k} = -\frac{I_k - I_{k-1}}{V_k - V_{k-1}} \tag{4.5}$$

Where the subscripts k and $k-1$ stand for two consecutive time instants. IC also recognizes if the operating point is on the left or right side of the MPP. By recalling (4.2) and (4.3) it is possible to rewrite $\frac{dP}{dV}$ in terms of G and dG:

$$\frac{1}{V}.\frac{dP}{V} = \frac{I}{V} + \frac{dI}{dV} = G + dG \tag{4.6}$$

If the operating point is on the left side of MPP (4.6) results in $G + dG > 0$ and on the right side of MPP where the power derivative is negative (4.6) results in $G + dG < 0$. This information is the key criteria to choose the right direction for the next voltage perturbation. The IC algorithm flowchart is shown in Figure 4-5.

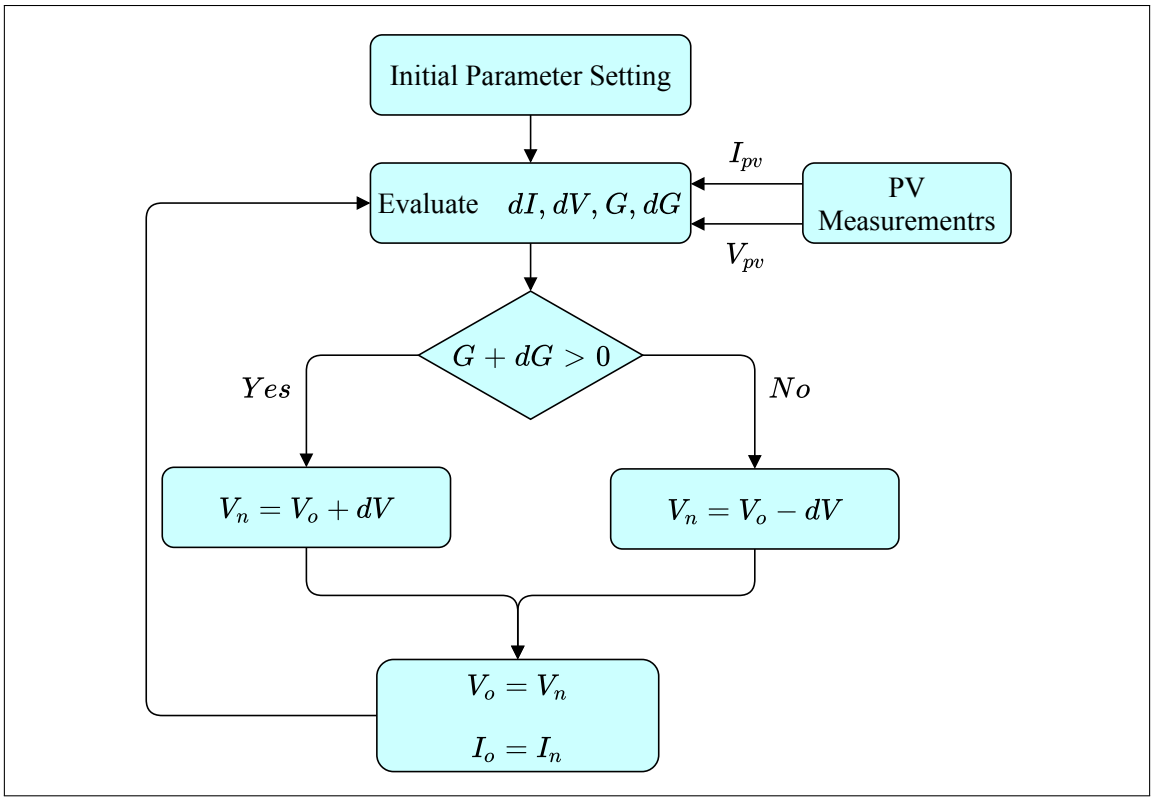

Figure 4-5: IC algorithm flowchart, subscript n and o stand for new and old values.

4.1.2 Battery Charge-Discharge Management

HESS system requires a strategy to control BESS depth of discharge and maximum charge level. The controlling scheme is called battery charge-discharge management (CDM). This scheme receives the BESS SoC as the input, and accordingly identifies the BESS possible operational states. Initially, the upper and lower SoC limits are identified. Then the CDM scheme evaluates two BESS charge and discharge enables, C_{en} and D_{en} respectively. The CDM scheme logic uses the following conditional statements to evaluate C_{en} and D_{en}:

- if $SoC \geq SoC_{max} \implies C_{en} = 0$ and $D_{en} = 1$
- if $SoC_{min} < SoC < SoC_{max} \implies C_{en} = 1$ and $D_{en} = 1$
- if $SoC \leq SoC_{min} \implies C_{en} = 1$ and $D_{en} = 0$

Thus, if the current SoC level is above the upper limit, CDM does not allow any further charging (C_{en}=0) and it allows the BESS to discharge (D_{en}=1). And if the SoC in within the limits, both charge and discharge operation are possible (C_{en}=1 and D_{en}=1). Similarly, if the SoC is bellow the lower limit, no further discharge is allowed (D_{en}=0) and the charging

operation is permitted (C_{en}=1). The input and output of the CDM scheme are shown in Fig. 4-6, in which the upper and lower SoC limits are 90 and 10 percent respectively. These

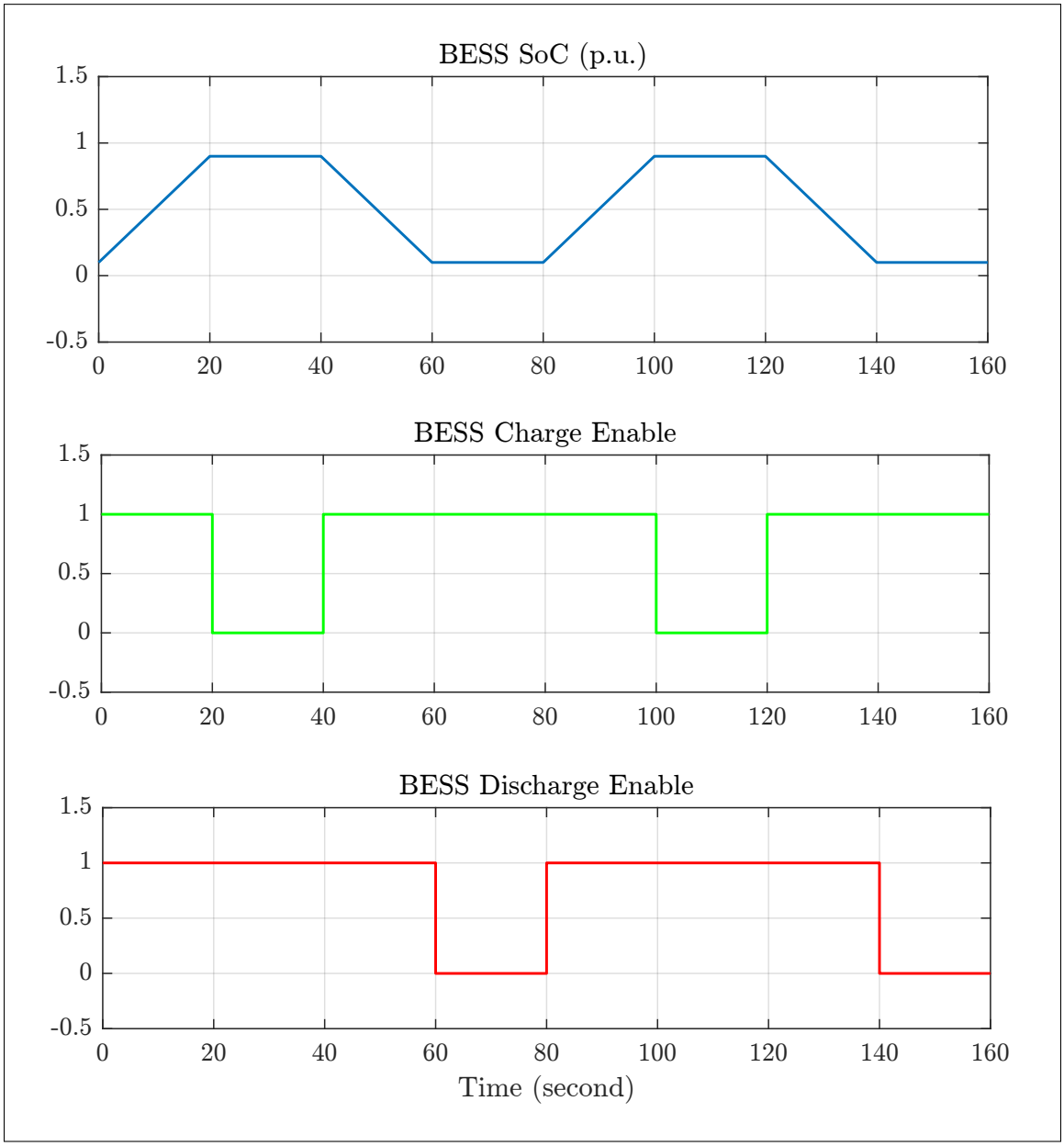

Figure 4-6: CDM scheme input and outputs.

outputs are fed to another logic scheme which generates the BESS reference current. This auxiliary scheme also considers other factors which influence the desired BESS current such as PV power, load requirements and grid active power injection. This scheme is discussed in Section 5.3.3.

4.1.3 DC Power Regulation

As it was previously mentioned, regarding the PV power generation, the most important consideration is to extract maximum available PV power. This is done by MPPT implementation presented in Chapter 5. One of the issues regarding the PV power is the fact that it can not exactly follow the household load profile. Thus, BESS is considered as the regulatory DC power source. This implies that the extracted power from BESS is adjusted according to the PV measurements and household load profile. Hence, the combination of PV and BESS powers can perfectly match the required power demand on the HESS AC side. This functionality can be implemented by identifying the BESS charge-discharge current according to the power difference between PV and AC side demand. Thus, this feature can be embedded in BESS reference charge-discharge current generation which is discussed in the next chapter.

4.2 AC Side Function

In this section the HESS model AC side function is introduced. This functionality involves in controlling all the possible power flow exchanges between HESS and LV grid.

4.2.1 HESS-Grid Active and Reactive Power Exchange

In this section a couple of fully controlled power exchange modes between HESS and LV grid are introduced. And due to the similar nature of these power exchange modes, their corresponding control schemes are combined in an overall scheme which is presented in Section 5.3.2.

Grid Power Injection-Absorption (GPIA)

For all the HESS applications it is necessary for the system to have absolute control on the active and reactive power (P_{grid} and Q_{grid} in Fig. 4-7) which is injected to or absorbed from the grid. This is particularly important to optimize the possible financial benefits for the HESS owner. Since, the grid side offers different tariffs for buying power from household PV installations. So it might bring more benefits to the HESS owner to inject excess PV generated power into the grid on specific days of a week or at specific hours of a day. Moreover, sometimes the excess PV power is available and the grid side does not allow any

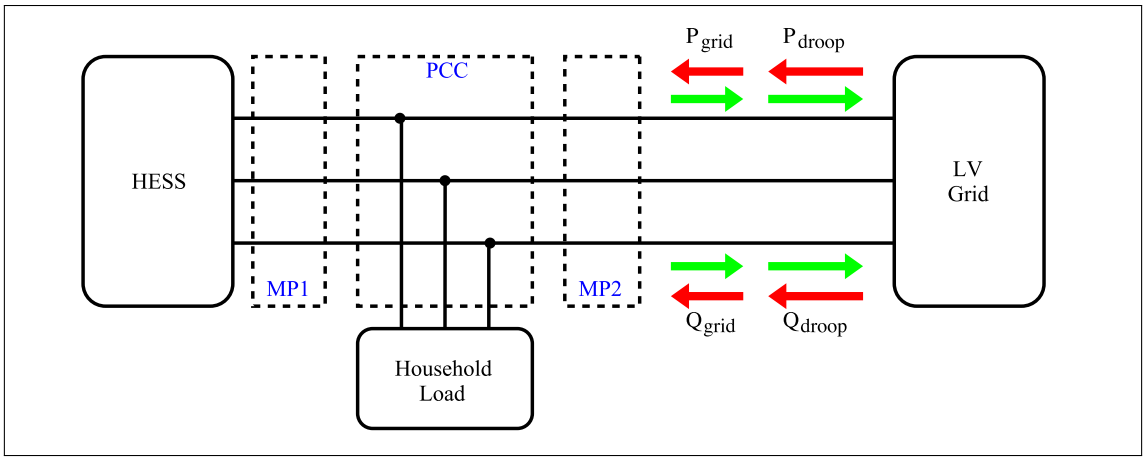

Figure 4-7: HESS-grid active and reactive power exchange.

power injection. This limitation might be imposed due to the overall LV grid operational state in terms of voltage and frequency stabilities.

The GPIA is required in the some HESS operational states. For instance, if the household load profile exhibits a gradient which is faster than HESS power delivery response time. In this case, inevitably the load is supplied by the LV grid during the transient state. The other scenario, in which the GPIA is required, is when there is not enough available DC (Overall BESS and PV) power to respond the household demand. Additionally, GPIA might be required to charge BESS so that it maintains the SoC level above the lower SoC limit if there is not enough sunlight for consecutive days. Thus, controlling the GPIA is one of the crucial AC side functionalities to be considered in overall HESS control design.

Grid Frequency-Voltage Regulation (GFVR)

In the case of interfacing HESS with an actual non-stiff grid which may impose voltage-frequency dynamics in the transmission system, HESS can provide some assistance in stabilizing grid voltage and frequency (Fig. 4-7). This auxiliary feature aims to mimic the role of a governor controller for conventional generators. In conventional generators if the active power demand increases from the set point P_0 to P accordingly then the governor lets the frequency drop from its set point f_0 to f which is illustrated in Fig. 4-8. This demonstrates the inherent governor trade-off between the power demand and frequency accuracy. However, when the power demand transient is finished, the governor will recover the

generator frequency to its original set point. Th similar argument is valid for the generator terminal voltage variation with respect to the generator reactive power demand. For this

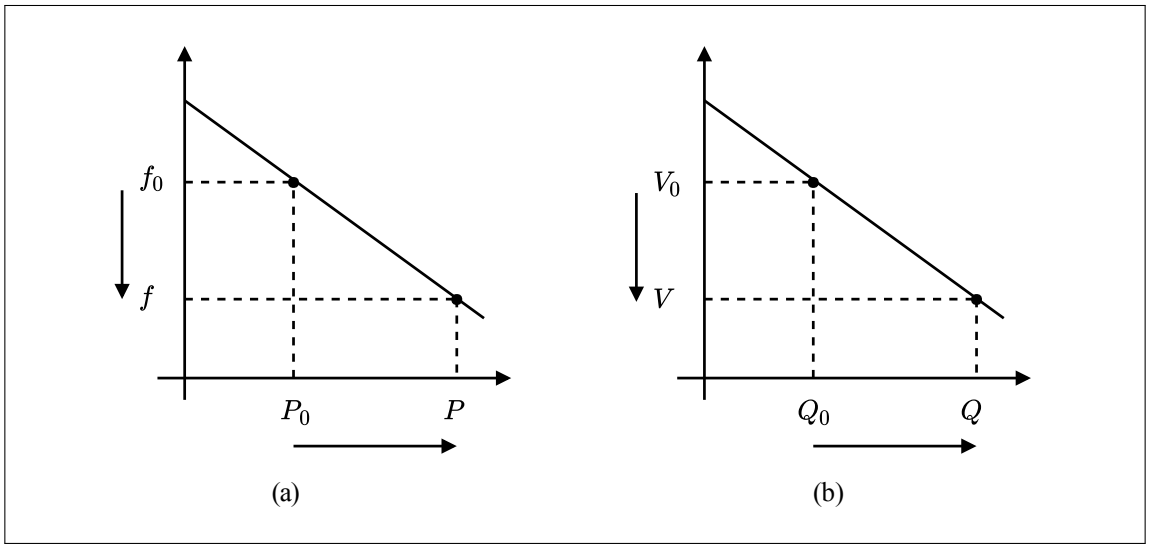

Figure 4-8: Frequency and voltage droop characteristics.

to be done it is required to consider the AC power flow from HESS to the LV grid through a transmission line section. As a result of the argument presented in Appendix A.4, the power angle δ and voltage difference $V_1 - V_2$ over a line segment ends can be approximated by:

$$\begin{aligned} \delta &\cong \frac{X.P}{V_1.V_2} \\ V_1 - V_2 &\cong \frac{X.Q}{V_1} \end{aligned} \tag{4.7}$$

Where V_1, V_2 and X are the sending voltage, receiving voltage and line inductance respectively. Therefore, by implication of swing equation, frequency is related to power angle. Thus, the active and reactive powers flowing through the line segment can regulate the frequency and voltage at the line end. Thus, if the grid requires excess active and reactive power to stabilize its frequency and voltage, this can be provided by HESS. Based on the grid side requirement HESS can inject or absorb active and reactive power (P_{droop} and Q_{droop} shown in Fig. 4-7). The implementation of combined GFVR and GPIA functionality is discussed in the next chapter.

Chapter 5

HESS Control Design

In this chapter all the control schemes which are necessary for a HESS to be able to provide the previously mentioned functionalities are discussed in detail. Firstly, the control schemes which influence the HESS DC side are presented. Afterwards, the AC side controllers are discussed. It must be taken into account that all the control schemes are designed in per-unit system based on Appendix A.2. Thus, the HESS can be easily scaled up to simulate the behaviour of higher power components (i.e. grid central storage).

5.1 DC Side Control Design

DC side control design includes the implementation of the PV maximum power point tracking (MPPT) and the BESS charge-discharge controller (CDC) which contributes to the BESS current controll.

5.1.1 Maximum Power Point Tracking

In this section the implementation of P&O MPPT algorithm is discussed. For this to be done, a DC - DC converter with the same topology as the model presented in Section 3.1 is adopted. P&O MPPT implementation can be done by direct perturbation of the converter duty cycle (Fig. 4-2). However, also a PI-based implementation exists. In this case the P&O algorithm generates a reference voltage, which is compared to the actual PV voltage. Therefore the generated error signal is processed by the PI controller to regulate the duty cycle. In this thesis the direct implementation is presented. P&O method can be expressed

by the following equation:

$$X((n+1)T) = X(nT) + (X(nT) - X((n-1)T)).sign[P(nT) - P((n-1)T)] \quad (5.1)$$

Where X is the parameter which is perturbed, and T is the perturbation time interval (in the sense of implementation this is the algorithm sample time), and the difference between the current and previous samples is considered as the perturbation amplitude dX. It is crucial to consider the system's time response to any perturbation. In other words, if the converter duty cycle is perturbed, what the corresponding settling time T_s is for PV voltage to reach the steady state value. If the perturbation time interval is smaller than T_s that means the system is re-excited before reaching the steady state according to the previous perturbation. This causes noise in MPPT controller which in turn affects the PV efficiency. Therefore to analyze the system time response it is necessary to derive the transfer function of the PV voltage over the converter duty . This is presented in [1], which employs the PV and the converter output stage small signal models to formulate this transfer function. According to [1] this is a stable second order transfer function stated by:

$$G_{pv,d}(s) = \frac{V_{pv}(s)}{d(s)} = \frac{\mu.\omega_n^2}{s^2 + 2\zeta.\omega_n.s + \omega_n^2} \quad (5.2)$$

Where the natural frequency ω_n, static gain μ and damping factor ζ are evaluated according to the converter and the output stage parameters. PV voltage to duty cycle perturbation response under STC is shown in Fig. 5-2. In this example the transfer function parameters are evaluated for PV-battery charger circuit. The small signal model of this circuit is shown in Fig. 5-1. The small letters identify the small signal variation of duty cycle and PV voltage. The small signal modeling for the converter non-liner components is done based on the discussion in Section 3.1.3. Moreover, it is considered that the battery is ideal therefore its small signal variation can be neglected ($v_{bat} = 0$). Consequently by circuit analysis the parameter in (5.2) can be evaluated as following:

$$\mu = V_{bat}, \omega_n = \frac{1}{\sqrt{L.C_{in}}}, \zeta = \frac{1}{2.R_{MPP}}.\sqrt{\frac{L}{C_{in}}} + \frac{R_{Cin} + R_L}{2}.\sqrt{\frac{C_{in}}{L}} \quad (5.3)$$

Where V_{bat} is the battery nominal voltage and $R_{MPP} = \frac{V_{pv,MPP}}{I_{pv,MPP}}$. It should be taken into account that the R_{Cin} introduces a high frequency zero to the system which will not

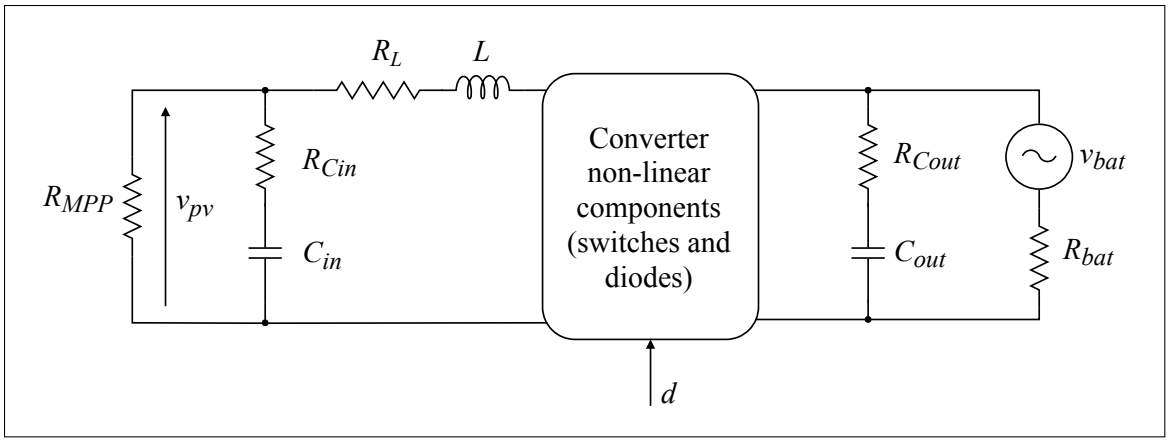

Figure 5-1: PV battery charger small signal equivalent circuit.

influence the dynamics considerably. One of the main disadvantages of P&O method is the steady state oscillation around the MPP point. Which is due to the fact that very close to MPP with one perturbation the operating point can shift from the left side of MPP to the right side and vice versa (Fig. 5-3).

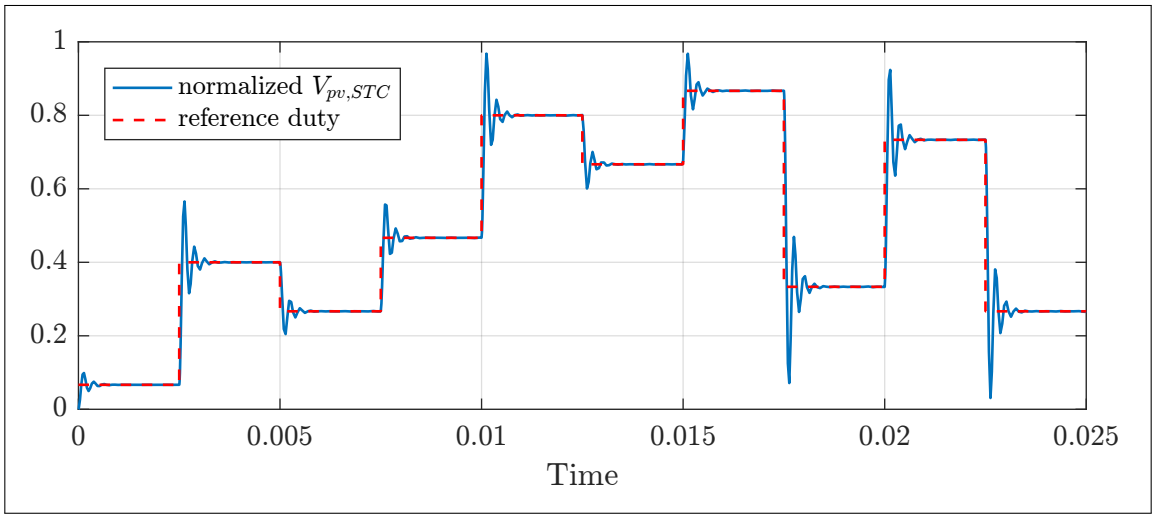

Figure 5-2: PV voltage response to P&O duty cycle perturbation

Although this can be improved by reducing the perturbation amplitude. It is shown in [1] that the IC method improves the PV efficiency by addressing this issue. Fig. 5-4 compares the efficiency of these methods under changing irradiance input and STC temperature.

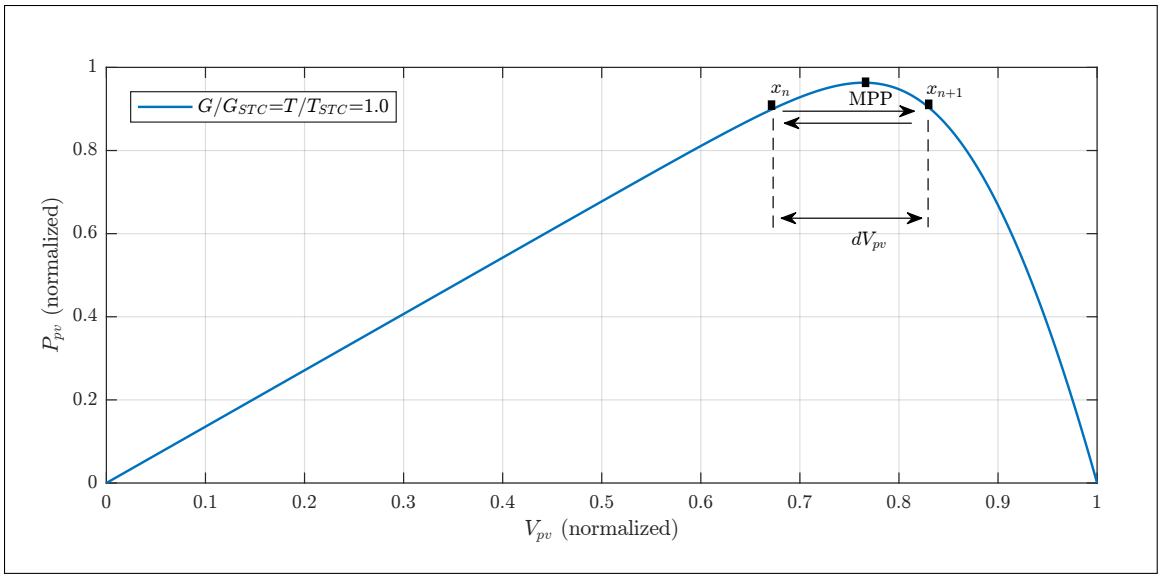

Figure 5-3: P&O Oscillation around MPP.

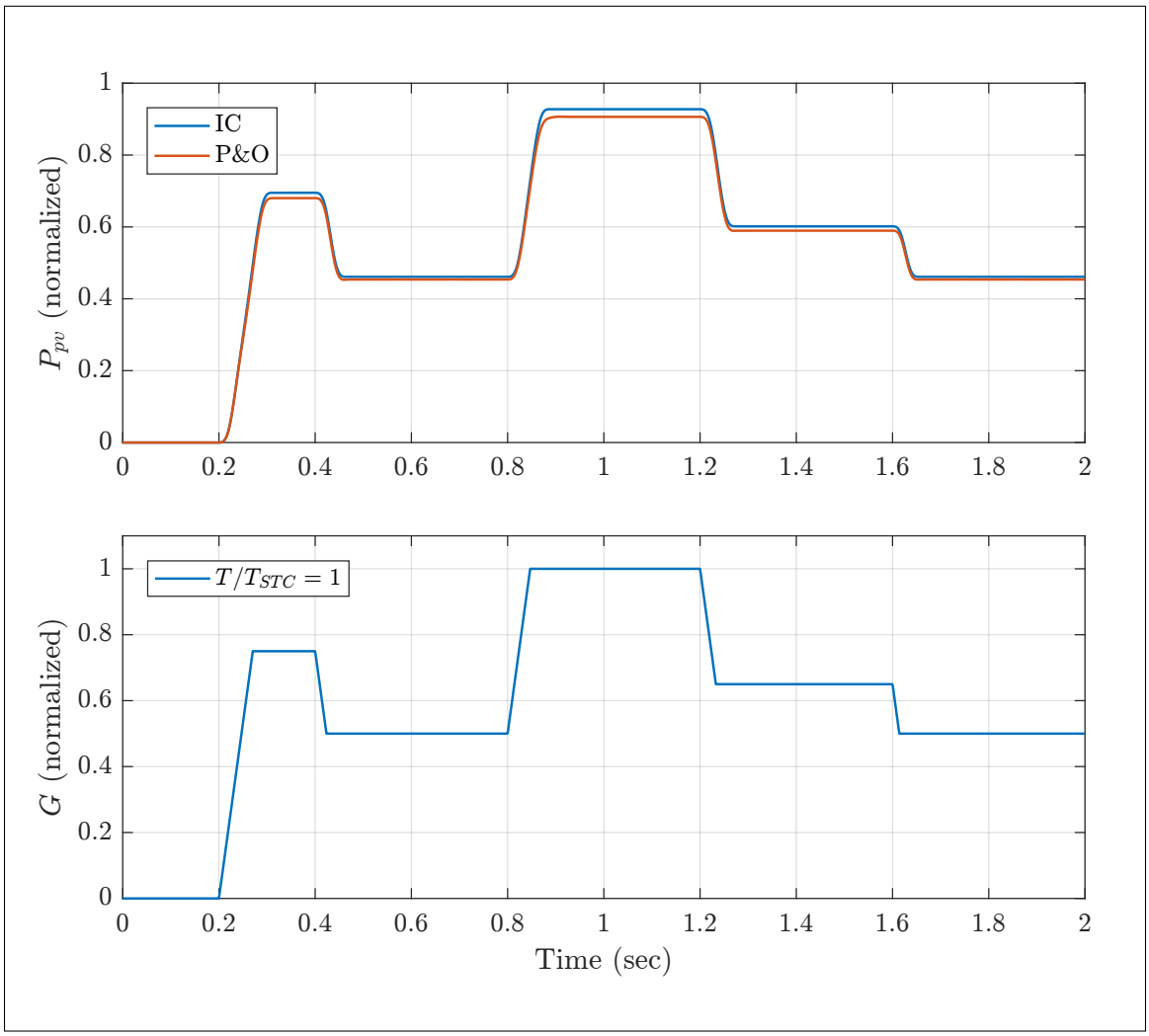

Figure 5-4: PV power with IC and P&O MPPT methods (top), irradiance profile (bottom).

5.1.2 Battery Charge-Discharge Controller

In this section the PI implementation of CDC for the BBBC model expressed by transfer function (3.27) is discussed. As it was demonstrated in Section 3.1.4, the objective is to control the battery current in charge and discharge operation modes. Thus, by recalling (3.27):

$$G_{i_L d} = \frac{i_L(s)}{d(s)} = \frac{V_{DC}}{L.s + R_L} \tag{5.4}$$

The transfer function of the BEES current over the BBBC duty, expresses a first order minimum phase system. To control the system, PI controller is adopted and the zero-pole cancellation method is applied. The PI controller has the form:

$$PI(s) = K_p + \frac{K_i}{s} \tag{5.5}$$

System (5.4) has a pole at $s = -\frac{R_L}{L}$. This pole can be fairly close to the origin so it must be cancelled out by the PI zero, therefore:

$$\frac{K_i}{K_p} = \frac{R_L}{L} \tag{5.6}$$

Now by inserting (5.6) in (5.5) and multiply the result with (5.4) the loop gain will be:

$$L(s) = \frac{K_p.V_{DC}}{L.s} \tag{5.7}$$

Consequently, the closed loop transfer function is deduced:

$$G(s) = \frac{L(s)}{1 + L(s)} = \frac{K_p.V_{DC}}{L.s + K_p.V_{DC}} \tag{5.8}$$

Which can be written as:

$$G(s) = \frac{1}{\tau.s + 1} \quad \text{where} \quad \tau = \frac{L}{K_p.V_{DC}} \tag{5.9}$$

And the closed loop time constant τ can be expressed in terms of closed loop bandwidth f_{bw} as $\tau = \frac{1}{f_{bw}}$ Therefore, K_p and K_i can be tuned to achieve the required bandwidth for

the charge-discharge current control:

$$K_p = \frac{L.f_{bw}}{V_{DC}} \quad \text{and} \quad K_i = \frac{R_L.f_{bw}}{V_{DC}} \tag{5.10}$$

The battery current to duty transfer function (5.4) and tuned system responses (5.8) are shown in Fig. 5-5, where the desired bandwidth is 1000 Hz. It must be noted, that τ should be considerably small therefore the CDC provides a fast current regulation. On the other hand the closed loop bandwidth f_{bw} must be significantly smaller than the converter switching frequency, thus any changes in the CDC output can be applied to the system simultaneously. The output of the CDC regulates the inductor voltage in Fig. 3-9. Therefore, corresponding gating signals S_1 and S_2 for switches Q_1 and Q_2 must be generated via PWM. This CDC schematic diagram alongside the PWM scheme is shown in Fig. 5-6.

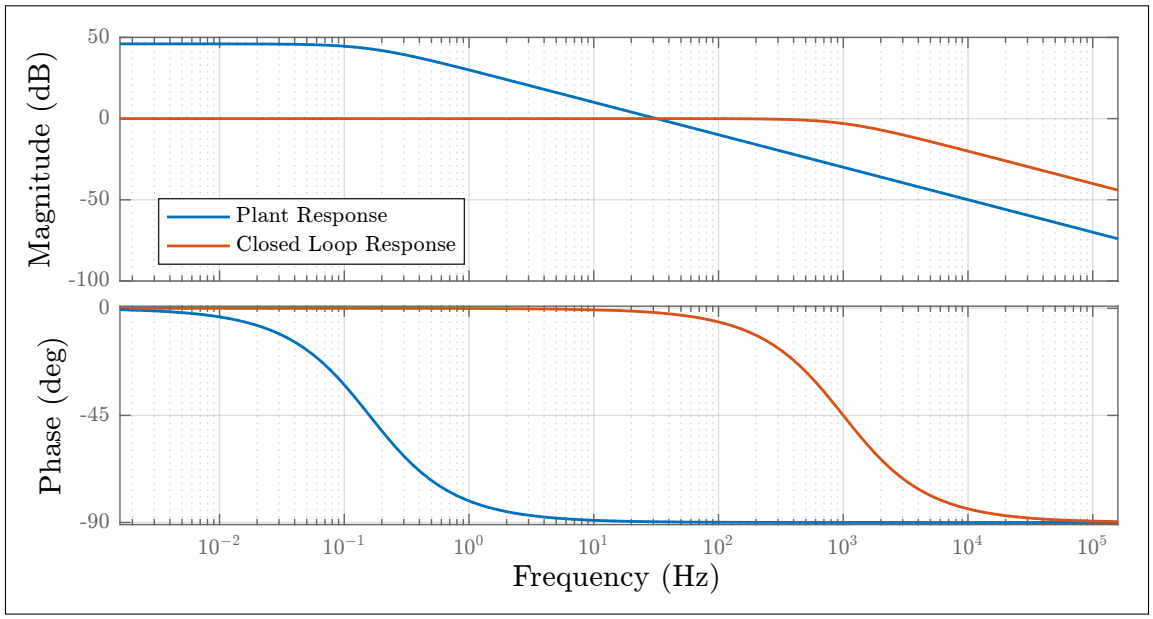

Figure 5-5: BESS CDC bode plots.

5.2 AC Side Control Design

The AC side controlling schemes include power flow control (PFC) which itself consists of inverter current controller (ICC) and the DC link voltage controller (DCVC). Moreover, a phase locked loop (PLL) is included as a necessary part to realize the PFC implementation in synchronous reference frame.

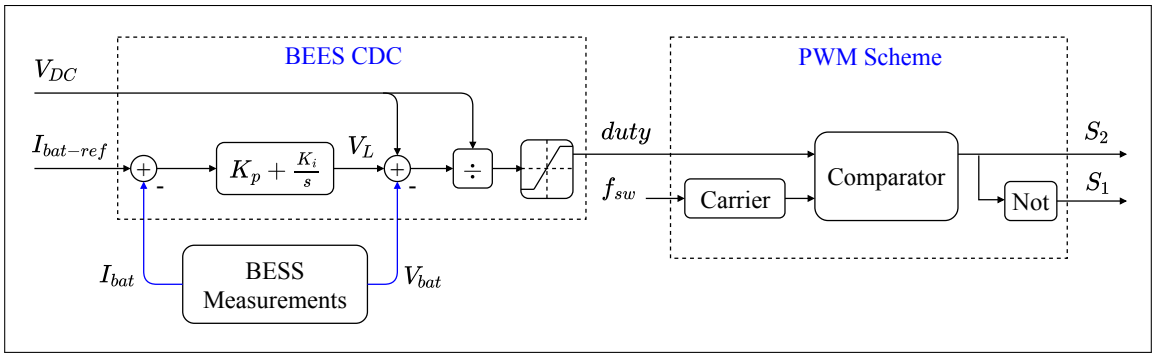

Figure 5-6: BESS CDC scheme cascaded with the PWM generation.

5.2.1 Power Flow Control

One of the main design requirements of HESS is to have direct control over the active P and reactive power Q flows at the AC side. In other words, HESS should be able to dynamically control the apparent power S injected to or absorbed from the AC side by the inverter stage. The schematic diagram of HESS AC side is shown in Fig. 5-7. The approach which is adopted in this thesis is to control the inverter terminal currents. More specifically, the three-phase current amplitude and its phase can be regulated with respect to the voltage imposed by grid at the PCC. Thus P, Q and consequently S are controlled. The other scheme might be controlling the power flow via controlling the inverter terminal

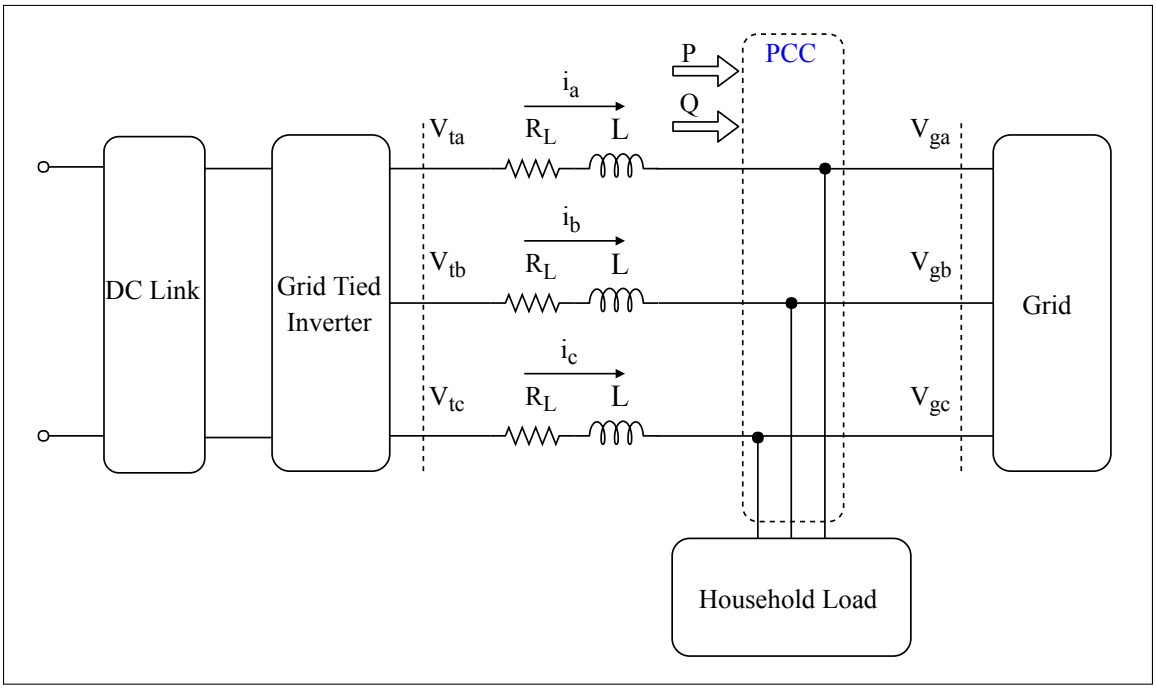

Figure 5-7: HESS AC side schematic diagram.

voltage [10]. In the following the dynamic model of the HESS AC side shown in Fig. 5-7 is discussed. Firstly, a brief introduction on three-phase voltage space phasor derivation in stationary ($\alpha\beta$) and arbitrary (dq) frames is presented. Afterwards, the dynamic model is formulated, and then the PFC scheme is designed by the means of PLL synchronization mechanism [8].

Space Phasor in $\alpha\beta$ and dq Frames

Let the generic three-phase voltage be represented by:

$$\begin{aligned} V_a(t) &= \hat{V}.\cos[\omega_0 t + \theta_0] \\ V_b(t) &= \hat{V}.\cos[\omega_0 t + \theta_0 - \frac{2\pi}{3}] \\ V_c(t) &= \hat{V}.\cos[\omega_0 t + \theta_0 - \frac{4\pi}{3}] \end{aligned} \tag{5.11}$$

In which $\hat{V}$ is the voltage amplitude, ω_0 is the angular frequency and θ_0 is the initial phase angle. Then the equivalent space phasor is introduced by:

$$\vec{V}_{abc}(t) = \frac{2}{3}\left[e^{j0}.V_a(t) + e^{j\frac{2\pi}{3}}.V_b(t) + e^{j\frac{4\pi}{3}}.V_c(t)\right] \tag{5.12}$$

Then by substituting (5.11) in (5.12):

$$\vec{V}_{abc}(t) = \left(\hat{V}.e^{j\theta_0}\right)e^{j\omega_0 t} \tag{5.13}$$

As it is illustrated in Fig. 5-8 the space phasor rotates with angular frequency ω_0. Thus, its phase angle difference with α axis has a time variant nature. At t_1 instant of time this phase angle is defined by:

$$\theta(t = t_1) = \theta_1 = \omega_0 t_1 + \theta_0 \tag{5.14}$$

Consequently the $\vec{V}_{abc}$ can be projected on the $\alpha\beta$ axes at every time instant t:

$$\vec{V}_{abc}(t) = V_\alpha + jV_\beta \tag{5.15}$$

Where:

$$V_\alpha = \left(\hat{V}e^{j\theta_0}\right).\cos[\theta(t)] \quad \text{and} \quad V_\beta = \left(\hat{V}e^{j\theta_0}\right).\sin[\theta(t)] \tag{5.16}$$

Which proves the fact that the rotating space phasor components on the stationary frame have AC nature. And as it is depicted in Fig. 5-8 the phase angle between the $\alpha\beta$ frame

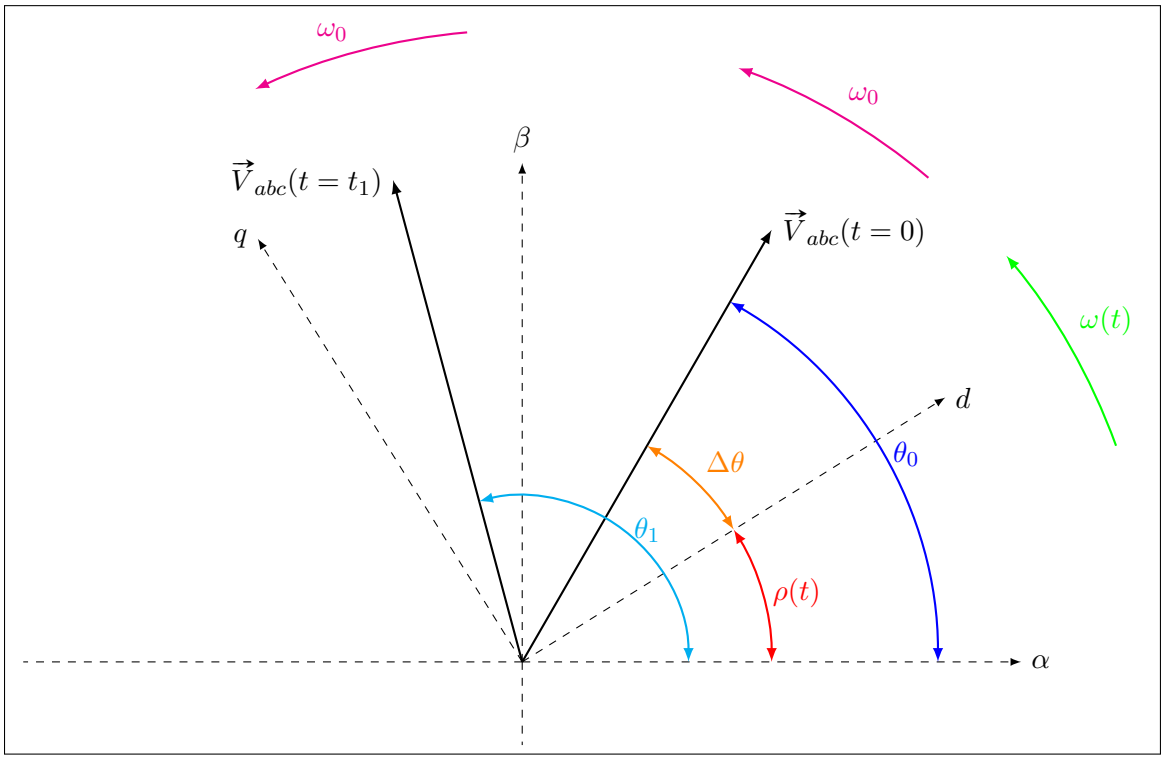

Figure 5-8: Three-phase voltage space phasor in dq and $\alpha\beta$ reference frames.

and the arbitrary the dq frame is defined by $\rho(t) = \omega(t).t$, where ω is the (dq) frame angular frequency. Hence, the transformation from the stationary to arbitrary dq reference frame is given by:

$$V_d + jV_q = \left(V_\alpha + jV_\beta\right).e^{-j\rho(t)} = \vec{V}_{abc}(t).e^{-j\rho(t)} \tag{5.17}$$

Where V_d and V_q are the projection of $\vec{V}_{abc}(t)$ on the dq axes. The main advantage of arbitrary reference frame is the fact that by a proper choice of frame initial phase angle and angular frequency it is possible to align the d-axis with the space phasor. Thus, the resulting space vector components on the dq-axes become DC quantities. In the next sections it is demonstrated how this particular property increases the PFC robustness.

Dynamic HESS AC Side Model

Let the LV grid voltages (Fig. 5-7) be stated as:

$$\begin{aligned} V_{ga}(t) &= \hat{V}_g.\cos[\omega_0 t + \theta_0] \\ V_{gb}(t) &= \hat{V}_g.\cos[\omega_0 t + \theta_0 - \frac{2\pi}{3}] \\ V_{gc}(t) &= \hat{V}_g.\cos[\omega_0 t + \theta_0 - \frac{4\pi}{3}] \end{aligned} \tag{5.18}$$

Which represent the stiff LV grid model introduced in Section 3.3, in which the voltage amplitude $\hat{V}_g$ and its angular frequency ω_0 are constant quantities. This means the dynamics of the grid voltage imposed at the PCC are neglected in this argument. Then, by (5.13) the grid voltage space phasor is:

$$\vec{V}_{g,abc}(t) = \left(\hat{V}_g.e^{j\theta_0}\right)e^{j\omega_0 t} = \hat{V}_g.e^{j(\omega_0 t+\theta_0)} \tag{5.19}$$

Consequently, the dynamics of HESS AC Side demonstrated in Fig. 5-7 are given by:

$$L.\frac{d\vec{i}_{abc}}{dt} = -R_L.\vec{i}_{abc} + \vec{V}_{t,abc} - \vec{V}_{g,abc} \tag{5.20}$$

Where the $\vec{V}_{t,abc}$ and $\vec{i}_{abc}$ represent the inverter terminal voltage and current space phasors respectively. By replacing $\vec{V}_{g,abc}$ in (5.20) by the expression given in (5.19):

$$L.\frac{d\vec{i}_{abc}}{dt} = -R_L.\vec{i}_{abc} + \vec{V}_{t,abc} - \hat{V}_g.e^{j(\omega_0 t+\theta_0)} \tag{5.21}$$

And by transforming $\vec{V}_{t,abc}$ and $\vec{i}_{abc}$ to dq- frame:

$$\vec{i}_{abc} = i_{t,dq}.e^{j\rho} \quad \text{and} \quad \vec{V}_{t,abc} = V_{t,dq}.e^{j\rho} \tag{5.22}$$

Consecutively by inserting (5.22) in (5.21) and multiplying both hand sides expressions by $e^{-j\rho}$ the system dynamics in dq frame is resulted as:

$$L.\frac{di_{t,dq}}{dt} = -j.(L.\frac{d\rho}{dt}).i_{t,dq} - R_L.i_{t,dq} + V_{t,dq} - \hat{V}_g.e^{j(\omega_0 t+\theta_0-\rho)} \tag{5.23}$$

Now by decomposing (5.23) into the d and q components according to (5.17):

$$\begin{aligned} L.\frac{di_{t,d}}{dt} &= (L.\frac{d\rho}{dt}).i_{t,q} - R_L.i_{t,d} + V_{t,d} - \hat{V}_g.\cos[\omega_0 t + \theta_0 - \rho)] \\ L.\frac{di_{t,q}}{dt} &= -(L.\frac{d\rho}{dt}).i_{t,d} - R_L.i_{t,q} + V_{t,q} - \hat{V}_g.\sin[\omega_0 t + \theta_0 - \rho)] \end{aligned} \tag{5.24}$$

And to present (5.24) in standard state space form, the arbitrary angular frequency $\omega(t)$ of dq frame, is introduced as the third input. This adds another state equation to the model:

$$\begin{aligned} L.\frac{di_{t,d}}{dt} &= (L.\frac{d\rho}{dt}).i_{t,q} - R_L.i_{t,d} + V_{t,d} - \hat{V}_g.\cos[\omega_0 t + \theta_0 - \rho)] \\ L.\frac{di_{t,q}}{dt} &= -(L.\frac{d\rho}{dt}).i_{t,d} - R_L.i_{t,q} + V_{t,q} - \hat{V}_g.\sin[\omega_0 t + \theta_0 - \rho)] \\ \frac{d\rho}{dt} &= \omega(t) \end{aligned} \tag{5.25}$$

Where $V_{t,d}$, $V_{t,q}$ and $\omega(t)$ are the inputs and $i_{t,d}$, $i_{t,q}$ and ρ are the state variables. The dynamic model defined by (5.25) is a coupled non-linear dynamical system due to presence of the highlighted terms. in the case that the $\rho_0 = 0$ and $\omega(t) = 0$ then dq-frame represent $\alpha\beta$ stationary frame. In which due to the sinusoidal grid voltage terms, also the system solutions $i_{t,d}$ and $i_{t,q}$ obtain AC values. This highlights the fact that the dq-frame performance tightly depends on a proper choice of ρ_0 and $\omega(t)$. By setting these values to the corresponding initial phase angel θ_0 and angular frequency ω_0 of the grid space phasor, the synchronous dq-frame is achieved. In this frame the d-axis is aligned with $\vec{V}_{g,abc}(t)$ for all time instants. Hence, the projection of $\vec{V}_{g,abc}(t)$ on dq-frame leads to a constant DC value for $V_{g,d}$ and a zero component for $V_{g,q}$, which replace the sinusoidal terms. Moreover, the third equation in (5.25) is solved as:

$$\rho(t) = \omega_0 t + \theta_0 \tag{5.26}$$

Then the linear coupled form of (5.25) is expressed by:

$$\begin{aligned} L.\frac{di_{t,d}}{dt} &= +L.\omega_0.i_{t,q} - R_L.i_{t,d} + V_{t,d} - \hat{V}_g \\ L.\frac{di_{t,q}}{dt} &= -L.\omega_0.i_{t,d} - R_L.i_{t,q} + V_{t,q} + 0 \end{aligned} \tag{5.27}$$

It is concluded that by employing the synchronous frame, the grid voltage influences the dynamical model as a DC input. The control scheme which guarantees (5.26) for all time instances is called phase locked loop (PLL).

5.2.2 Phase Locked Loop

As it is demonstrated previously, when the synchronous dq-frame is obtained the q component of the grid voltage $V_{g,q}$ is zero. This property is the basis of PLL design (Fig. 5-9). For this to be achieved, let the phase angle difference between $\vec{V}_{abc}$ and dq frame be:

$$\Delta\theta = \theta(t) - \rho(t) \tag{5.28}$$

Consequently, based on the transformation matrix presented in Appendix A.3 the $\vec{V}_{g,abc}(t)$ components on dq-frame are:

$$\begin{aligned} V_{g,d} &= \hat{V}_g.\cos[\theta(t) - \rho(t)] \\ V_{g,q} &= \hat{V}_g.\sin[\theta(t) - \rho(t)] \end{aligned} \tag{5.29}$$

The second equation in system (5.29) shows the non-linear relation of $V_{g,q}$ to the phase angle difference. Therefore, to linearize the system, it is assumed that the $\Delta\theta$ is approximately zero, then (5.29) is approximated by:

$$\begin{aligned} V_{g,d} &\approx \hat{V}_g \\ V_{g,q} &\approx \hat{V}_g.(\theta(t) - \rho(t)) \end{aligned} \tag{5.30}$$

Then let the voltage error be:

$$e(t) = V_{g,q-ref} - V_{g,q} \tag{5.31}$$

Where $V_{gq,ref}$ is set to zero for the realization of synchronous frame. Then by replacing $V_{g,q}$ with its approximation stated in (5.30), consequently the error signal is represented by:

$$e(t) = -\hat{V}_g.(\theta(t) - \rho(t)) \tag{5.32}$$

Then dividing (5.32) by approximated $V_{g,d}$ in (5.30) results in $\Delta\theta$. This phase difference is processed by a PI controller to regulate dq-frame rotation speed. As it is illustrated in Fig. 5-9 This regulating term $\Delta\omega$ is added to the grid frequency and then the result is integrated to derive the rotating frame phase angle. Finally, the grid voltage transformation to the dq-frame is introduced in the feedback path. However, by the grid model stiffness assumption the transformation can be neglected. Moreover, the feedback $\theta(t)$ term can

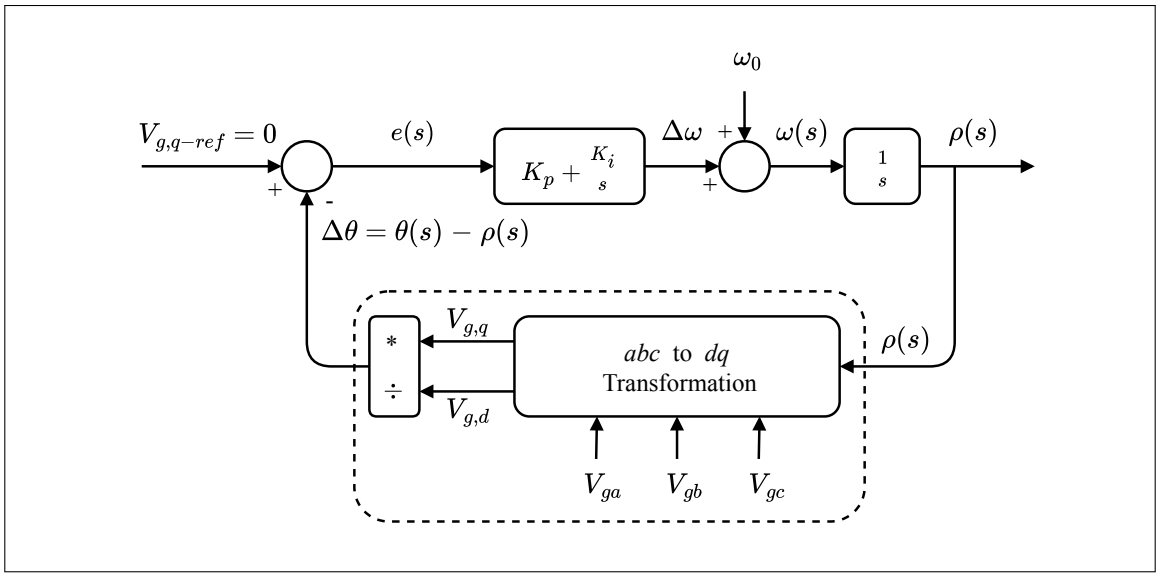

Figure 5-9: PLL schematic diagram.

replace the $V_{g,q-ref}$ which is zero, resulting the following expression for PLL closed loop transfer function in Laplace domain:

$$G_{PLL}(s) = \frac{\rho(s)}{\theta(s)} = \frac{K_p.s + K_i}{s^2 + K_p.s + K_i} \tag{5.33}$$

Alternatively, this can be written in standard second order transfer function form with a zero as [11]:

$$G_{PLL}(s) = \frac{\rho(s)}{\theta(s)} = \frac{2\zeta.\omega_n.s + \omega_n^2}{s^2 + 2\zeta.\omega_n.s + \omega_n^2} \tag{5.34}$$

Therefore, the PI parameters can be tuned in terms of settling time T_s and damping factor ζ [12]:

$$K_p = \frac{9.2}{T_s} \quad , \quad K_i = \frac{K_p}{T_i} \quad \text{where} \quad T_i = \frac{T_s.\zeta^2}{2.3} \quad \text{and} \quad \omega_n = \frac{4.6}{\zeta.T_s} \tag{5.35}$$

The PLL step response is illustrated in Fig. 5-10. The overshoot is due to the presence of a zero in (5.34). As it is proposed in [8], adding a lag compensator removes the overshoot efficiently . However, in this thesis zero steady state error matters the most, since after the start-up transient the grid frequency does not exhibit any other dynamical state. In the following it is demonstrated that by the implementation of the PLL the active and reactive power exchange between HESS shown in Fig. 5-7 and the grid can be fully controlled by *dq* current components. As suggested by [8], the active and reactive power which is injected

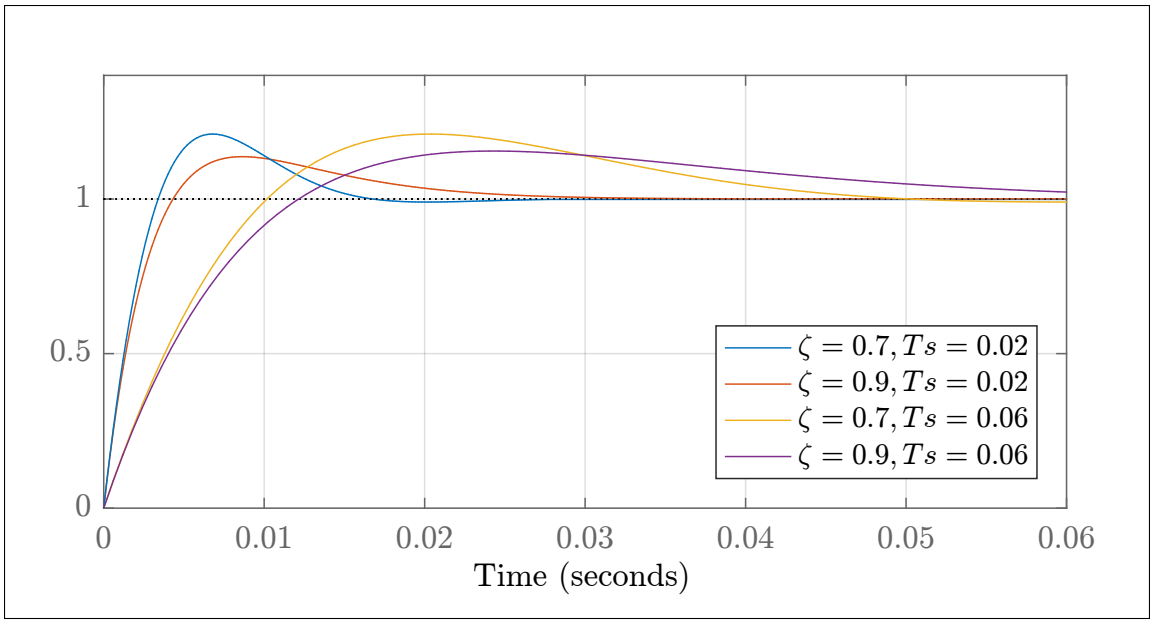

Figure 5-10: PLL step response.

or absorbed by HESS at PCC is:

$$\begin{aligned} P &= \frac{3}{2}.\Big(V_{g,d}.i_{t,d} + V_{g,q}.i_{t,q}\Big) \\ Q &= \frac{3}{2}.\Big(-V_{g,d}.i_{t,q} + V_{g,q}.i_{t,d}\Big) \end{aligned} \tag{5.36}$$

And when the synchronous frame is achieved $V_{g,q} = 0$, then (5.36) is represented by:

$$\begin{aligned} P &= \frac{3}{2}.V_{g,d}.i_{t,d} \\ Q &= -\frac{3}{2}.V_{g,d}.i_{t,q} \end{aligned} \tag{5.37}$$

Thus P and Q are controlled by $i_{t,d}$ and $i_{t,q}$ respectively. Moreover, the current reference signals might be expressed in terms of require power references P_{ref} and Q_{ref} at the PCC:

$$\begin{aligned} i_{d-ref} &= \frac{2}{3.V_{g,d}}.P_{ref} \\ i_{q-ref} &= -\frac{2}{3.V_{g,d}}.Q_{ref} \end{aligned} \tag{5.38}$$

Later on the argument regarding derivation of a decoupled form of (5.27) is presented, and consequently the inverter current controller design is introduced which enables the HESS to track current references (5.38).

Decoupled Dynamic Model

In order to derive the general (not just for the synchronous frame implementation) decoupled form of the dynamic model, by recalling (5.27) and replacing the grid voltage disturbances $\hat{V}_g$ and zero by $V_{g,d}$ and $V_{g,q}$:

$$\begin{aligned} L.\frac{di_{t,d}}{dt} &= +L.\omega_0.i_{t,q} - R_L.i_{t,d} + V_{t,d} - V_{g,d} \\ L.\frac{di_{t,q}}{dt} &= -L.\omega_0.i_{t,d} - R_L.i_{t,q} + V_{t,q} - V_{g,q} \end{aligned} \tag{5.39}$$

Where similar to (3.35) the inverter terminal voltage in dq frame is expressed by:

$$\begin{aligned} V_{t,d}(t) &= m_d.\frac{V_{DC}}{2} \\ V_{t,q}(t) &= m_q.\frac{V_{DC}}{2} \end{aligned} \tag{5.40}$$

In which m_d and m_q are defined in terms of new control inputs v_d and v_q as:

$$\begin{aligned} m_d &= \frac{2}{V_{DC}}.\Big(v_d - L.\omega_0.i_{t,q} + V_{g,d}\Big) \\ m_q &= \frac{2}{V_{DC}}.\Big(v_q + L.\omega_0.i_{t,d} + V_{g,q}\Big) \end{aligned} \tag{5.41}$$

Then by inserting (5.41) in (5.40) and the resulting dq terminal voltages in (5.39), the highlighted terms removes the coupling and disturbance terms in (5.39). And the decoupled forms is resulted in:

$$\begin{aligned} L.\frac{di_{t,d}}{dt} &= -R_L.i_{t,d} + v_d \\ L.\frac{di_{t,q}}{dt} &= -R_L.i_{t,d} + v_q \end{aligned} \tag{5.42}$$

Which defines the HESS AC side dynamics with a system of first order linear ordinary ordinary differential equations. In which $i_{t,d}$ and $i_{t,q}$ are controlled with regulating terms v_d and v_q. The dynamic model (5.42) can be alternatively stated in the Laplace domain by following identical transfer functions:

$$\begin{aligned} G_{i_{t,d}v_d} &= \frac{i_{t,d}}{v_d} = \frac{1}{R_L + L.s} \\ G_{i_{t,q}v_q} &= \frac{i_{t,q}}{v_q} = \frac{1}{R_L + L.s} \end{aligned} \tag{5.43}$$

The overall HESS PFC schematic diagram is presented in Fig. 5-11.

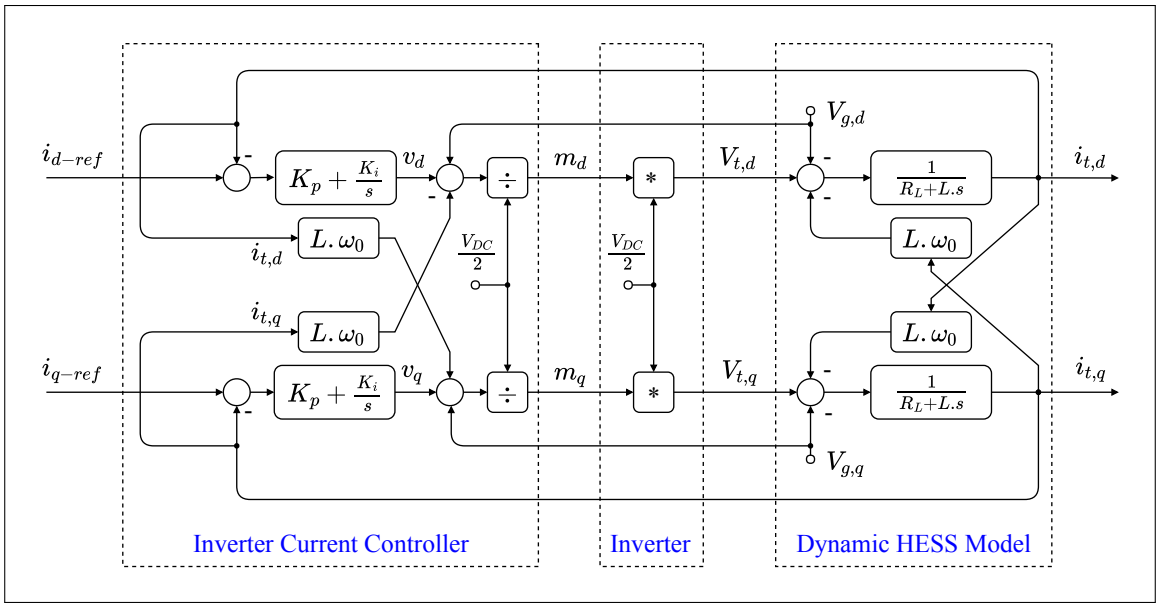

Figure 5-11: PFC schematic diagram.

5.2.3 Inverter Current Controller

In this section the PI implementation of the ICC design is discussed. The objective is to control the HESS AC side dynamics expressed by (5.42). As it was previously mentioned, the dynamic model transfer function is (5.43). This transfer function which has a first order nature is almost identical to the BESS CDC plant (5.4). Thus, for ICC the zero-pole cancellation approach is also practical. The schematic diagram of the ICC is depicted in Fig. 5-12 which is a simplified version of Fig. 5-11. The controllers parameters in Fig. 5-12 can be adjusted to meet the required ICC bandwidth. It must be taken into account that also in this case, similar to CDC the closed loop bandwidth should be at least 10 times smaller than the inverter switching frequency. For the sake of compactness the tuning procedure and bode plots are not presented here. However, they are of the same nature as the results presented in Section 5.1.2.

Modulating Signals Generation

Once the regulating inputs v_d and v_q are generated by ICC, the inverter modulating signals m_d and m_q are constructed (Fig. 5-11). Moreover, when a three-phase three-level NPC inverter is adopted, m_d and m_q must be transformed into *abc* frame which are defined by (3.36). Once m_a, m_b and m_c are obtained, the corresponding switching functions are

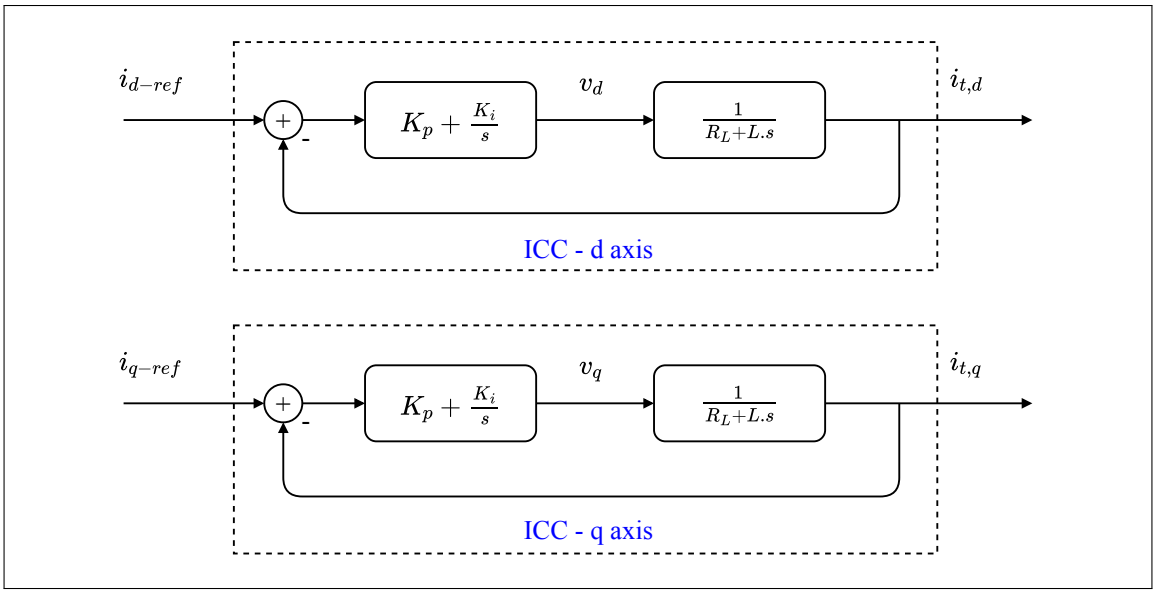

Figure 5-12: ICC schematic diagram.

generated by the PWM scheme illustrated in Fig. 3-13. This three-phase modulating signal generator augmented by PWM scheme is visualized in Fig. 5-13.

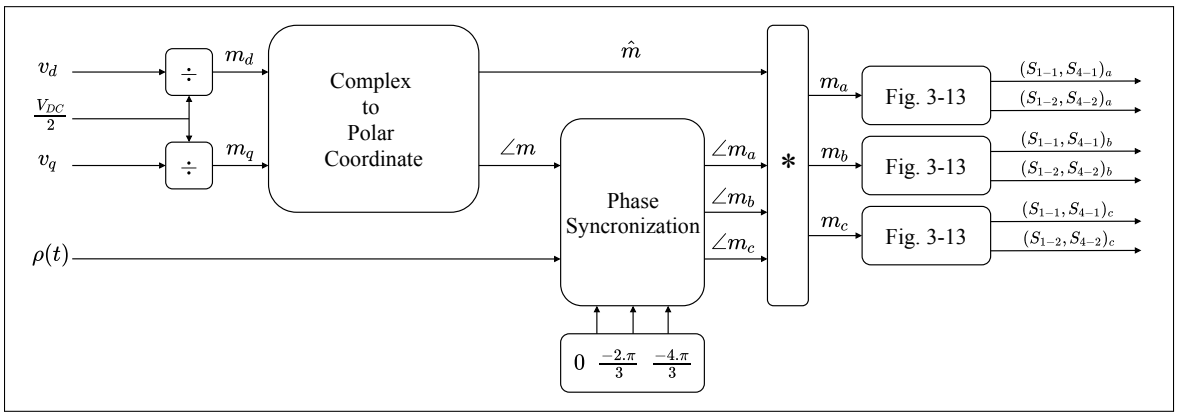

Figure 5-13: ICC schematic diagram.

5.2.4 DC Link Voltage Controller

HESS DC link topology was previously introduced in Section 3.1.5. In this section following the argument on PFC, the DC link model and its corresponding control plant is introduced. Moreover, the DCVC design method is presented. The objective of DCVC implementation is to stabilize the DC link voltage. The DC link circuit diagram and the important currents on the HESS DC side is shown in Fig. 5-14. It must be taken into account that when NPC

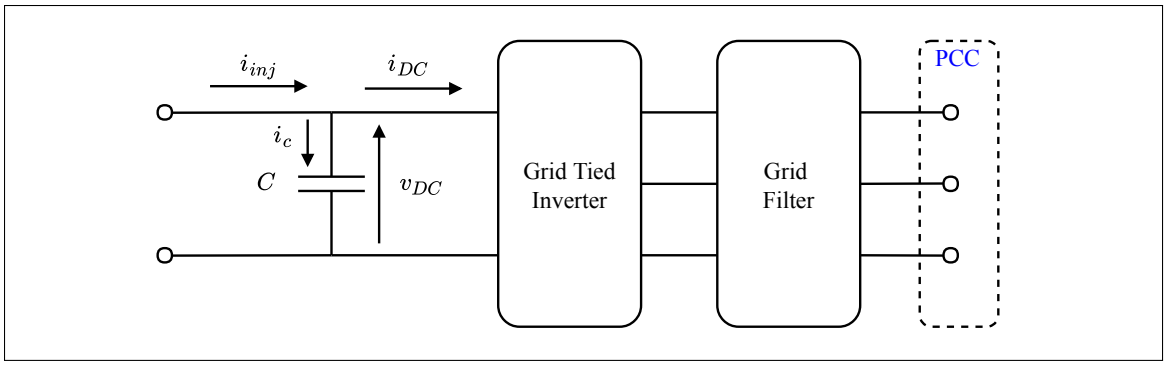

Figure 5-14: HESS DC link circuit diagram.

inverter is used,the DC link itself is composed of two identical capacitor ($\frac{1}{2C}$) connected in series which is equivalent to the DC link shown in Fig. 5-14. The instantaneous power balance equation at the DC link's positive terminal can be written as:

$$P_{inj} = P_c + P_{DC} \tag{5.44}$$

Which alternatively can be stated in terms of the DC link voltage as:

$$v_{DC}.i_{inj} = v_{DC}.i_{DC} + C.v_{DC}.\frac{dv_{DC}}{dt} \tag{5.45}$$

In which the left hand side term is the active power injected by PV and BESS. And the second term on the right hand side stands for the active power delivered to the inverter. Under no-loss condition $v_{DC}.i_{DC}$ is equal to the power injected to PCC by HESS:

$$v_{DC}.i_{DC} = \frac{3}{2}.v_{g,d}.i_{t,d} \tag{5.46}$$

Where $v_{g,d}$ is the grid voltage on the d-axis. Now by inserting (5.46) in (5.45):

$$v_{DC}.i_{inj} = \frac{3}{2}.v_{g,d}.i_{t,d} + C.v_{DC}.\frac{dv_{DC}}{dt} \tag{5.47}$$

This constitutes a non-linear model expressing the DC link voltage dynamics. In order to linearize the system all the variables are perturbed around their steady state values:

$$\begin{aligned}(V_{DC} + \hat{v}_{DC}).(I_{inj} + \hat{i}_{inj}) = \frac{3}{2}.(V_{g,d} + \hat{v}_{g,d}).(I_{t,d} + \hat{i}_{t,d}) + \\ C.(V_{DC} + \hat{v}_{DC}).\frac{d(V_{DC} + \hat{v}_{DC})}{dt}\end{aligned} \tag{5.48}$$

The DC voltage regulation is desired to be done by the d-axis current on the HESS AC side, in other words DCVC sets the reference current for the d-axis controller in Fig. 5-12. And voltage regulation is achieved when ICC perfectly tracks its reference. Therefore, the DCVC plant in the Laplace domain is described by $\frac{\hat{v}_{DC}(s)}{\hat{i}_{t,d}(s)}$. Thus, all the other perturbation terms in (5.48) are set to zero. Moreover, the derivative of the steady state values and second order perturbation terms are neglected. Hence, the simplified version of (5.48) is obtained as:

$$\hat{v}_{DC}.I_{inj} = \frac{3}{2}.V_{g,d}.\hat{i}_{t,d} + C.V_{DC}.\frac{d\hat{v}_{DC}}{dt} \tag{5.49}$$

The steady state equivalent resistance can be defined as:

$$R_{eq} = \frac{V_{DC}}{I_{inj}} \tag{5.50}$$

Additionally, by the argument on DC link reference voltage level V_{DC-ref} selection presented in Appendix A.1, V_{DC} can be approximated by:

$$V_{DC} \simeq \sqrt{3}.V_{g,d} \tag{5.51}$$

Now by dividing both hand sides of (5.49) by V_{DC} and then by considering (5.50) and (5.51), the DC voltage to d axis current transfer function is resulted as:

$$G(s) = \frac{\hat{v}_{DC}(s)}{\hat{i}_{t,d}(s)} = \frac{\sqrt{3}}{2}.\frac{R_{eq}}{1 - R_{eq}.C.s} \tag{5.52}$$

Moreover, the influence of the injected current $\hat{i}_{inj}$ and grid voltage $\hat{v}_{g,d}$ disturbances on the DC link voltage can be examined with similar approach [13]. Therefore the disturbance transfer functions are expressed by:

$$\begin{aligned} G_{d1}(s) &= \frac{\hat{v}_{DC}(s)}{\hat{i}_{inj}} = \frac{-R_{eq}}{1 - R_{eq}.C.s} \\ G_{d2}(s) &= \frac{\hat{v}_{DC}(s)}{\hat{v}_{g,d}} = \frac{\sqrt{3}}{1 - R_{eq}.C.s} \end{aligned} \tag{5.53}$$

The overall DCVC scheme including the d-axis ICC as the inner loop is illustrated in Fig. 5-15. As it is stated by (5.52) dynamics of DC link voltage is influenced by the DC side steady state equivalent resistance R_{eq} defined by (5.52). Thus, before proceeding to

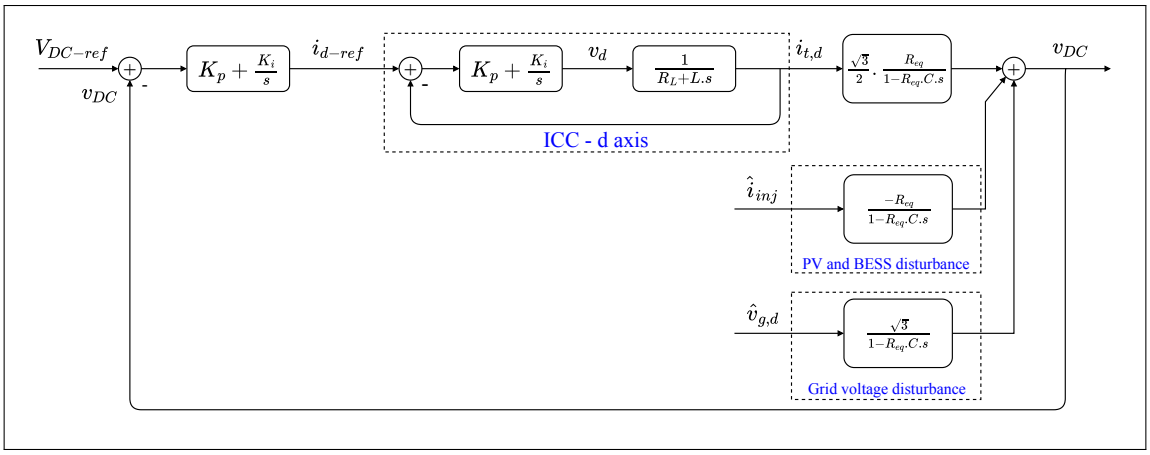

Figure 5-15: DC voltage controller scheme.

controller tuning, this value must be identified. By definition, R_{eq} can gain positive or negative sign which depends on HESS operation modes. In other word, if the DC power sources (PV and BESS) are injecting a constant power $P_{inj} > 0$ to the AC side, HESS is operating in inverting mode. Similarly, if the BESS absorbs the power $P_{inj} < 0$ from the Grid, HESS operates in rectifying mode. Consequently, R_{eq} can be approximated by the slope of the line which is the tangent to the constant power characteristic curve around the operating point (Fig. 5-16). The Constant power characteristic is defined by:

$$\begin{aligned} P_{inj} = v_{DC}.i_{inj} = k \quad , \quad k > 0 \quad \text{(inverter mode)} \\ P_{inj} = v_{DC}.i_{inj} = k \quad , \quad k < 0 \quad \text{(rectifier mode)} \end{aligned} \tag{5.54}$$

Therefore, as it is demonstrated in Fig. 5-16 inverting and rectifying modes lead to negative and positive sign for R_{eq} respectively. Now by considering (5.52), its pole is located at $s = \frac{1}{R_{eq}.C}$. Hence, this system might be unstable for rectifying mode where $R_{eq} > 0$ moves the system pole to the right half half of the Laplace plane. However, the high value of C which is typical in HESS applications, drags the pole near the origin. The controller tuning must be performed assuming the worst case scenario (rectifying mode). Since the transfer function expressed by (5.52) is a first order system, it can be tuned with the zero-pole cancellation method presented in Section 5.1.2. It must be taken into account that the DCVC bandwidth must be at least 10 times smaller than that of ICC. Thus, the ICC closed loop transfer function in Fig. 5-15 can be approximated by unity.

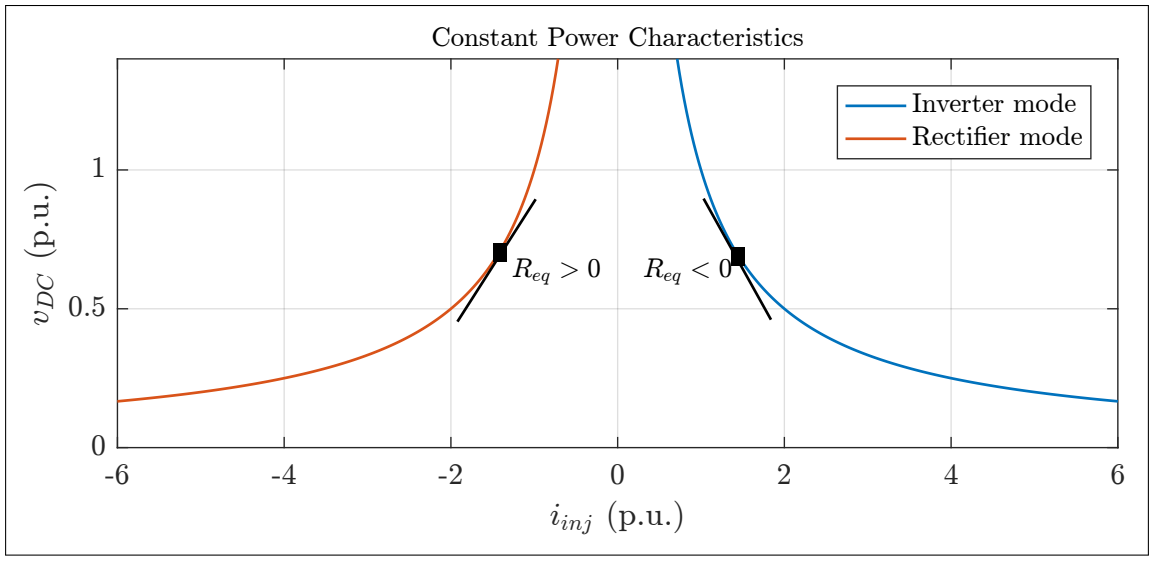

Figure 5-16: DC side equivalent resistance approximation.

5.3 Auxiliary Functionality Design

In this section the auxiliary functionality implementation are discussed. This functionalities includes DC link pre-charge controller (DCC), GPIA and GFVR combined scheme and battery reference current generator (BRCG).

5.3.1 DC Link Pre-Charge Controller

Prior to initiating any power exchange between HESS DC and AC sides, it is compulsory to charge the DC link capacitor to its reference voltage level. Once the DC link is charged, the DCC controller is disabled, and DCVC (Section 5.2.4) maintains the DC link voltage. DC link pre-charge can be done by PV, grid or BESS. In this thesis BESS is chosen to be the power source employed for charging the DC link. Trivially, if BESS is fully discharged, PV or grid can serve as the auxiliary power sources. However, the BESS discharge level can be adjusted by the CDM (Section 4.1.2) in a way that the BESS always keeps enough energy to fully charge the DC link capacitors. In the DCC scheme outlined by Fig. 5-17 the DC link voltage error is processed by a PI controller. Therefore, the controller regulates the BBBC inductor current, and consequently this current is fed as reference current for the BESS charge-discharge scheme. The PI controller can be tuned with zero-pole cancellation method in order to achieve the required bandwidth for the outer voltage control loop. It must be taken into account that the inner loop must be 10 times faster than the outer

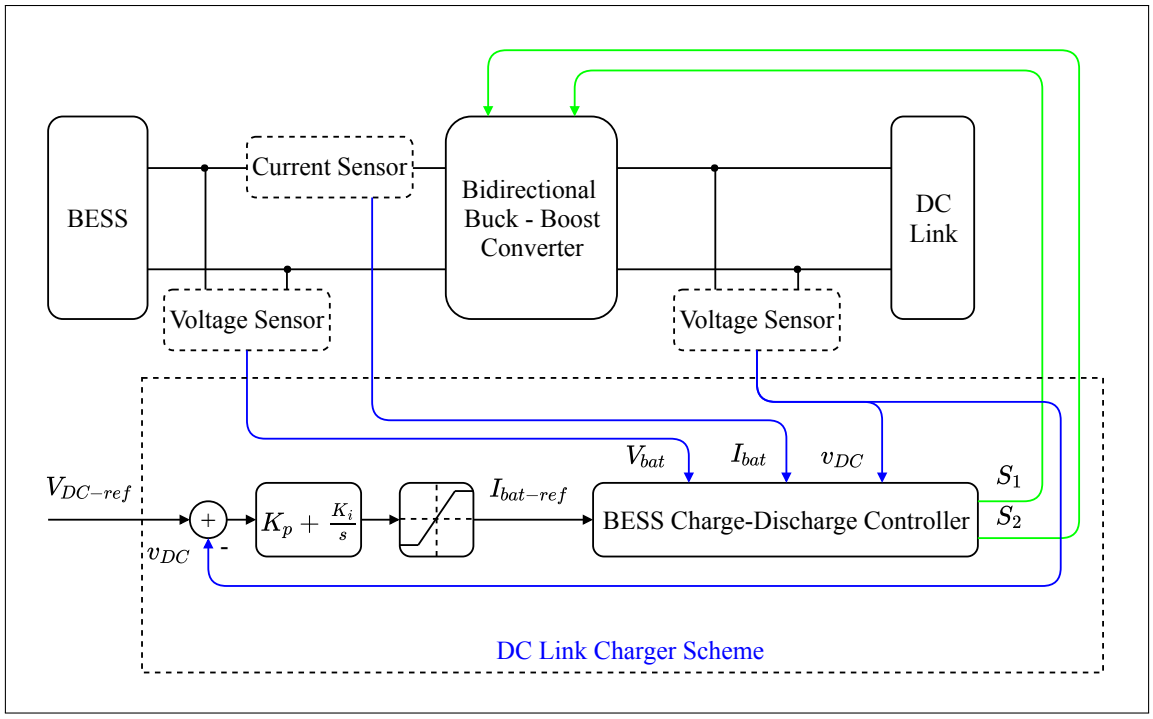

Figure 5-17: DC link pre-charge control scheme.

one. Moreover, a saturation block be employed in order to limit the BESS reference current to its rated discharge current. Therefore, before the DC link voltage reaches some certain neighborhood of its reference value, the reference current is limited to the rated value, which results in the BESS constant current discharge mode. And once the voltage is close to the reference level, the BESS current decays to zero as the voltage increases. A generic result of the DCC performance when it charges the DC link from $0.9V_{DC-ref}$ to V_{DC-ref} is depicted in Fig. 5-18.

5.3.2 GPIA and GFVR controller

In this section the implementation of GPIA and GFVR controller is presented. For technical reasons firstly the GFVR controller is introduced and consequently it is augmented by the GPIA controller.

As it was introduced in Chapter 4, the GFVR scheme enables the HESS to provide grid support terms of frequency and voltage stabilization. The operational principle of the GFVR is based on sensing frequency and voltage deviation, and correspondingly injecting to or absorbing power from (P_{droop} and Q_{droop} shown in Fig. 4-7) the LV grid. Thus, the knowledge of grid frequency and voltage operational limits is necessary. This is usually

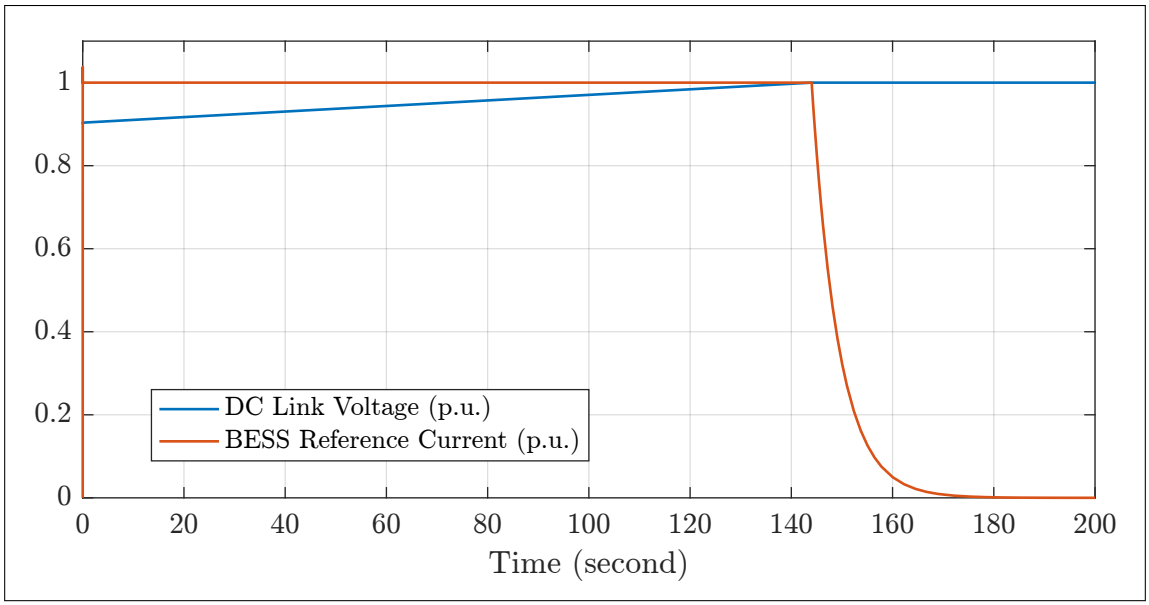

Figure 5-18: DC link pre-charge control performance.

given by grid side standards.

P-F Regulation

In this thesis, two different limits are considered for the frequency. As the nominal frequency is 50 Hz, 0.2 Hz deviation is considered as the frequency soft limit i.e. within this range ($49.8 < f < 50.2$) no regulation is required. And the frequency hard limit is set to 0.4 Hz, thus in the are between soft and hard limits ($49.6 < f < 49.8$ and $50.2 < f < 50.4$) HESS regulates P_{droop}. And beyond the hard limit ($f < 49.6$ or $50.4 < f$) is considered as faulty grid state and HESS must be disconnected from the grid. The amount of regulating active power P_{droop} is identified by the P-F droop curves demonstrated in Fig. 5-19. As a result, when the frequency is bellow the nominal value, HESS injects active power into the grid ($P_{droop} > 0$). Similarly, in over frequency state HESS absorbs power from the grid ($P_{droop} < 0$).

Q-V Regulation

Similar to frequency regulation, for the grid voltage regulation, reactive power is adjusted according to the Q-V curve depicted in Fig. 5-20. In this case there is just one operational limit for grid voltage deviation which is 5 percent of the base value. Thus, within the interval of $0.95V_{base} < V_{grid} < V_{base}$ the HESS injects reactive power to the grid ($Q_{droop} > 0$). And

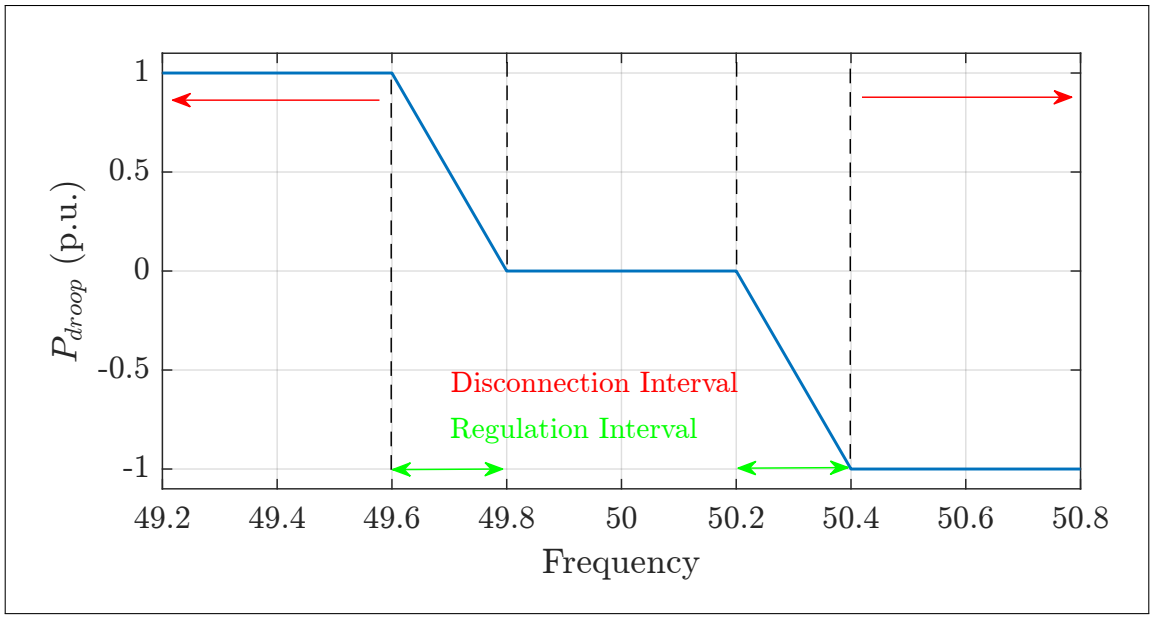

Figure 5-19: P-F droop characteristic.

similarly in the case of over-voltage $V_{base} < V_{grid} < 1.05V_{base}$ HESS absorbs reactive power from the grid ($Q_{droop} < 0$). And beyond these limits the HESS must be disconnected from the grid.

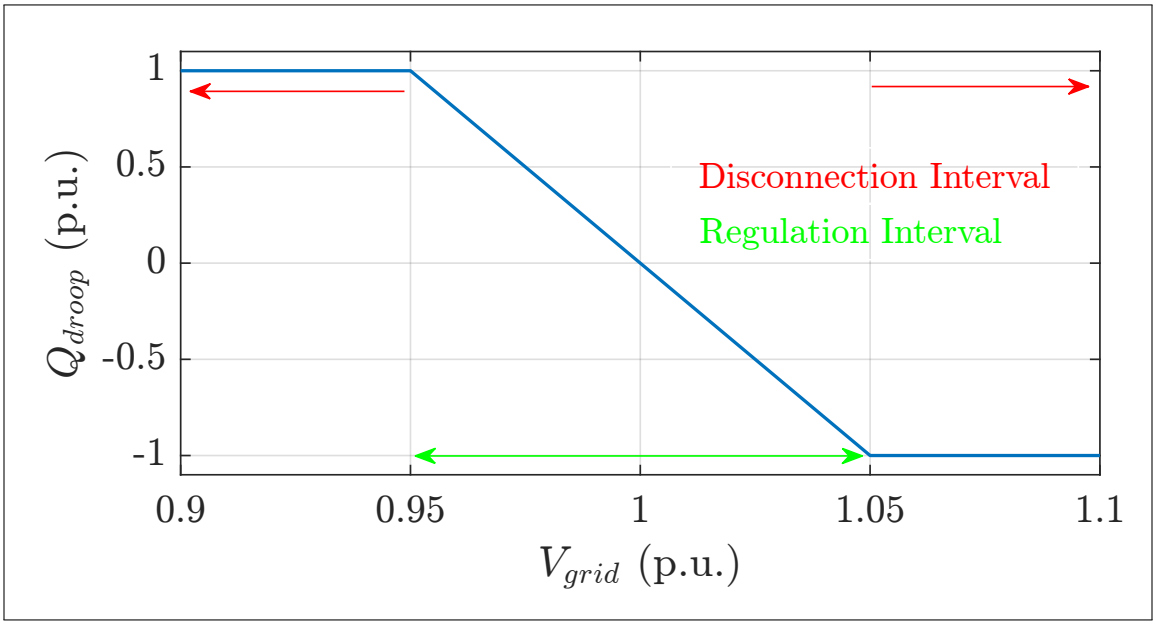

Figure 5-20: Q-V droop characteristic.

GPIA and GFVR controller implementation

In order to design this controller firstly the reference values for all the power exchanges shown in Fig. 4-7 are evaluated. The GPIA references are directly set by the HESS according to the scenarios presented in Section 4.2.1. And the GFVR reference are evaluated by the droop controllers introduced in previous discussion. And in order to evaluate the instantaneous power (sum of the GPIA and GFVR) which is injected to the grid, the voltage, current and frequency are measured at MP2 (after PCC) depicted in Fig. 4-7. Then based on (5.36) the instantaneous power is calculated. Consequently this power is compared to the sum of GFVR and GPIA reference values. Hence, the power error signal is constructed.

It must be noted that the two identical independent controllers are designed for active and reactive power. Once the error signal is obtained, it will be processed by a PI controller. This scheme is illustrated in Fig. 5-21. It is noteworthy that the household load active and reactive power (P_{Load} and Q_{Load}) estimations can be obtained by calculating the power difference between measurement points MP1 and MP2 which are highlighted in Fig. 4-7. As it is shown Fig. 5-21 the output of the reactive power controller I_{q-ref} sets the inverter q-axis reference current for the scheme presented in Fig. 5-12. Thus the reactive power is controlled directly from the inverter control.

Similarly, the active power controller output $I_{d-ref,reg}$ might set the inverter d-axis current reference. However, this reference current is already set by the DCVC shown in Fig. 5-15. Moreover, the amount of active power corresponding to $I_{d-ref,reg}$ must be generated from the DC side so the inverter can pass it through the AC side. Therefore, this reference current is fed to battery BRCG scheme (Section 5.3.3) which regulates the BESS reference current in a way that the overall DC power is equal to the required active power by GPIA and GFVR schemes. This reference is tracked by the CDC scheme illustrated in Fig. 5-6. The active power PI controller bandwidth must be coordinated with respect to the CDC bandwidth. And likewise the reactive power PI controller bandwidth must be coordinated with the ICC bandwidth. Therefore under no-loss assumption for all the HESS components, the inverter active and reactive power highlighted in Fig. 2-1 and expressed by (5.36) are

equal to:

$$\begin{aligned} P_{inv} &= P_{PV} + P_{BESS} = P_{Load} + P_{grid} + P_{droop} \\ Q_{inv} &= Q_{Load} + Q_{grid} + Q_{droop} \end{aligned} \tag{5.55}$$

This result sets the ground rule to define the HESS operational states which is presented in Chapter 6.

5.3.3 Battery Reference Current Generator

To sum up this chapter, in this section the scheme which adjusts the BESS reference current is presented. For this to be done, the reference current must be identified by considering the CDM scheme outputs discussed in Section 4.1.2. Moreover, the BESS reference current must be adjusted so that the active power balance expressed by (5.55) is respected. Thus, the battery state of operation (charge-discharge) is distinguished by the D_{en} and C_{en} signals generated by CDM scheme. Additionally, the reference current value is evaluated so that the P_{BESS} fills the gap between P_{PV} and P_{Load}. Moreover it also includes the term $I_{d-ref,reg}$ generated by GPIA and GFVR schemes. The BRCG logic is constructed by following conditional statements:

- if $D_{en} = 1$ && $\left(\frac{P_{Load}-P_{PV}}{V_{bat}} + I_{d-ref,reg}\right) > 0 \implies I_{bat-ref} = \frac{P_{Load}-P_{PV}}{V_{bat}} + I_{d-ref,reg}$
- if $C_{en} = 1$ && $\left(\frac{P_{Load}-P_{PV}}{V_{bat}} + I_{d-ref,reg}\right) < 0 \implies I_{bat-ref} = \frac{P_{Load}-P_{PV}}{V_{bat}} + I_{d-ref,reg}$
- else $\implies I_{bat-ref} = 0$

As a result, if the BESS reference current sign specifies an operation mode which is not allowed by the CDM, the BRCG output will be zero, resulting in soft BESS isolation from the rest of the HESS. In this case, the PV power is transfered to the AC side, and any active power shortage or surplus is absorbed from or injected to the grid. Therefore from the flexibility point of view it is crucial to keep BESS SoC level always withing its operational limits. The BRCG scheme is illustrated in Fig. 5-21.

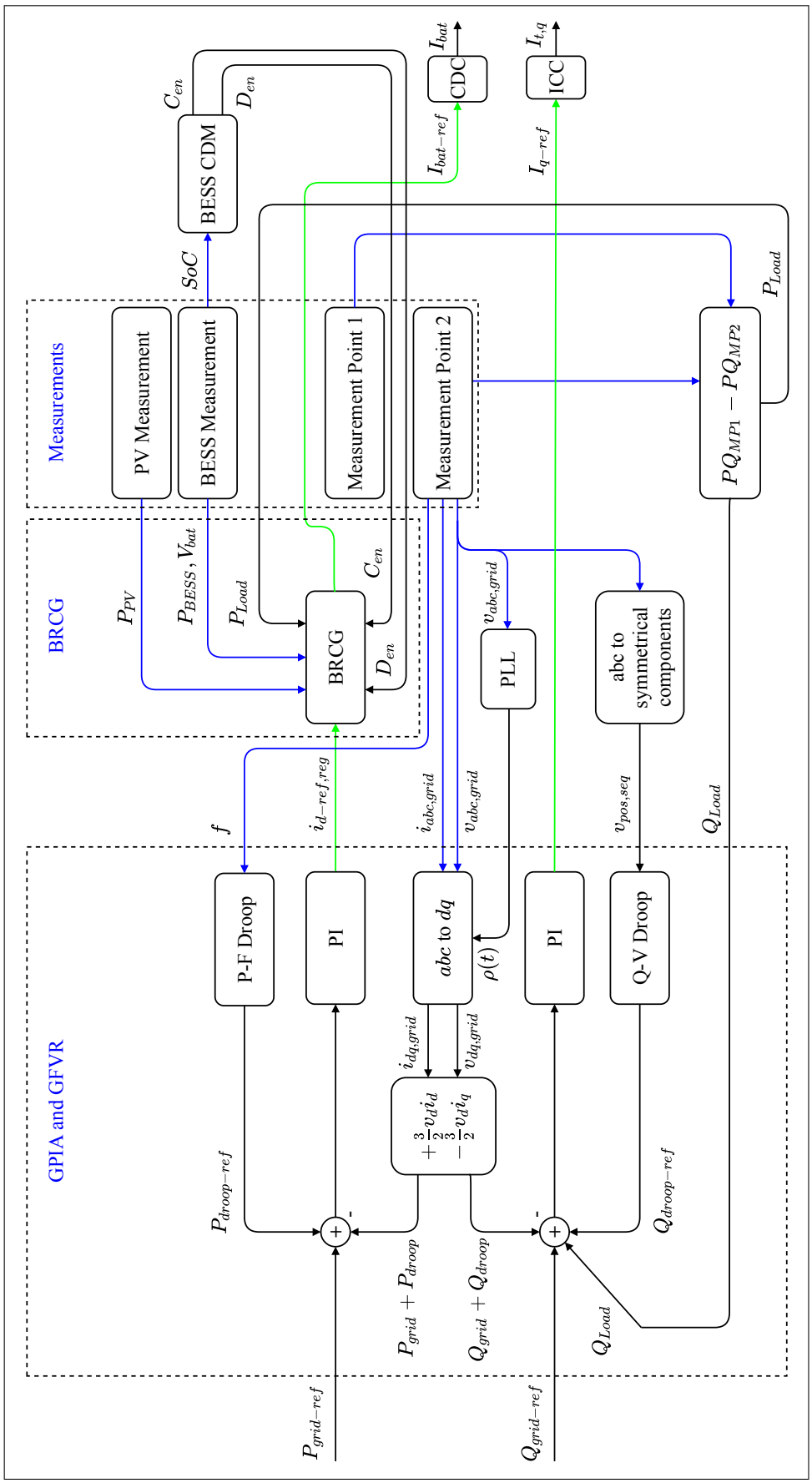

Figure 5-21: GPIA and GVFR implementation cascaded with BRCG, ICC and CDC.

Chapter 6

HESS Operational States

In this chapter the HESS operational states are described. The HESS control ensures that ideally at every instant of time the household load demand is responded. For the HESS, the priority is to supply the load with available PV and BESS power. That means the household HESS owner possibly prefers not to buy any power from the grid. And on the contrary, possibly sell power to the grid under GPIA or GFVR schemes. However, this can only be done with the permission of the grid operator. This information is provided to HESS with two signals from the grid power management unit. One specifies if the HESS system is allowed to inject power I_{en} and the other one specifies the possibility of absorbing power from the grid A_{en}. GPMU also sends an auxiliary signal which specifies grid emergency states E_{en}. The enable signals are considered to be active high. In case E_{en} is active, this implies the load supply is no longer a priority for the HESS and it must respond to the grid injection-absorption requirements via GPIA and GFVR schemes. In this case all the available DC power and free BESS storage capacity can be used to provide assistance to the grid.

Initially, it is necessary to identify the possible HESS scenarios, and consequently, highlight all the possible states which correspond to each scenario. In this thesis, for the sake of compactness the HESS states are just described by considering active power flows through the HESS. This can be easily extended to include the states occurred by reactive power flows through the HESS AC side. Now by having P_{PV} and P_{Load} measurements alongside the C_{en} (BESS charge enable), D_{en} (BESS discharge enable) and the GPMU signals I_{en}, A_{en} and E_{en} the HESS possible operational scenarios are described as:

$$(0) \quad v_{DC} < v_{DC-ref} \implies \begin{cases} \text{(0-1) if } D_{en} = 1 \implies \text{BESS pre-charging DC link} \\ \text{(0-2) if } P_{PV} > 0 \implies \text{PV pre-charging DC link} \\ \text{(0-3) if } A_{en} = 1 \implies \text{Grid pre-charging DC link} \\ \text{(0-4) else} \implies \text{Halt (waiting for availabe power source)} \end{cases}$$

Scenario (0) specifies the DC link pre-charging operation. The HESS remains in this state as long as it takes to charge the DC link.

$$(1) \quad P_{PV} > P_{Load} \implies \begin{cases} \text{(1-1) if } C_{en} = 1 \implies \text{BESS charging} \\ \text{(1-2) if } I_{en} = 1 \implies \text{HESS injects to grid} \\ \text{(1-3) else} \implies \text{PV turned off \& BESS discharging} \end{cases}$$

In the scenario (1), the excess PV power is either fed into the BESS or to the grid. If these states are not allowed, PV is turned off and the BESS supplies the load.

$$(2) \quad P_{PV} = P_{Load} \implies \begin{cases} \text{(2-1) if } D_{en} = 1 \ \& \ I_{en} = 1 \implies \text{BESS injects to the grid} \\ \text{(2-2) else} \implies \text{BESS turned off} \end{cases}$$

In the scenario (2), the PV is enough to supply the load, thus if it is allowed the BESS can inject to the grid.

$$(3) \quad P_{PV} < P_{Load} \implies \begin{cases} \text{(3-1) if } D_{en} = 1 \implies \text{BESS discharging} \\ \text{(3-2) if } A_{en} = 1 \implies \text{HESS absorbs from the grid} \\ \text{(3-3) else} \implies \text{Load demand is partially responded} \end{cases}$$

In the scenario (3), in the state (3-3) there is no way to satisfy the load demand.

$$(4) \quad P_{PV} > 0 \ \& \ P_{Load} = 0 \implies \begin{cases} \text{(4-1) if } C_{en} = 1 \implies \text{BESS charging} \\ \text{(4-2) if } I_{en} = 1 \implies \text{HESS injects to the grid} \\ \text{(4-3) else} \implies \text{PV turned off} \end{cases}$$

In the scenario (4), in the state (4-3) the PV is turned off, because there is no way to use this power.

$$(5) \quad E_{en} = 1 \implies \begin{cases} \text{(5-1) if } I_{en} = 1 \text{ or } A_{en} = 1 \implies \text{HESS injects to (absorbs) the grid} \\ \text{(5-2) else} \implies \text{Halt} \end{cases}$$

In the scenario (5), which corresponds to the grid emergency state, all available PV and BESS power is injected to grid or all the BESS free capacity is used to absorb power from the grid.

The functional level operational state diagram of the HESS is depicted in Fig. 6-1. In this diagram, the transition occurs if the condition over the arrows is met. Moreover, the triggering condition for each scenario and its corresponding states are highlighted with the same colour. And each state is labelled according to the previously mentioned state description. In this diagram CS is the current state, R identifies the state in which DC link is charged and the HESS is ready for operation and H is the halting state in which HESS does not perform any operation and waits for a change in the input variables.

Figure 6-1: HESS operational state diagram.

Chapter 7

Simulation and Laboratory Verification

In this chapter, initially the simulation environment and model settings are discussed. Consequently, the laboratory equipments and test setup are introduced. Furthermore, for the defined test cases both the simulation and laboratory results are presented.

7.1 Simulation Environment and Model Settings

The simulation of HESS is performed in MATLAB/Simulink. If applicable, for the system components the corresponding simulink blocks are used. And for the algorithms such as MPPT and IC the corresponding Matlab code is embedded in the simulink model.

For the system configuration, the components rating and parameter are adopted based on Appendix B.1. Additionally, the controllers parameter are calculated based on the principles discussed in Chapter 5. And the resulting controllers setting are reported in table B.1. Due to multi-functionality of the HESS, the system control design includes multiple loops. Thus, a proper bandwidth coordination of the nested loops is crucial to ensure satisfactory system performance.

7.1.1 Controllers Bandwidth Coordination

For this, it is assumed that the system measurement blocks such as current and voltage sensors are ideal, so no measurement delay is introduced to the system. And as the rule of

thumb for nested loop bandwidth coordination it is considered that the inner loop is 5-10 times faster than the outer loop. It must be noted that for the algorithms (i.e. P&O and IC), logic schemes (i.e. BRCG and CDM) and GMPU signals their sampling frequencies are adjusted with respect to the controller bandwidths and HESS switching frequencies. The list of controllers, switching devices, logic and arithmetic schemes to be coordinated together is presented bellow:

- Inverter switching frequency f_{sw-inv}
- ICC bandwidth bw_{ICC}
- DCVC bandwidth bw_{DCVC}
- PV DC - DC boost switching frequency $f_{sw-boost}$
- BBBC switching frequency $f_{sw-BBBC}$
- CDC bandwidth bw_{CDC}
- MPPT sampling frequency f_{s-MPPT}
- DCC bandwidth bw_{DCC}
- BRCG sampling frequency f_{s-BRCG}
- GFVR and GPIA bandwidth $bw_{GFVR\&GPIA}$
- GPMU sampling frequency f_{s-GPMU}

The HESS bandwidths coordination is illustrated in Fig. 7-1.

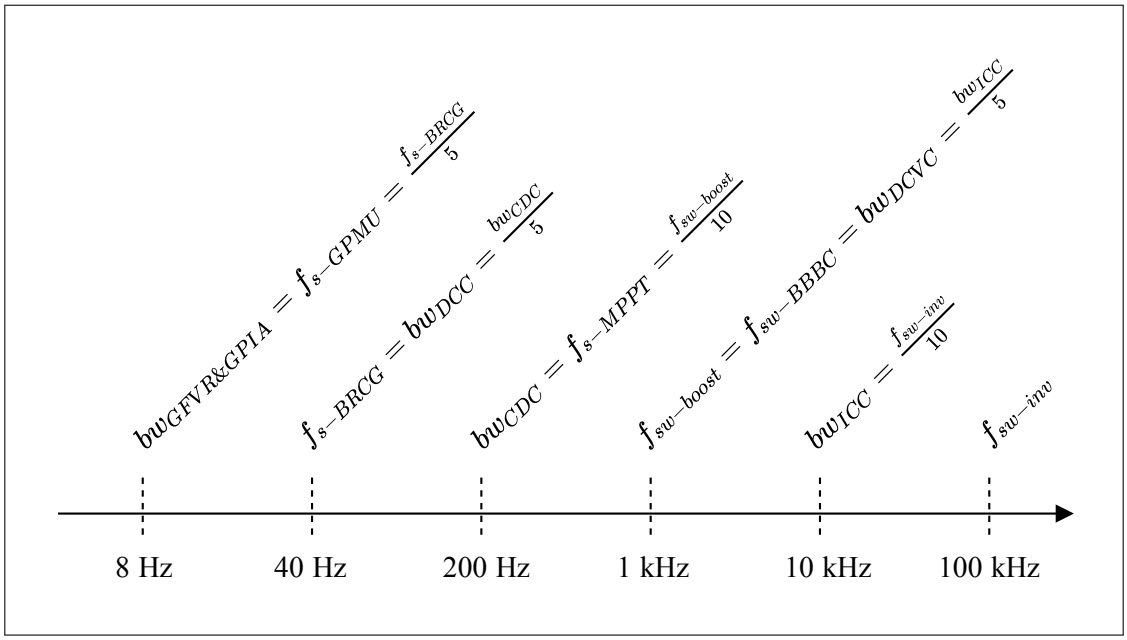

Figure 7-1: HESS bandwidths coordination.

7.2 Simulation Results

In this section simulation results for some generic test cases are presented.

7.2.1 HESS Response With Dynamic Unbalanced Load Demand

For this simulation case the household load profile varies dynamically. The HESS and load active and reactive power values are normalized with the inverter maximum power presented in table B.1. This load profile consists of following components:

- There-phase balanced sinusoidal active power (offset=0.25 p.u. , amplitude=0.20 p.u.)
- Three-phase step change in active power (step amplitude=0.20 p.u. at t=0.5 - 2 sec)
- Unbalanced constant power active power for phase A (amplitude=0.30 p.u.)
- There-phase balanced sinusoidal reactive power (offset=0.0.3 p.u. , amplitude=0.15 p.u.)

The P_{Load} and Q_{Load} for individual phases and in total are depicted in Fig. 7-2 and Fig. 7-3 respectively.Before presenting the HESS model response, following points must be considered:

- PV operates under STC, so it provides constant power.
- The GFVR scheme is disabled, and GPIA scheme is active so in steady state it forces the grid power exchange to zero.
- DC link refernce voltage is set to $V_{DC-ref} = 1000$ V.
- Simulation time is 3 seconds.

In the following the corresponding simulation plots (for t=0 - 3 sec.) are presented.

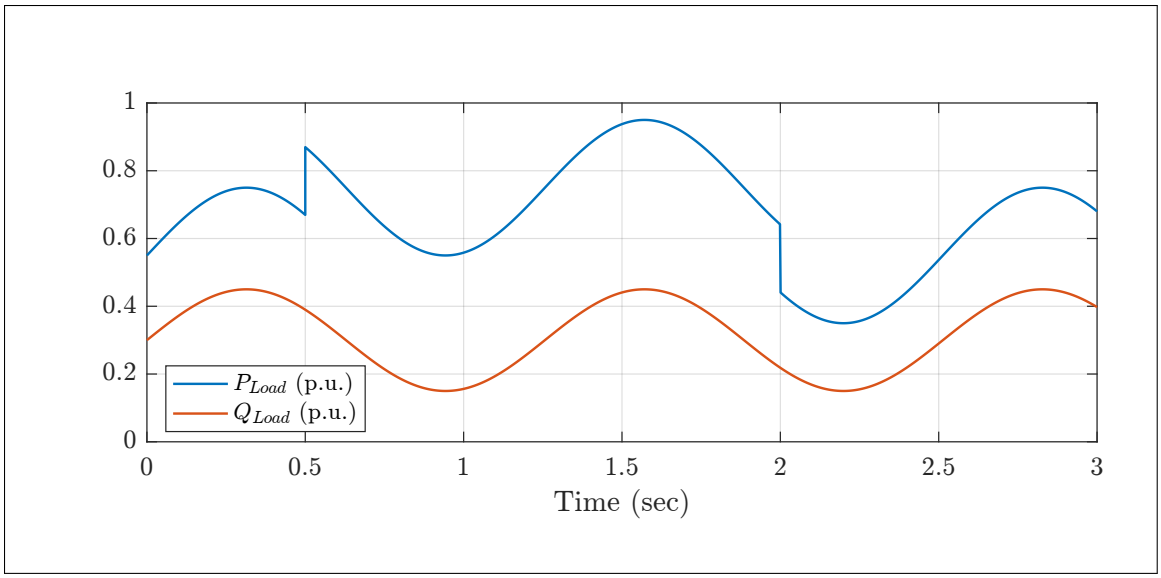

Figure 7-2: Total three-phase load demand.

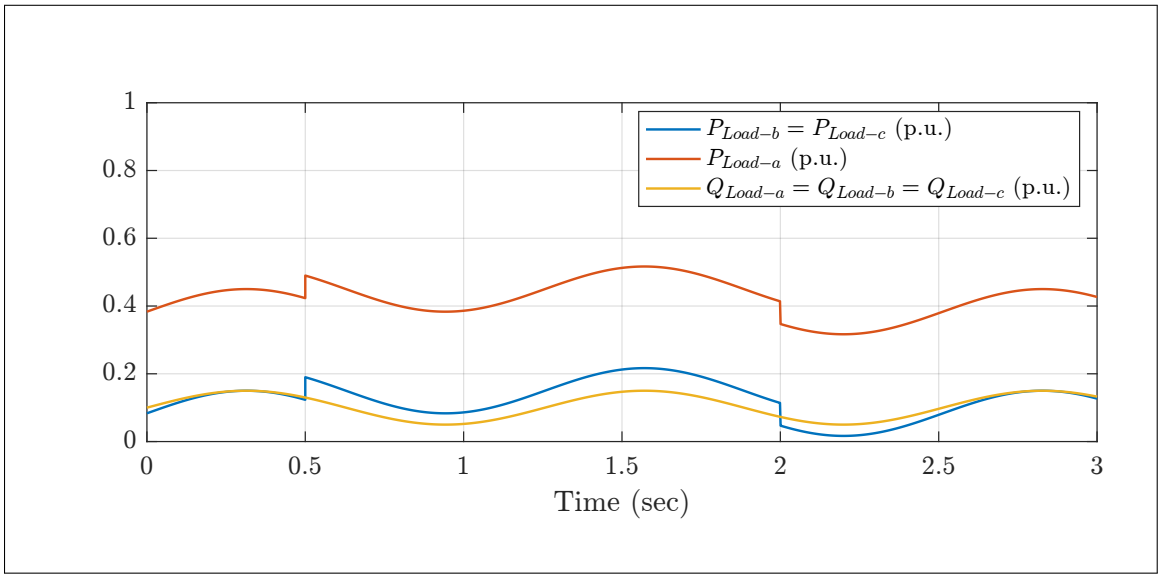

Figure 7-3: Per-phase load demand.

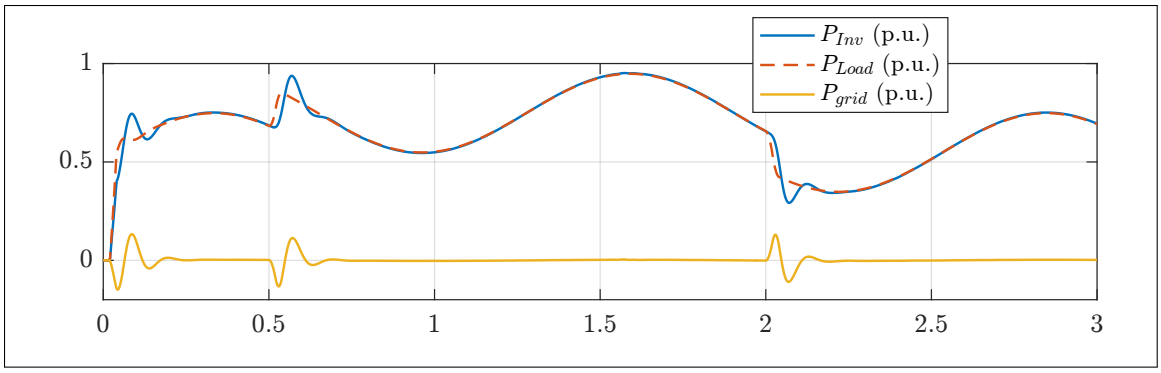

Figure 7-4: HESS AC side active power flows.

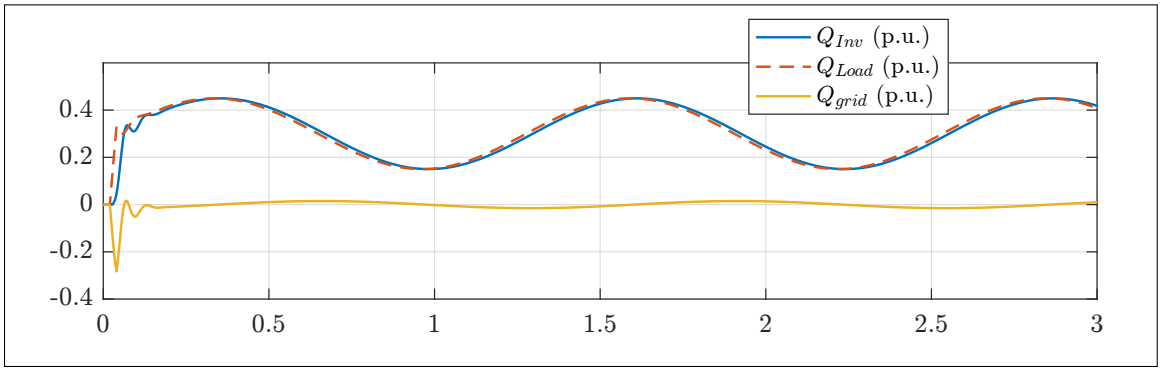

Figure 7-5: HESS AC side reactive power flows.

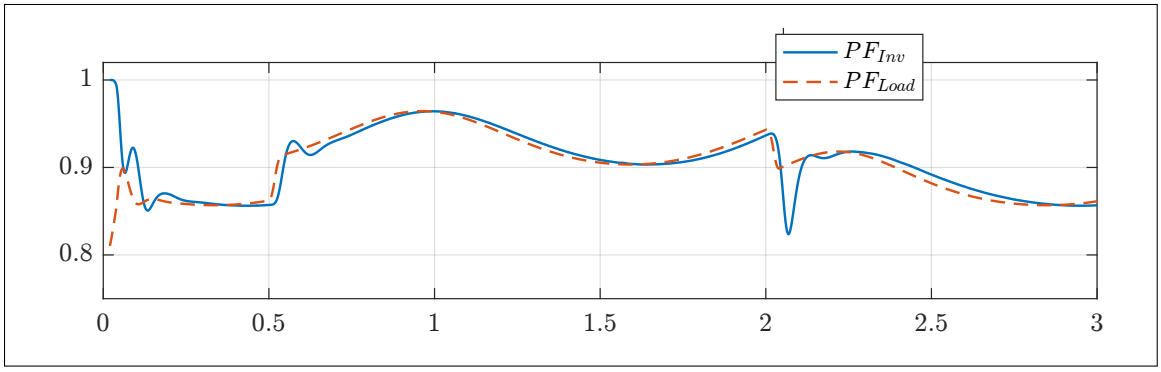

Figure 7-6: HESS inverter and load power factor.

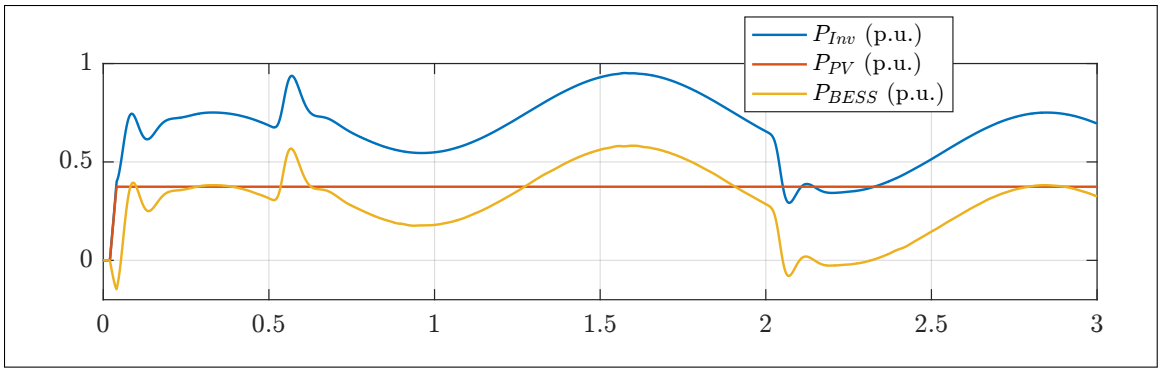

Figure 7-7: HESS DC side power flows.

I_{PV} is a constant proportional to the PV power.

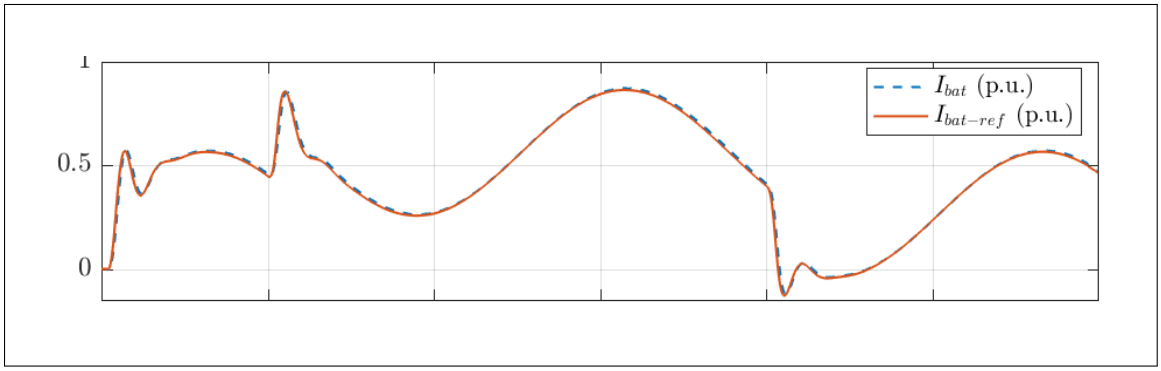

Figure 7-8: BESS current regulated by CDC.

The reference current is generated by BRCG.

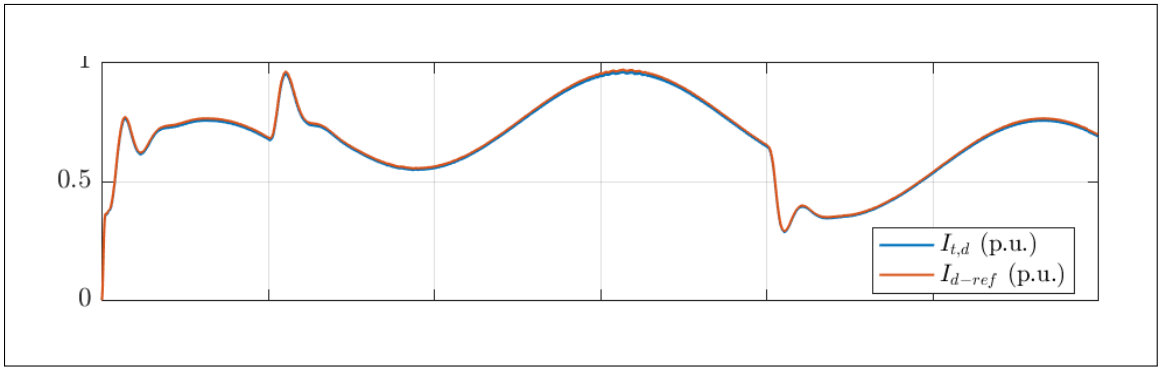

Figure 7-9: Inverter d-axis current regulated by ICC.

The reference current is generated by DCVC. This current is proportional to P_{inv}.

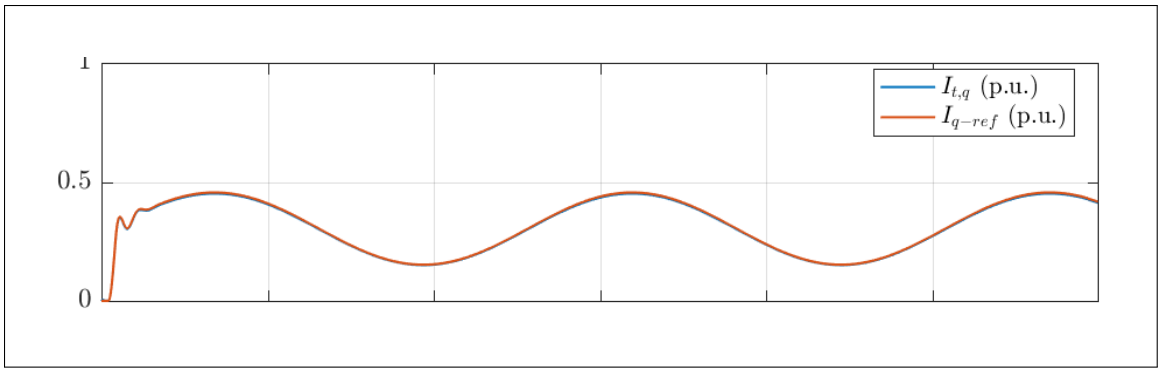

Figure 7-10: Inverter q-axis current regulated by ICC.

The reference current is generated by the combined GFVR & GPIA scheme. This current is proportional to Q_{inv}.

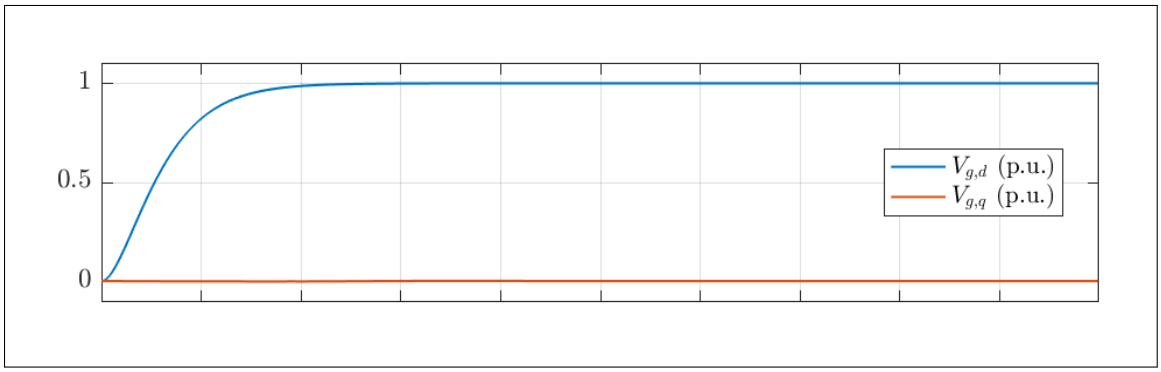

Figure 7-11: Grid dq-axes voltage.The q component is forced to zero by PLL scheme.

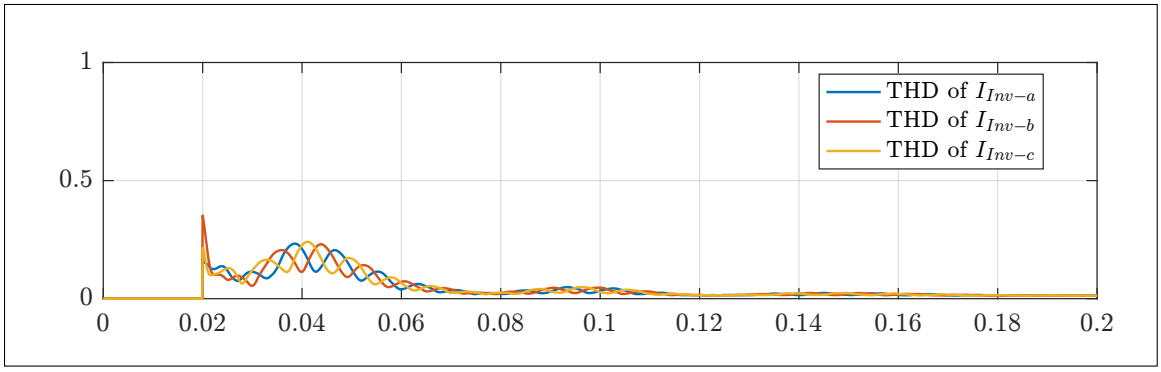

Figure 7-12: HESS inverter three-phase current total harmonic distortion.

7.2.2 HESS Response With Step Load Demand

In this simulation case the household load demand exhibits some step-wise variation. And the load demand for active and reactive power is the same. Additionally, PV is operating under irradiance level variation. The household balance load demand and PV irradiance level are shown in Fig. 7-13 and Fig. 7-14.

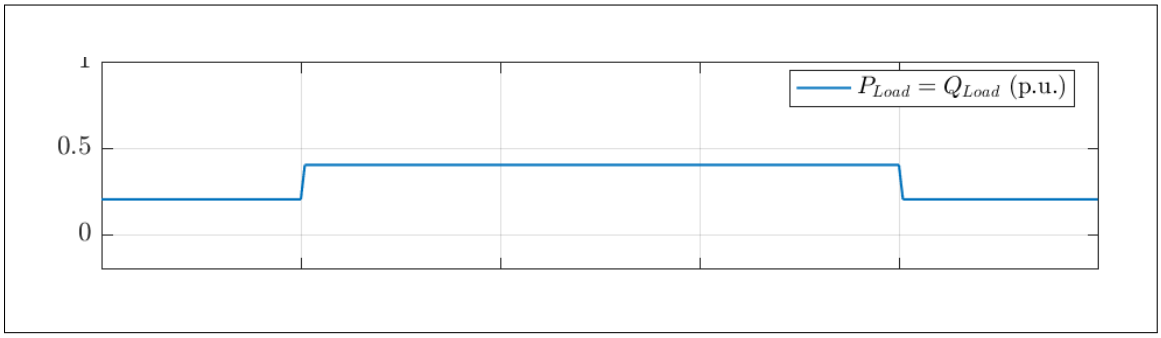

Figure 7-13: Total three-phase balance load demand.

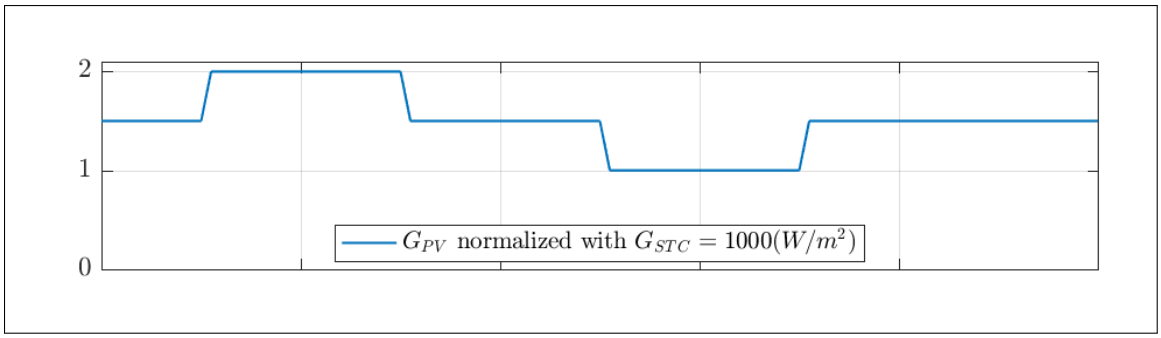

Figure 7-14: PV irradiance variation.

Prior to presenting the HESS response for this simulation test case, the following points are important to be noted:

- The total simulation time is 2.5 seconds and all the figures are plotted in this time interval.
- The GFVR scheme is disabled.
- DC link refernce voltage is set to $V_{DC-ref} = 1000$ V.
- The GPIA scheme is active and in steady state condition it injects the amount of active power requested by GPMU (0.3 p.u.) into the grid.
- The CDM and BRCG schemes automatically set the battery operational state (charge-discharge) according to the excess available PV power.

- The load demand is balanced and it has a constant power factor.

In the following the HESS performance result is presented.

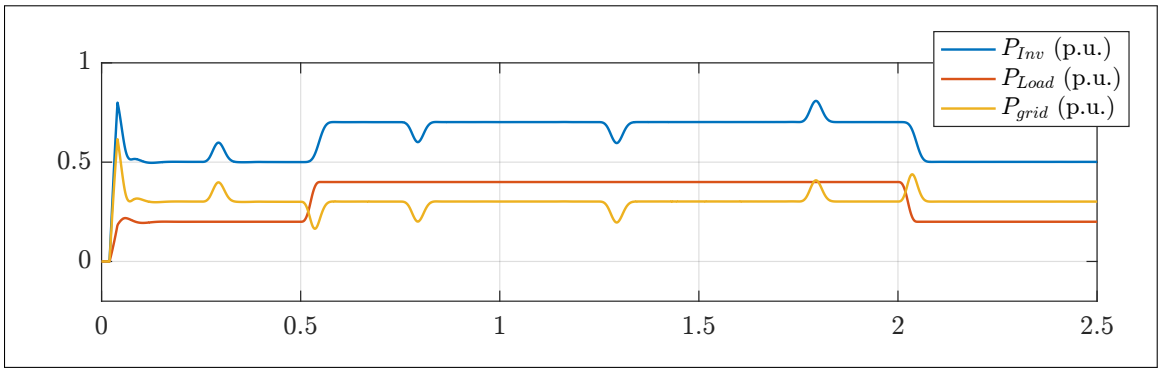

Figure 7-15: HESS AC side active power flows.

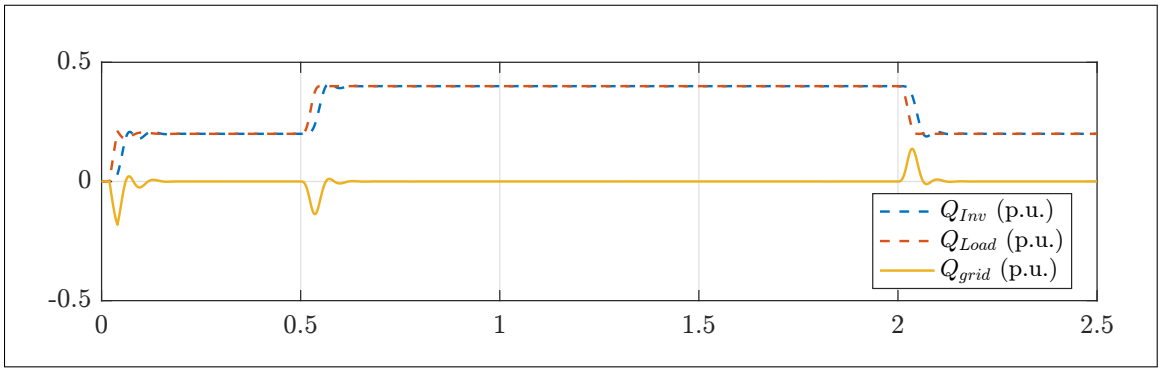

Figure 7-16: HESS AC side reactive power flows.

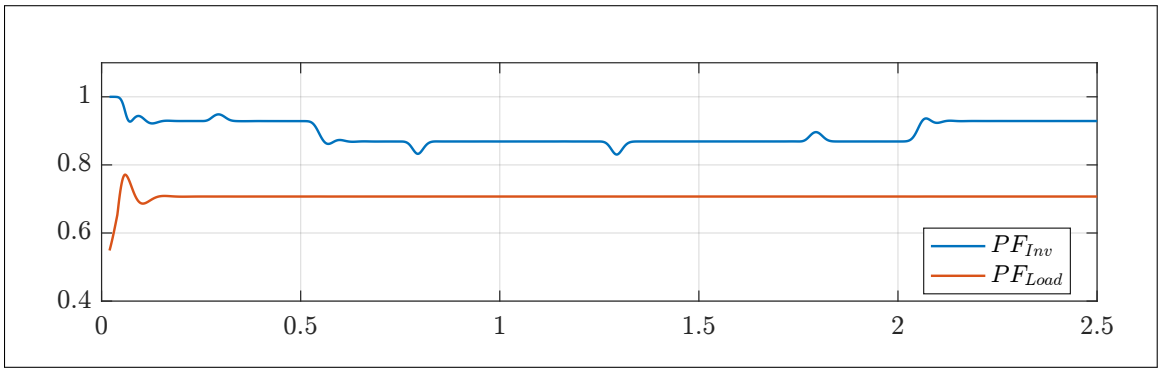

Figure 7-17: HESS inverter and load power factor.

The PF imbalance is due to the amount of active power injected to the grid by HESS inverter.

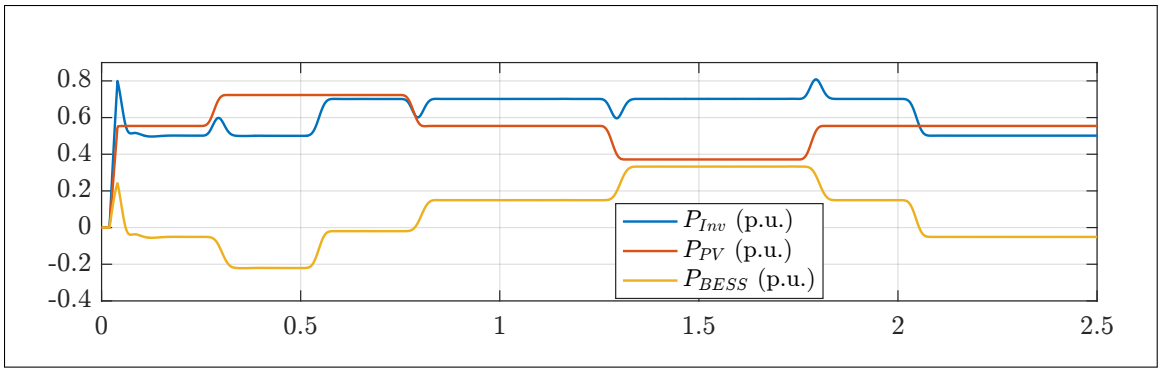

Figure 7-18: HESS DC side power flows.

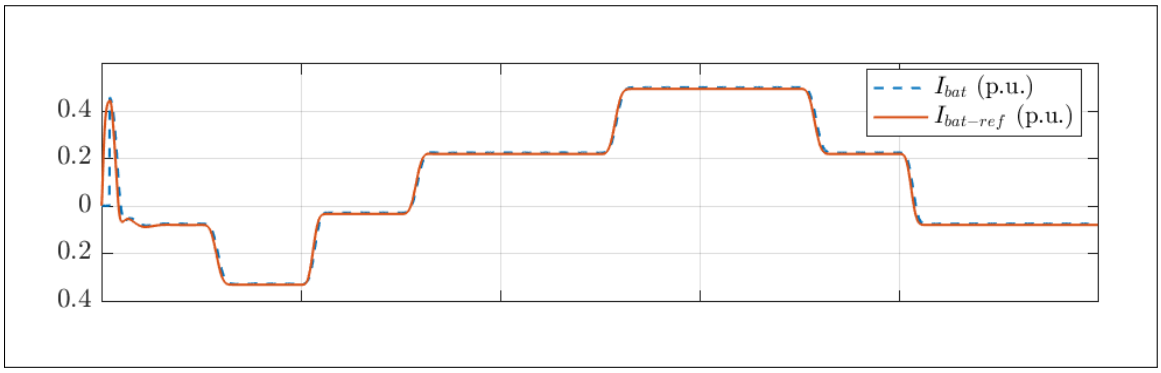

Figure 7-19: BESS current regulated by CDC.

The reference current is generated by BRCG.

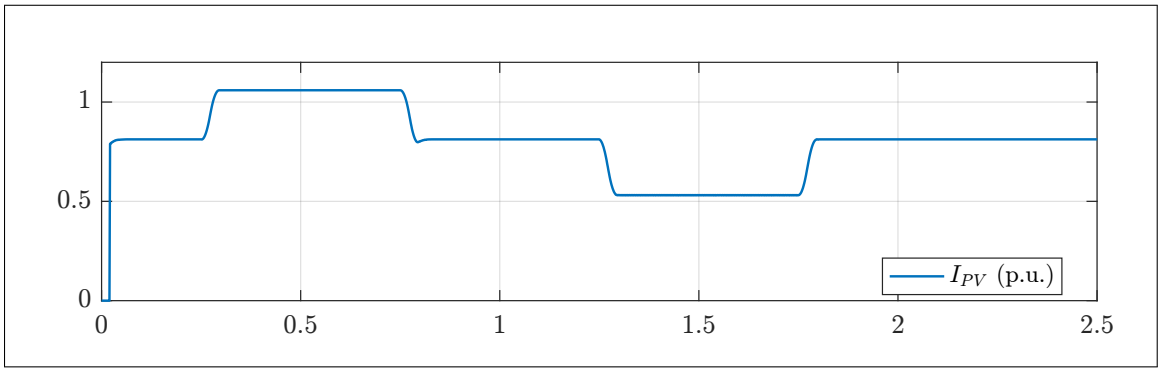

Figure 7-20: PV current.

The excursion beyond 1 p.u. is due to the irradiance level which is higher than STC value.

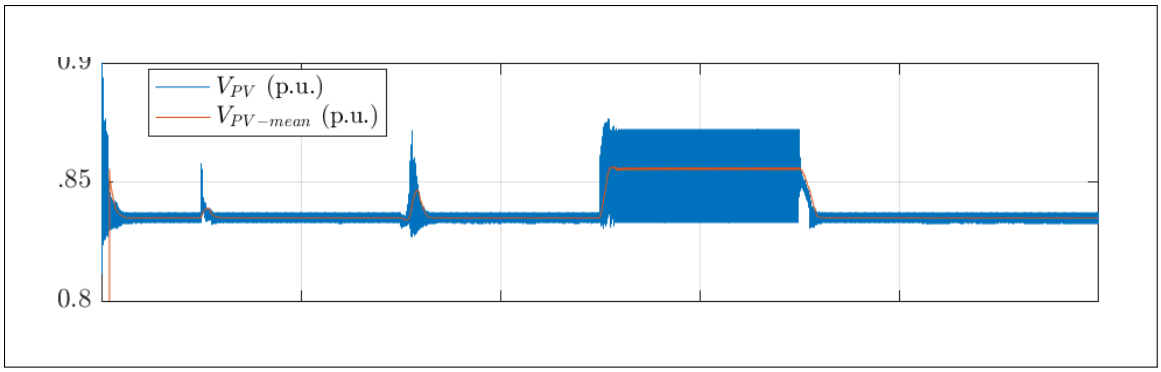

Figure 7-21: PV voltage perturbation by MPPT algorithm.

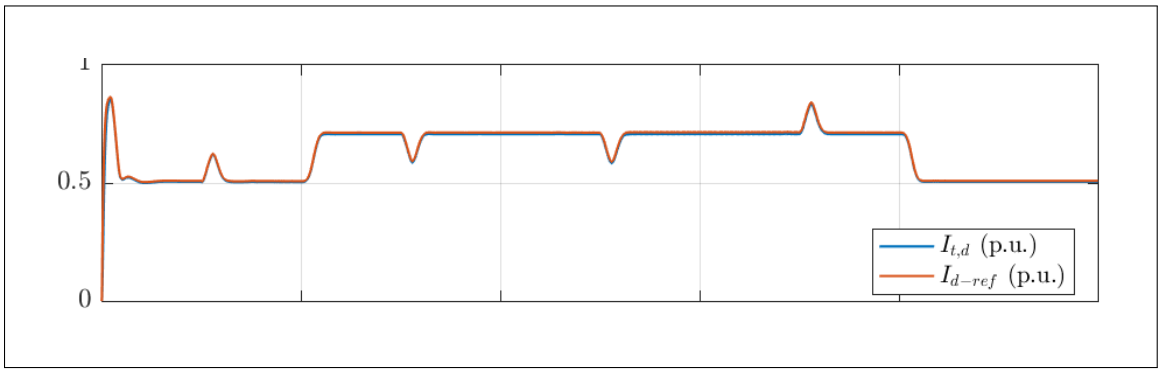

Figure 7-22: Inverter d-axis current regulated by ICC.

The reference current is generated by DCVC. This current is proportional to P_{inv}.

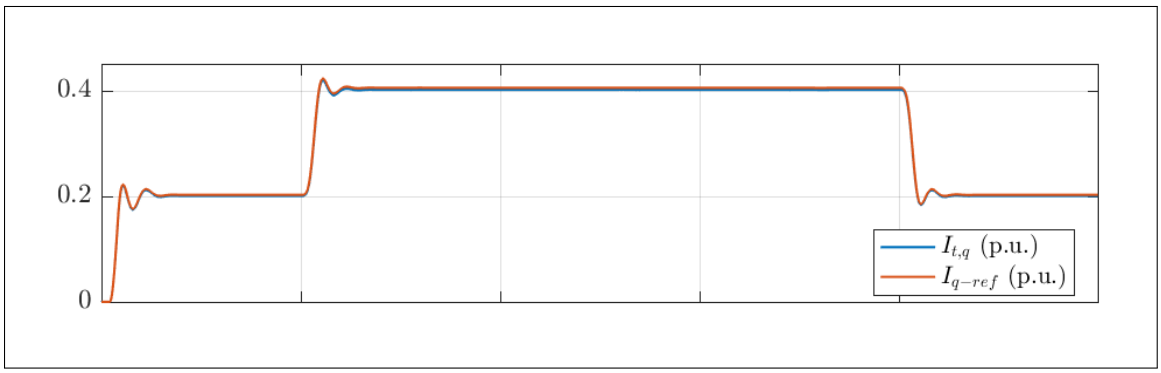

Figure 7-23: Inverter q-axis current regulated by ICC.

The reference current is generated by the combined GFVR & GPIA scheme. This current is proportional to Q_{inv}.

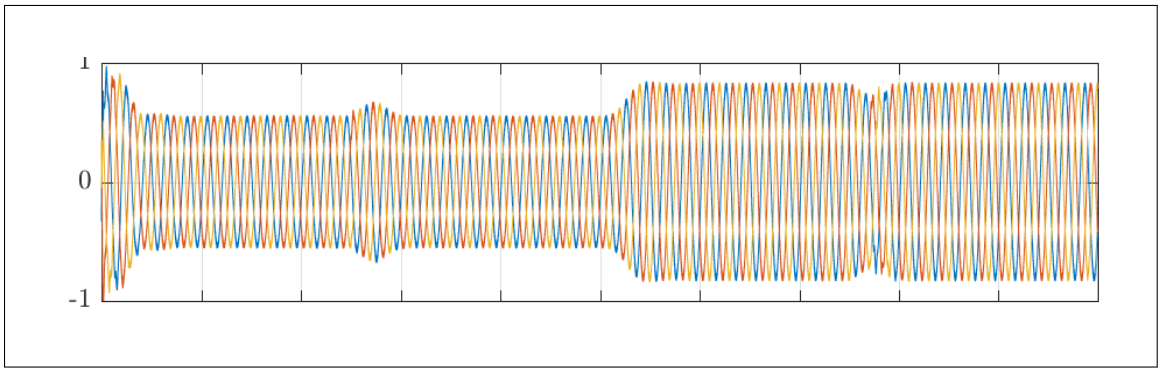

Figure 7-24: Three-phase inverter current in p.u. value, t = 0 - 1 sec.

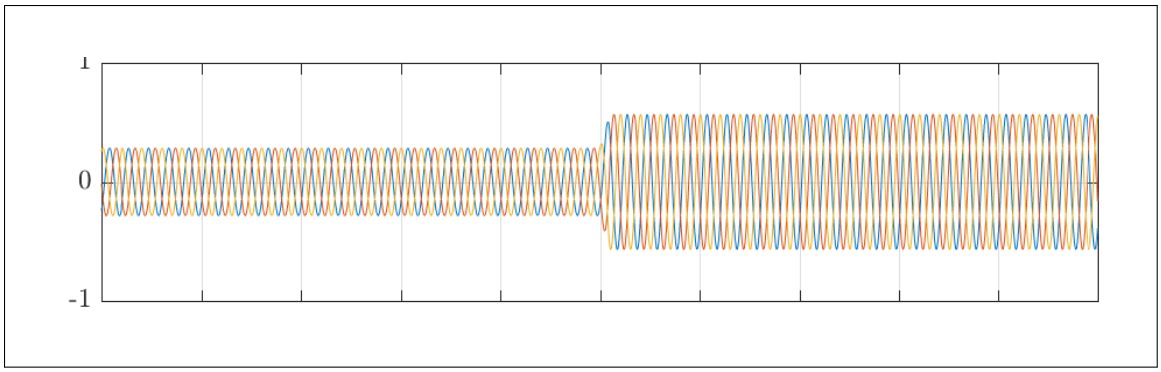

Figure 7-25: Three-phase load current in p.u. value, t = 0 - 1 sec.

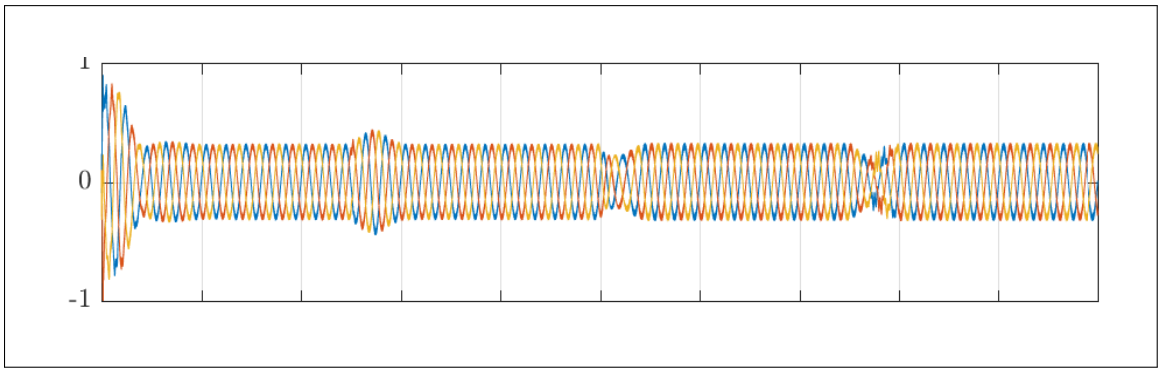

Figure 7-26: Three-phase grid current in p.u. value, t = 0 - 1 sec.

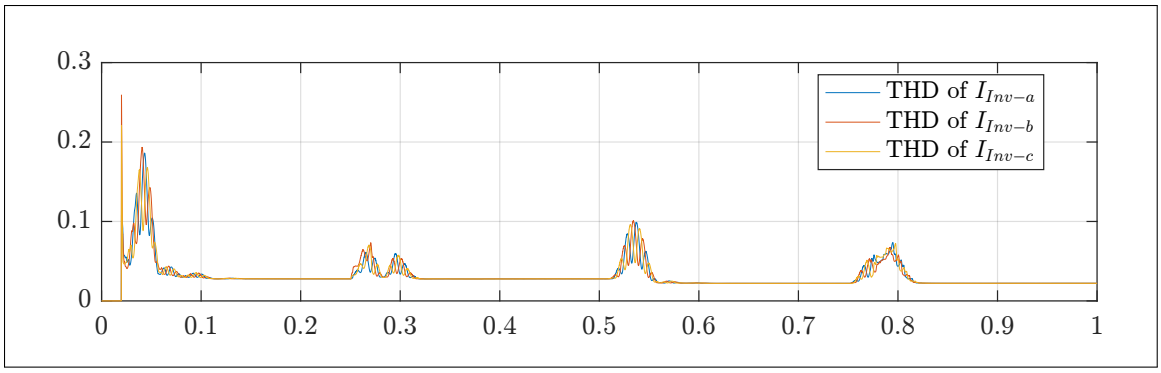

Figure 7-27: HESS inverter three-phase current total harmonic distortion.

7.2.3 HESS Response With Unbalanced Step Load Demand

This test case is similar to the previous case. This is presented in order to show the CDM scheme action when the BESS state of charge hits its lower limit. Moreover, the HESS capability responding unbalanced load is discussed. For the sake of compactness only the results regarding the DC and AC side power flows are presented.

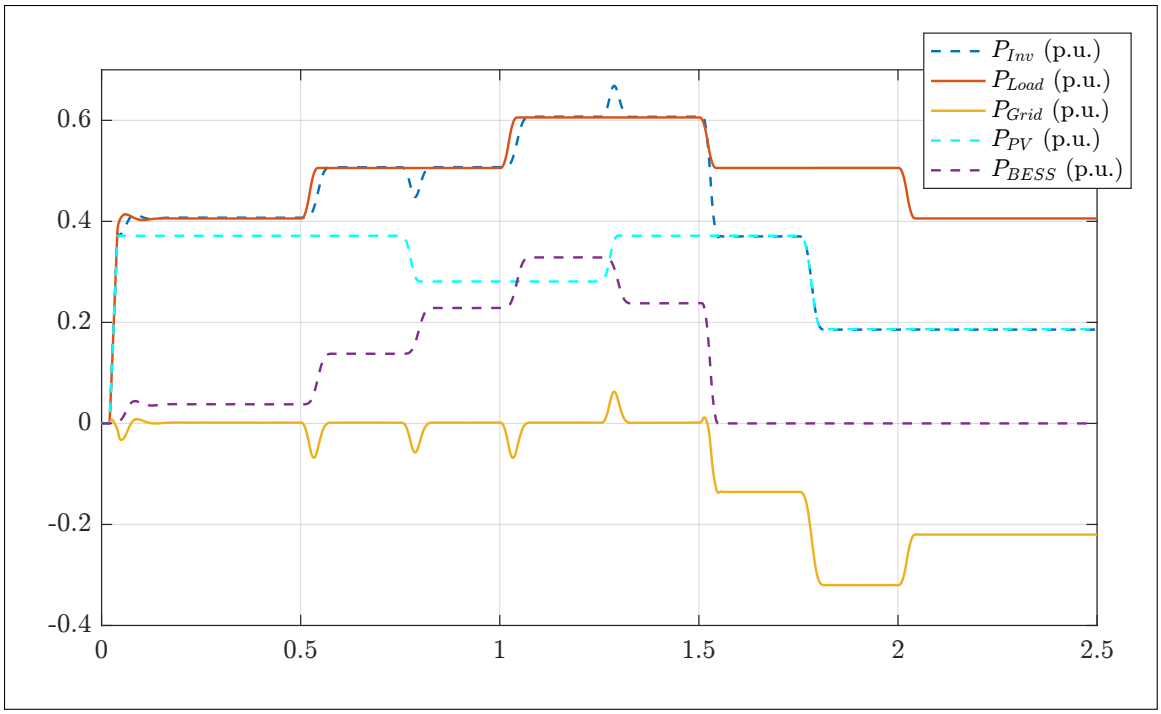

Figure 7-28: HESS DC and AC side power flows.

At t=1.5 sec. the BESS SoC reaches its minimum limit, therefore the CDM and BRCG scheme set the BESS current to zero. Thus, the grid power fills the gap between PV power

and Load demand.

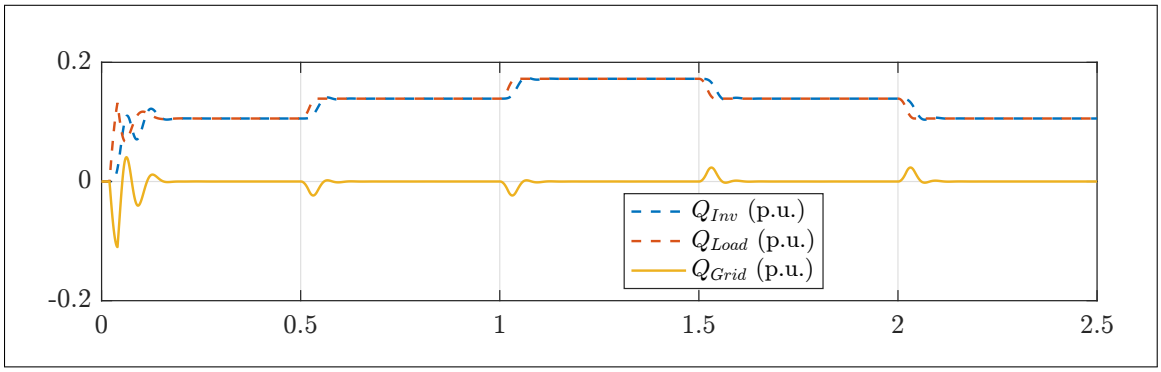

Figure 7-29: HESS AC side reactive power flows.

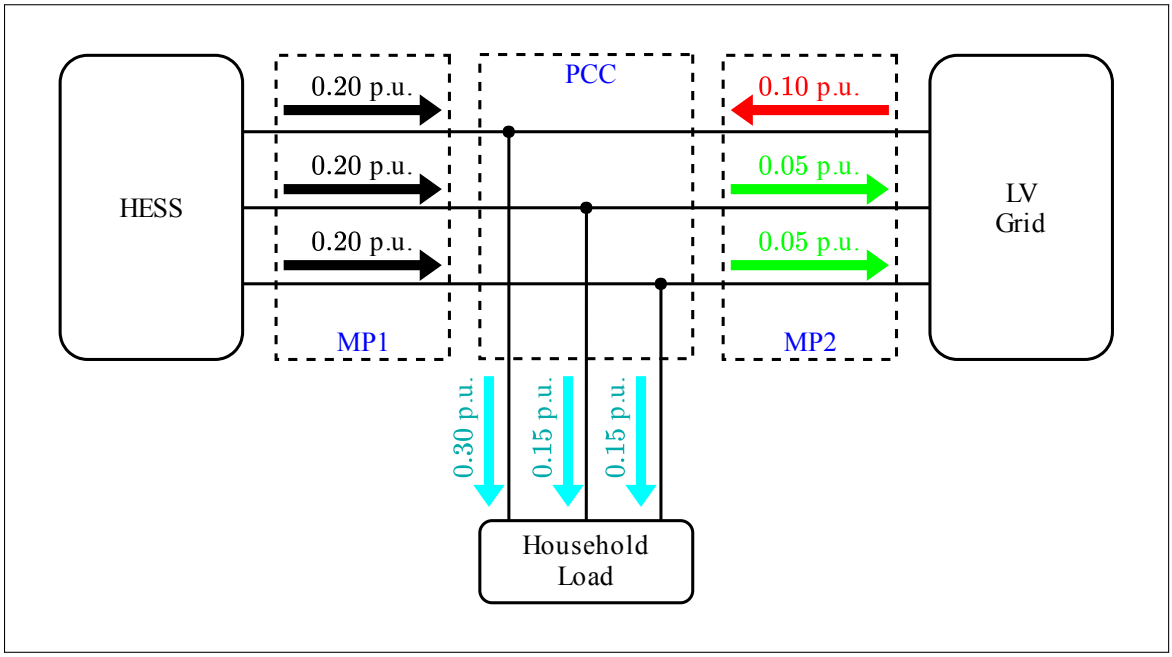

Figure 7-30: HESS AC side active power flows at t=1.25 sec.

However the load demand is unbalanced, inverter provides balanced three-phase power (due to dq frame PFC implementation) and the grid cooperates (injection-absorption) in shaping the per-phase inverter power according to per-phase load demand.

7.3 Laboratory Equipments and Test Setup

The laboratory test setup is shown in Fig. B.3. In which the the device under test (DUT) is a commercial HESS which also includes the DC - DC boost and BBBC. The circuit topology of these components is the same as the models presented in Chapter 3. For the test cases an actual BESS is used. And for the PV component the PV emulator is used. Moreover, for the test cases in which a stiff LV grid is required, the utility grid is used. And for the cases in which the grid frequency-voltage dynamics can not be neglected, the grid emulator is deployed. And the load demand setting is adjusted via supervisory control and data acquisition (SCADA) system. Additionally, the measurement data is captured by the five measuring devices shown in Fig. B-3.

7.4 Laboratory Verification Test Cases

In this section the results regarding the HESS model verification is presented by comparing the behavior of a commercial HESS and the developed model. For all the test cases, the measurement sampling time is 200 ms. Unfortunately, the data which is captured by the measurement devices are noisy. To address this issue, in the presented results the moving average method and interpolation techniques are used.

7.4.1 HESS Step Response

In this test case the commercial HESS response to the load step-wise variation is observed. It must be considered that the HESS inverter is forced to operate with constant power factor. Therefore, as the HESS AC side active power increases, also its reactive power increases proportionally to keep PF = 0.9. For the sake of compactness the simulation results for this case is not presented. And the laboratory results can be easily compared to HESS model simulation results presented in Sections 7.2.2 and 7.2.3.

The interesting point to be mentioned is that the DUT settling time for step-wise changes in the load demand is approximately 50 seconds. While, the model developed in this thesis responds to the similar load demand variation in less than a second (Fig. 7-28). This is mainly due to the lower inverter switching frequency setting of the DUT. Moreover, since the DUT is designed for operating in smart LV grid, there are some auxiliary schemes implemented regarding its real-time communication with the virtual power plant operator.

This beside the system delays and electrical protection design can shift the HESS controller bandwidths lower than the ones presented in Fig. 7-1.

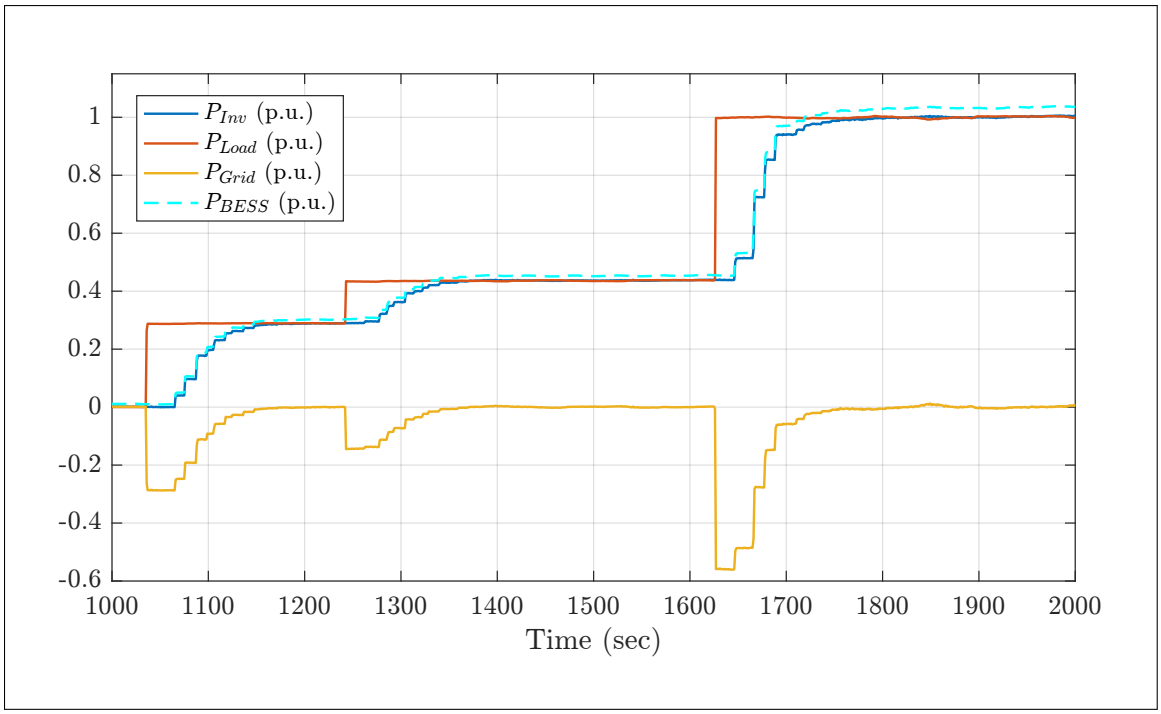

Figure 7-31: DUT step response to active power demand.

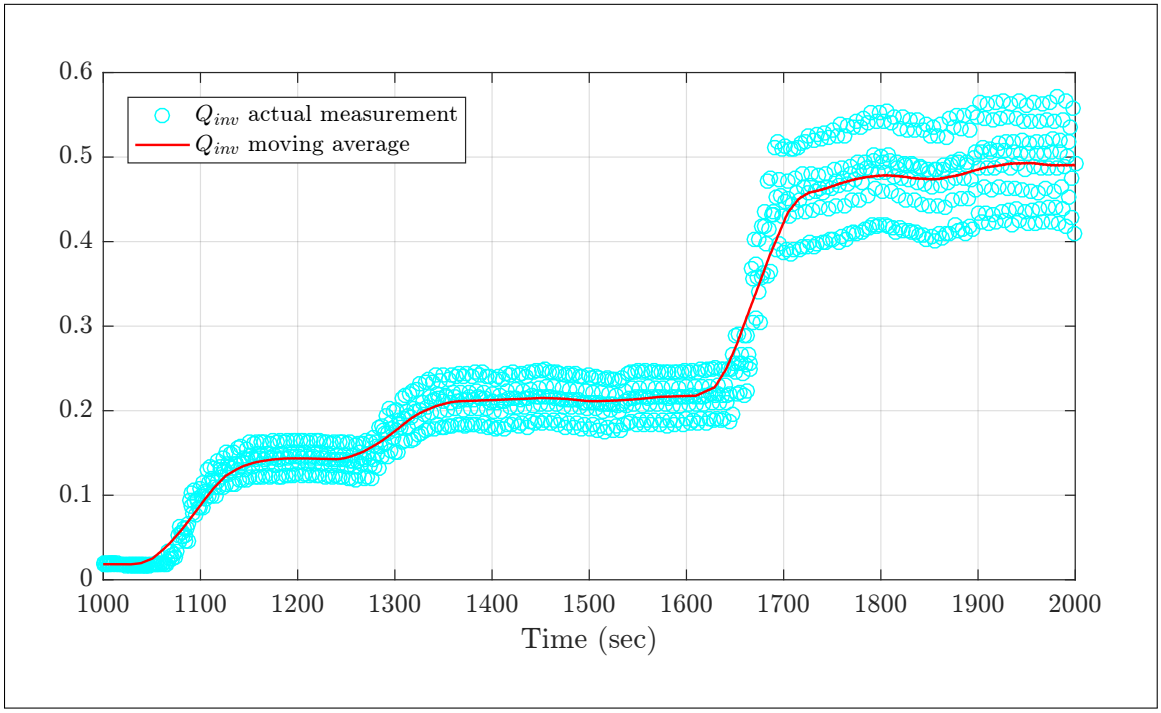

Figure 7-32: DUT AC side reactive power.

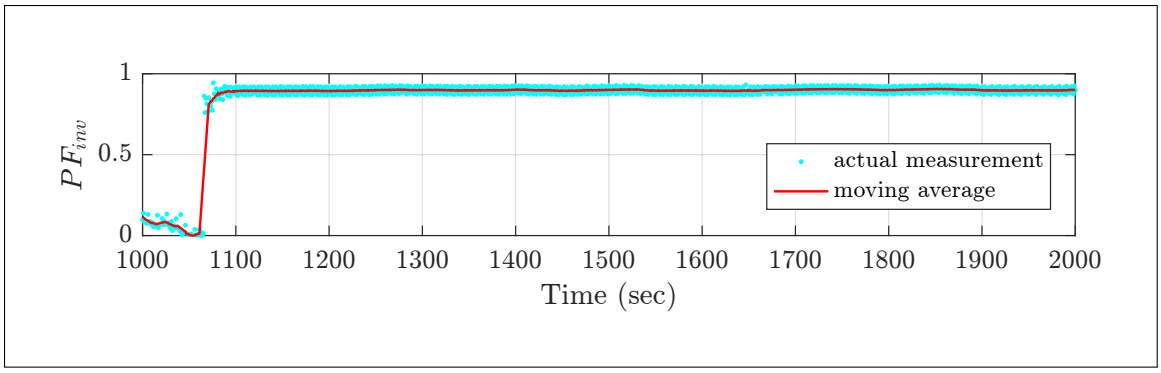

Figure 7-33: DUT inverter power factor.

7.4.2 HESS Power Factor - Active Power Droop

In this test case the PF - P droop curve shown in Fig. 7-34 is adjusted for the inverter stage embedded in the commercial HESS. The idea is to adjust the inverter PF with respect to the active power (in per-unit) which is delivered to the AC side (either load or grid). This curve forces the inverter to also deliver a proportional amount of reactive power when $P_{inv} > 0.5$. Thus, when the active power goes beyond this limit, the inverter power factor decreases. The final value for PF is 0.92 which corresponds to $P_{inv} = 1$ and $Q_{inv} = \sqrt{1-(PF)^2}.P_{max} = 0.39$.

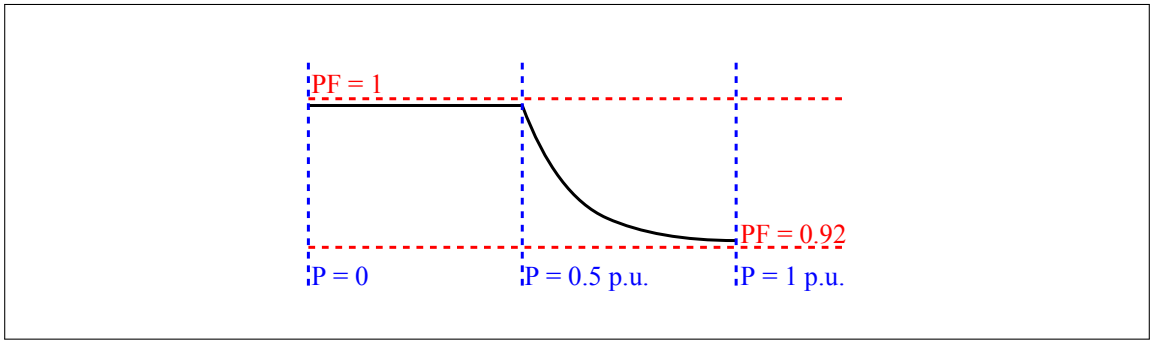

Figure 7-34: Inverter PF - P droop curve.

In this test case the DC power is provided by BESS, and the overall simulation time is 550 seconds. In Fig. 7-35 the start-up transient is not shown. To process the measurement data and cancel out the noise the moving average is applied with the window of 190 and 150 samples for PF and inverter power respectively. As it is depicted in Fig. 7-35 the PF decrement starts when active power becomes greater than 0.5.

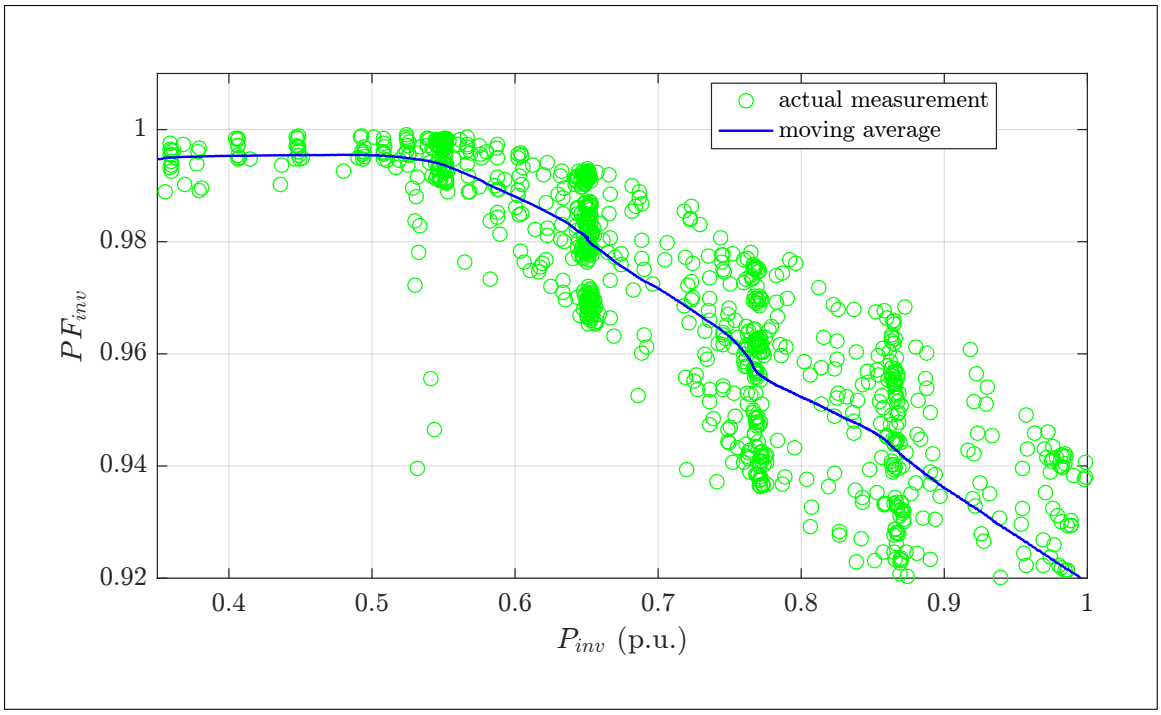

Figure 7-35: Commercial HESS inverter power factor vs. active power.

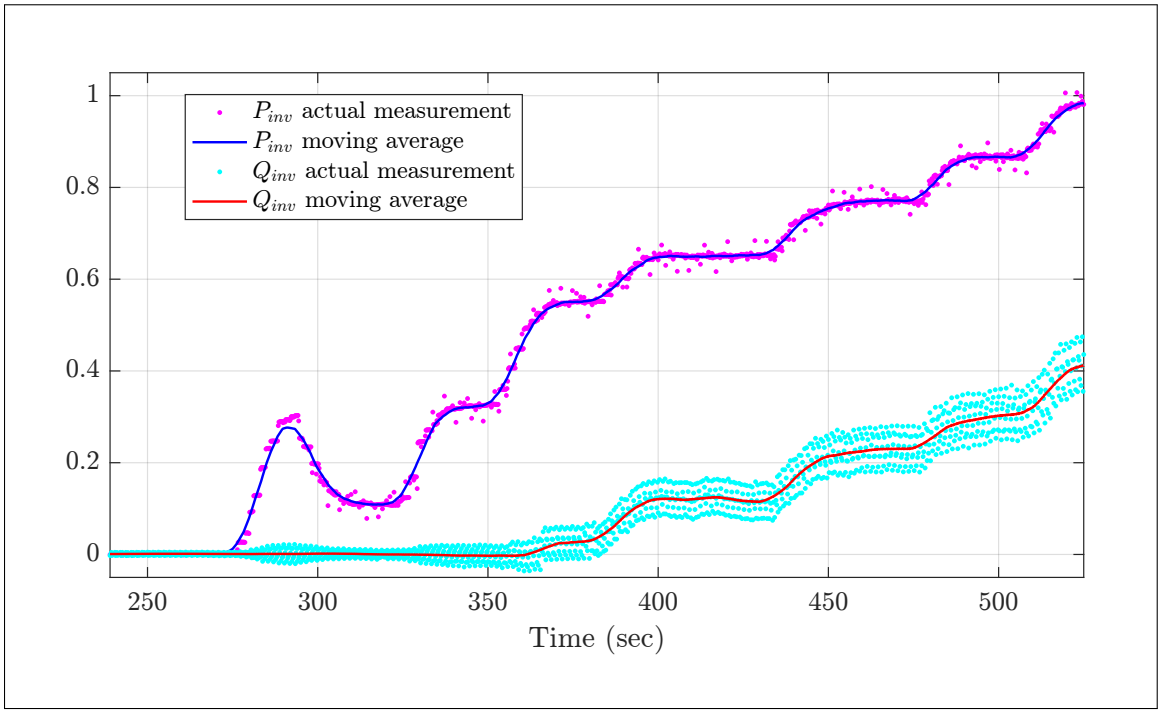

Figure 7-36: Inverter active and reactive power.

As it is shown in Fig. 7-36, when the increasing active power goes beyond 0.5, the inverter

reactive power increases proportionally. This lets the inverter to achieve the required PF setting. For this case the active power is increased step-wise from 0 to 1.

Simulation Result

In order to verify the simulation result for this test case the droop curve shown in Fig. 7-34 is fed in to GFVR scheme. As it is explained in Chapter 5, the GFVR controller can regulate the injected power to the grid according to any required droop curve. The simulation time is 0.6 seconds and the inverter active power is increased step-wise.

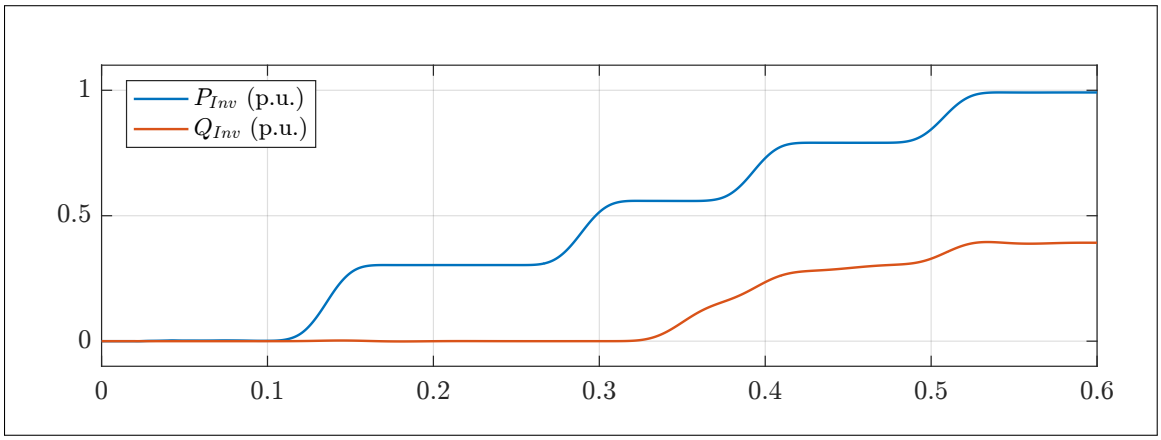

Figure 7-37: Inverter active and reactive power.

And the actual PF calculated based on P_{inv} and Q_{inv} is shown in Fig. 7-38. This PF response is almost the same as the commercial HESS PF - P droop setting.

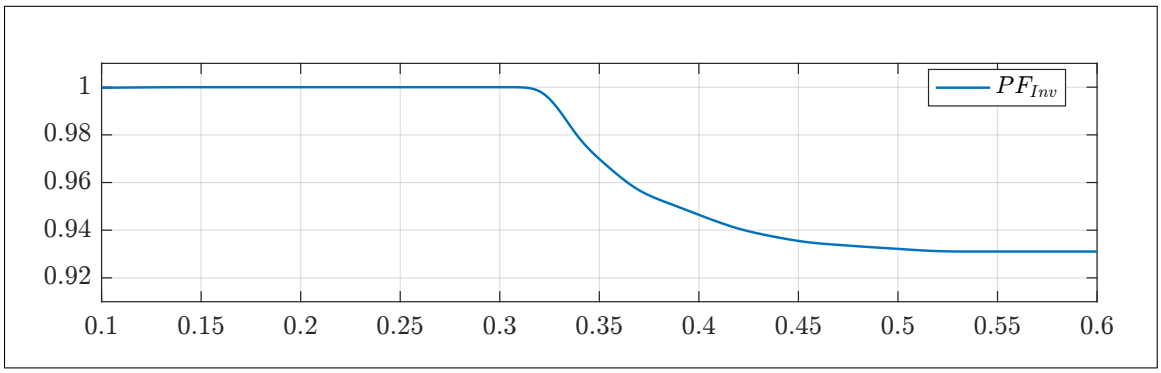

Figure 7-38: Inverter power factor.

7.4.3 HESS Voltage - Reactive Power Droop

In this test case the Q -V droop curve shown in Fig. 7-39 is set for the commercial HESS. The objective is to observe how the HESS responds to the grid voltage variation. As it is mentioned in Chapter 5, it is expected that the HESS absorbs power if the grid voltage is higher than the allowed upper limit. And HESS must inject reactive power to the grid if voltage drops bellow the lower limit. In this test case since grid voltage variation is required

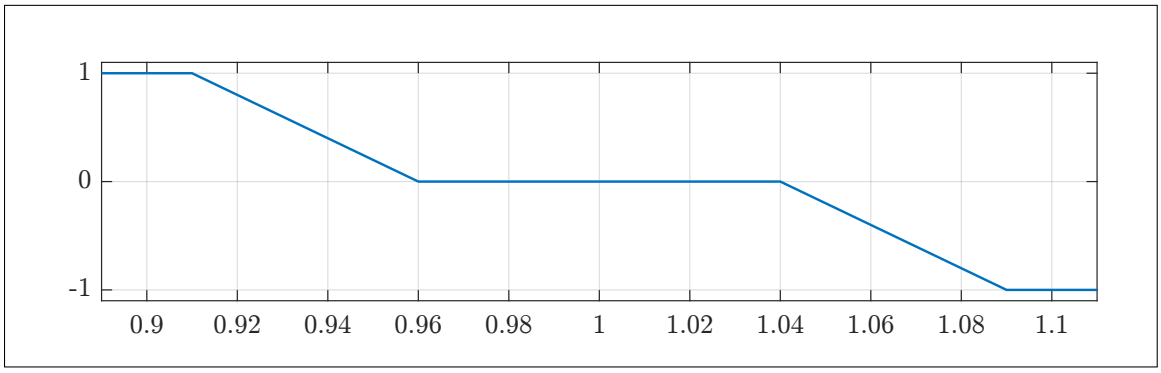

Figure 7-39: Inverter Q - V droop curve.

the grid emulator shown Fig. B-3 is used. Therefore, the voltage sweep from 0.91 to 1.09 p.u. is performed and the HESS reactive power is measured. The actual measurement data and the interpolated data are presented in Fig. 7-40. The polynomial interpolation is performed by using Matlab curve fitting toolbox.

Simulation result

For this case the droop curve shown Fig. 7-39 is fed into the GFVR scheme. Considering the fact that the HESS model in this thesis is linked to the stiff LV grid model, it is not possible to perform the voltage sweep. Regardless of this, the response of the GFVR reactive power controller to the reference reactive power value based on the droop curve is depicted in Fig. 7-41.

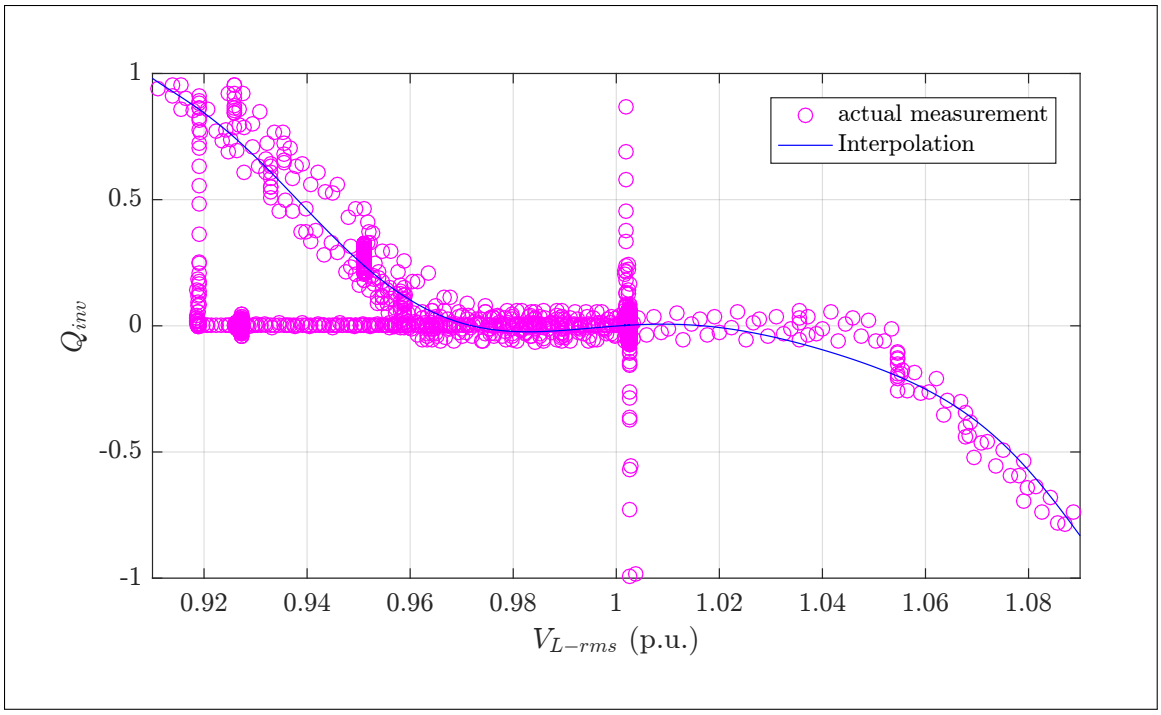

Figure 7-40: Commercial HESS inverter reactive power vs. voltage.

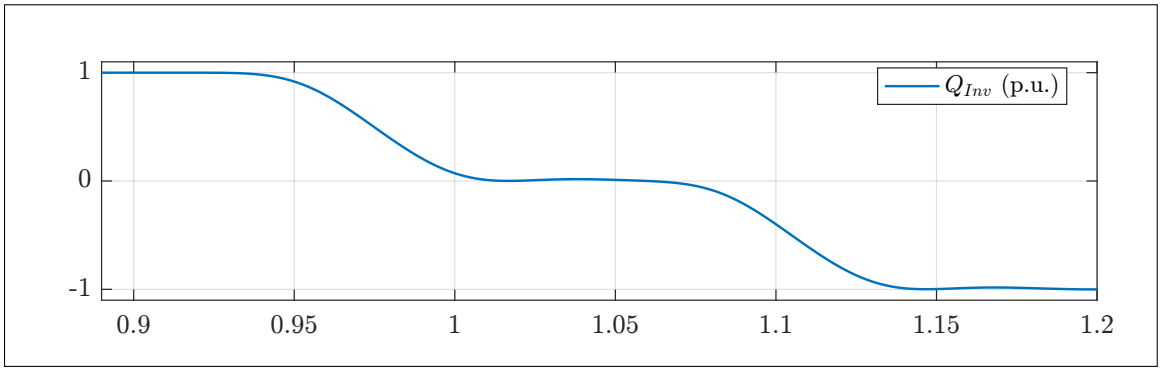

Figure 7-41: Commercial HESS inverter GFVR reactive power response.

7.5 Further Development

The multi-functional PV electrochemical storage system model developed in this thesis can exhibit performance improvement by adopting the following controlling schemes and component models:

- MPPT algorithm with adaptive step size can be designed which improves the PV efficiency.
- DC link voltage equalizing scheme can be implemented in order to gain better DC link voltage stabilization.
- Third harmonic injection technique can be implemented in order to extend the inverter voltage range with the same DC link reference voltage.
- A LCL filter can substitute the RL filter, in order to decrease AC side losses. Moreover, a sensor-less LCL filter control can be implemented by designing a non-linear observer. This leads to reduction of the required measurement points.
- Instead of the static P-F and Q-V droop curves presented in Chapter 5, dynamic curves can be adopted in which the amount of grid power injection-absorption is adjusted dynamically to expedite the grid frequency-voltage recovery.
- Islanding detection and operation mode control can be implemented, which helps HESS to continue its operation under faulty grid conditions.

Chapter 8

Activities Done at AIT

While developing my master thesis at AIT, I could attend the LEAFS project research team regular monthly meetings. Which helped me to improve my communication skills with the other team members working on a long-term industrial-research project.

Moreover, I was given the chance to use the AIT Smartest Research Test Lab, which helped me to gain experience in working with solar inverters, BEES, PV emulator and grid emulator. Moreover, as an optional activity, I have attended the PowerFactory intensive workshop instructed by a tutor from DigSilent GmbH.

I would like to encourage the next generation of STEPS students to possibly join AIT for their thesis project. Since at AIT under a peaceful environment, all the necessary scientific support is provided which facilitates a gainful research experience.

Appendix A

A.1 DC Link Reference Voltage Level Selection

In this section the DC link reference voltage selection criteria is discussed. DC link reference voltage will be expressed in term of inverter terminal voltage. And the peak amplitude of terminal voltages is influenced by steady and transient states of active and reactive power injected to PCC by HESS. to begin with, by recalling (3.34), v_{DC} is stated by:

$$V_{DC} = \frac{2.\bar{V_t}}{m(t)} \tag{A.1}$$

now by replacing $\bar{V_t}$ by its peak amplitude $\hat{V_t}$ and assuming $|m(t)| \leq 1$:

$$V_{DC} \geq 2.\hat{V_t} \tag{A.2}$$

however if third harmonic injection is adopted, $m(t)$ is extended to 1.15 resulting in[8]:

$$V_{DC} \geq \sqrt{3}.\hat{V_t} \tag{A.3}$$

therefore V_{DC} lower bound depends on $\hat{V_t}$. The peak terminal voltage is identified by its dq components as:

$$\hat{V_t} = \sqrt{V_{t,d}^2 + V_{t,q}^2} \tag{A.4}$$

moreover, the dynamics of $V_{t,d}$ and $V_{t,q}$ are described by (5.39), by assuming $R_L \approx 0$ and $V_{g,q} = 0$:

$$\begin{aligned} V_{t,d} &= L.\frac{di_{t,d}}{dt} - L.\omega_0.i_{t,q} + V_{g,d} \\ V_{t,q} &= L.\frac{di_{t,q}}{dt} + L.\omega_0.i_{t,q} \end{aligned} \tag{A.5}$$

Thus, the influence of inverter current on $\hat{V}_t$ is demonstrated. Alternatively, $i_{t,d}$ and $i_{t,d}$ can be written in terms of P and Q based on (5.37):

$$\begin{aligned} i_{t,d} &= \frac{2.P}{3.V_{g,d}} \\ i_{t,q} &= -\frac{2.Q}{3.V_{g,d}} \end{aligned} \tag{A.6}$$

now by inserting (A.6) in (A.5):

$$\begin{aligned} V_{t,d} &= \left(\frac{2.L}{3.V_{g,d}}\right).\frac{dP}{dt} + \left(\frac{2.L.\omega_0}{3.V_{g,d}}\right).Q + V_{g,d} \\ V_{t,q} &= -\left(\frac{2.L}{3.V_{g,d}}\right).\frac{dQ}{dt} + \left(\frac{2.L.\omega_0}{3.V_{g,d}}\right).P \end{aligned} \tag{A.7}$$

Hence the relation between active and reactive power dynamics and terminal voltage is realized. It is inferred by (A.9) that the highest peak voltage occurs when there is a simultaneous changes in P and Q. Therefore, it is assumed that initially $P = P_0\big|_{t=t_0}$ and $Q = Q_0\big|_{t=t_0}$. Then at $t = t_0$ the P_{ref} is changed to $P_0 + \Delta P$ and Q_{ref} is changed to $Q_0 + \Delta Q$. In order to investigate how $P(t)$ and $Q(t)$ respond to their new references, by recalling (5.37) it is illustrated that $P(t)$ and $Q(t)$ exhibit same first order transient behaviour as the output of ICC (Fig. 5-12). As a result, $P(t)$ and $Q(t)$ dynamics can be modelled by constant steady state term and an exponentially decaying term:

$$\begin{aligned} P(t) &= (P_0 + \Delta P) - \Delta P.e^{\frac{-(t-t_0)}{\tau}} \\ Q(t) &= (Q_0 + \Delta Q) - \Delta Q.e^{\frac{-(t-t_0)}{\tau}} \end{aligned} \tag{A.8}$$

where the exponential term time constant τ is defined by the ICC bandwidth. Therefore, by inserting (A.8) in (A.9), and taking the right limit with respect to time (i.e. evaluating the resulting expression at $t = t_0^+$ which replaces the exponential terms with 1) $V_{t,d}(t_0^+)$ and $V_{t,q}(t_0^+)$ are derived as:

$$\begin{aligned} V_{t,d}(t_0^+) &= \left(\frac{2.L}{3.\tau.V_{g,d}}\right).\Delta P + \left(\frac{2.L.\omega_0}{3.V_{g,d}}\right).Q_0 + V_{g,d} \\ V_{t,q}(t_0^+) &= -\left(\frac{2.L}{3.\tau.V_{g,d}}\right).\Delta Q + \left(\frac{2.L.\omega_0}{3.V_{g,d}}\right).P_0 \end{aligned} \tag{A.9}$$

As a result $V_{t,d}(t_0^+)$ and $V_{t,q}(t_0^+)$ can be evaluated by the knowing P_0, ΔP, Q_0 and ΔQ. And accordingly, $\hat{V}_t$ is calculated by (A.4). Thus depending on the modulation scheme either (A.3) or (A.2) identifies the required DC voltage reference level.

A.2 HESS per-unit System

HESS base values for per unit system are presented in the following tables. The point to be considered is that the base values are obtained based on inverter rated power P_b, line to neutral voltage amplitude $\hat{V}$ and grid nominal angular frequency ω_0.

Table A.1: AC side base values.

Quantity	Expression
power	$P_b = \frac{3}{2}.V_b.I_b$
voltage	$V_b = \hat{V}$
current	$I_b = \frac{2.P_b}{3.V_b}$
impedance	$Z_b = \frac{V_b}{I_b}$
capacitance	$C_b = \frac{1}{Z_b.\omega_b}$
inductance	$L_b = \frac{Z_b}{\omega_b}$
frequency	$\omega_b = \omega_0$

Table A.2: DC side base values.

Quantity	Expression
power	$P_{b,dc} = V_{b,dc}.I_{b,dc} = P_b$
voltage	$V_{b,dc} = 2.V_b$
current	$I_{b,dc} = \frac{3}{4}.I_b$
impedance	$R_{b,dc} = \frac{8}{3}.Z_b$
capacitance	$C_{b,dc} = \frac{3}{8}.C_b$
inductance	$L_{b,dc} = \frac{8}{3}.L_b$
frequency	——

A.3 Arbitrary and Stationary Frame Transformation

Table A.3: Park and Clark transformations.

Transformation	**Refernce Frames**	**Matrix**
Clark	abc to $\alpha\beta$	$\frac{2}{3}.\begin{bmatrix} 1 & -\frac{1}{2} & -\frac{1}{2} \\ 0 & \frac{\sqrt{3}}{2} & -\frac{\sqrt{3}}{2} \end{bmatrix}$
Inverse Clark	$\alpha\beta$ to abc	$\begin{bmatrix} 1 & 0 \\ -\frac{1}{2} & \frac{\sqrt{3}}{2} \\ -\frac{1}{2} & -\frac{\sqrt{3}}{2} \end{bmatrix}$
Park	$\alpha\beta$ to dq	$\begin{bmatrix} \cos\theta & \sin\theta \\ -\sin\theta & \cos\theta \end{bmatrix}$
Inverse Park	dq to $\alpha\beta$	$\begin{bmatrix} \cos\theta & -\sin\theta \\ \sin\theta & \cos\theta \end{bmatrix}$

A.4 AC Power Transmission

The complex power flow derivation is done under the source constant voltage assumption. moreover, the line section exhibits RL behaviour. Thus the apparent power flow through

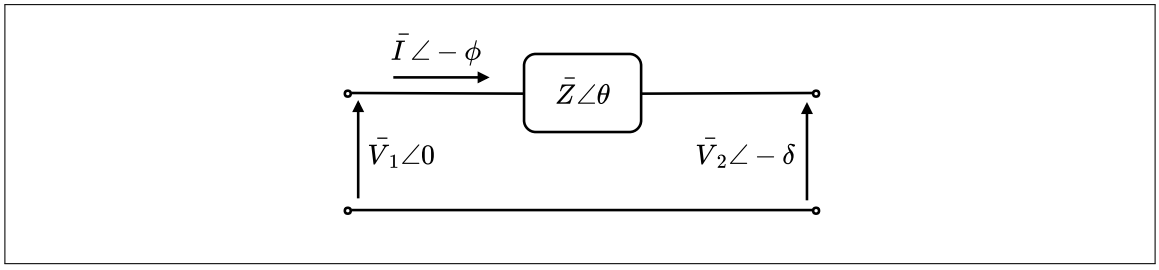

Figure A-1: Power flow through a line section.

the line section shown in Fig. A-1 is described by:

$$\begin{aligned}\bar{S} = P + jQ = \bar{V}_1.\bar{I}^* &= \bar{V}_1.\left(\frac{\bar{V}_1 - \bar{V}_2}{\bar{Z}}\right)^* \\ &= V_1.\left(\frac{V_1 - V_2.e^{j\delta}}{Z.e^{-j\theta}}\right) \\ &= \frac{V_1}{Z}.e^{j\theta} - \frac{V_1.V_2}{Z}.e^{j\theta+\delta}\end{aligned} \tag{A.10}$$

Then by Euler's formula application, the apparent power can be decomposed into active and reactive power as:

$$\begin{aligned}P &= \frac{V_1^2}{Z}.\cos\theta - \frac{V_1.V_2}{Z}.\cos(\theta+\delta) \\ Q &= \frac{V_1^2}{Z}.\sin\theta - \frac{V_1.V_2}{Z}.\sin(\theta+\delta)\end{aligned} \tag{A.11}$$

now by writing the line section impedance as $Z.e^{j\theta} = R + jX$ and consequently reforming (A.11) into:

$$\begin{aligned}P &= \frac{V_1}{X^2+R^2}\Big(R.\big(V_1 - V_2\big).\cos\delta + X.V_2.\sin\delta\Big) \\ Q &= \frac{V_1}{X^2+R^2}\Big(X.\big(V_1 - V_2\big).\cos\delta + R.V_2.\sin\delta\Big)\end{aligned} \tag{A.12}$$

The AC transmission line is typically modelled with their inductances to be much higher than the resistance, thus by assuming $R \simeq 0$, the proper power equations are derived by rewriting (A.12) as:

$$\begin{aligned}P &= \frac{V_1.V_2}{X}.\sin\delta \\ Q &= \frac{V_1^2}{X} - \frac{V_1.V_2}{X}.\cos\delta\end{aligned} \tag{A.13}$$

Consequently, if the power angle δ is enough small, then we can approximate $\sin\delta = \delta$ and $\cos\delta = 1$, hence (A.13) is simplified and reformed into:

$$\begin{aligned}\delta &\cong \frac{X.P}{V_1.V_2} \\ V_1 - V_2 &\cong \frac{X.Q}{V_1}\end{aligned} \tag{A.14}$$

This demonstrates the fact that power angle depends on active power and voltage difference also depends on reactive power transmission.

Appendix B

B.1 Component Ratings and Parameters

The HESS rating and parameters are presented in the following tables, which separately reports the values for the DC side components, inverter and the AC side components. Moreover, all the control parameters and reference values are summarized in a separate table.

It must be noted that the system rating had been chosen according to the existing laboratory equipments which was also deployed in HESS model verification.

Table B.1: DC side component rating and parameter.

Component	Symbol	Value	Description
BESS	V_{bat}	320-460 V	voltage range
	RC	12 kWh	rated capacity
	P_{ch}	6.4 kW	rated charge-discharge power
	I_{ch}	16 A	rated charge-discharge current
PV	V_{mod}	37.6 V	nominal open circuit voltage
	P_{mod}	249.86 W	rated module power
	N_s	15	number of serial modules per string
	N_p	1	number of parallel modules per string
	C_{pv}	100 μF	PV output capacitor
	T_{STC}	25 °C	standard test condition temperature
	G_{STC}	1000 W/m^2	standard test condition irradiance
Boost Converter	L	5 mH	boost inductor
	R_s	5 $m\Omega$	inductor series resistance
Buck-Boost Converter	L	5 mH	buck-boost inductor
	R_s	5 $m\Omega$	inductor series resistance
DC Link	C	3 mF	DC link capacitor

Table B.2: Inverter rating.

Component	Symbol	Value	Description
PV Input Data	P_{max-pv}	6.5 kW	max PV input power
	I_{max}	16 A	max input current
	V_{dc}	150-1000 V	input voltage range
	V_{dc-r}	595 V	rated input voltage
	V_{MPPT}	320-800 V	MPPT voltage range
BESS Input Data	depends on BESS rating presented in previous table		
Output Data	P_{out-r}	5 kW	rated AC output power
	P_{max}	5 kVA	max AC apparent power
	V_{dc}	150-1000 V	input voltage range
	V_{ac}	3ph 380-400/220-230 V	output AC voltage range
	f	45-65 Hz	frequency range
	$Iac - r$	7.2 A	rated AC output current
	$\cos(\phi)_{ac-r}$	0.85-1	power factor range

Table B.3: AC side components rating and parameter.

Component	Symbol	Value	Description
Grid Filter	L	17.4 mH	filter inductance
	R_s	8.23 $m\Omega$	inductor series resistance
LV Grid	Vp	14.4 kV	transformer primary voltage
	V_s	220 V	transformer secondary voltage
	$P_{trans-r}$	450 kVA	transformer rated power

Table B.4: Controllers and algorithms settings.

Component	Symbol	Value	Description
P&O MPPT	D_{init}	0.5	initial duty cycle output
	D_{min}	0.3	minimum duty cycle output
	D_{max}	0.8	maximum duty cycle output
	ΔD	0.0003	duty perturbation step-size
	$fs - MPPT$	200 Hz	MPPT sampling frequency
IC MPPT	D_{init}	0.5	initial duty cycle output
	$fs - MPPT$	200 Hz	IC sampling frequency
Boost Converter	$f_{sw-boost}$	1 kHz	boost switching frequency
Buck-Boost Converter	$f_{sw-BBBC}$	1 kHz	buck-boost switching frequency
BESS CDC	k_i	1	CDC integrator constant
	k_p	16	CDC proportional constant
	bw_{CDC}	200 Hz	bandwidth
DCVC	k_i	94000	DCVC integrator constant
	k_p	942	DCVC proportional constant
	bw_{DCVC}	1 kHz	bandwidth
DCC	k_i	94000	DCC integrator constant
	k_p	942	DCC proportional constant
	bw_{DCC}	40 Hz	bandwidth
NPC Inverter	f_{sw-inv}	100 kHz	inverter switching frequency
ICC	k_i	0.4713	ICC integrator constant
	k_p	1097	ICC proportional constant
	bw_{ICC}	10 kHz	bandwidth
GFVR and GPIA	k_i	800	GFVR and GPIA integrator constant
	k_p	0.75	GFVR and GPIA proportional constant
	$bw_{GFVR\&GPIA}$	8 Hz	bandwidth
BRCG	f_{s-BRCG}	40 Hz	BRCG sampling frequency
GPMU	f_{s-GMPU}	8 Hz	GMPU sampling frequency

B.2 Overall HESS Power Flow Response

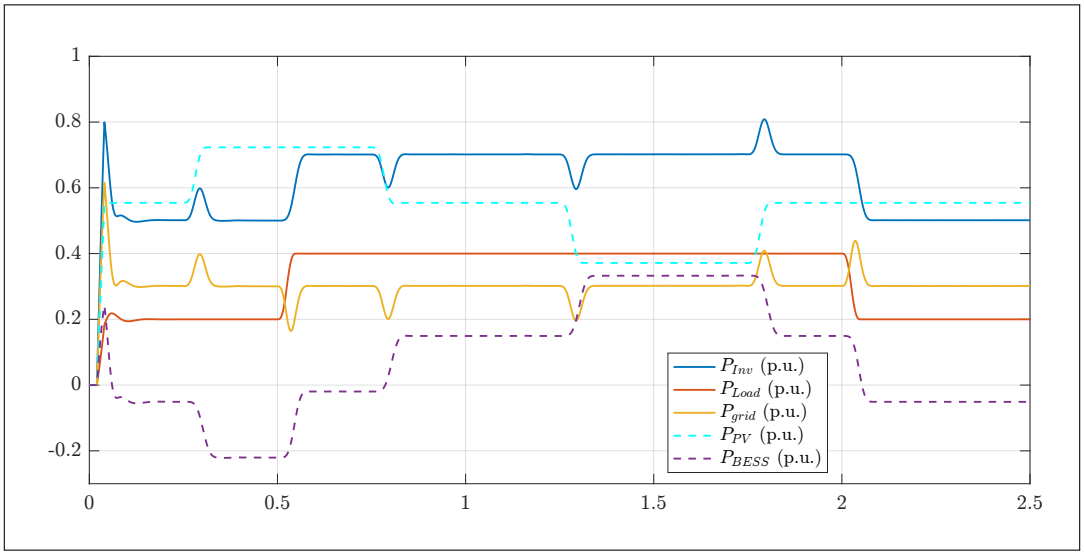

Figure B-1: HESS overall power flow response step-wise load demand.

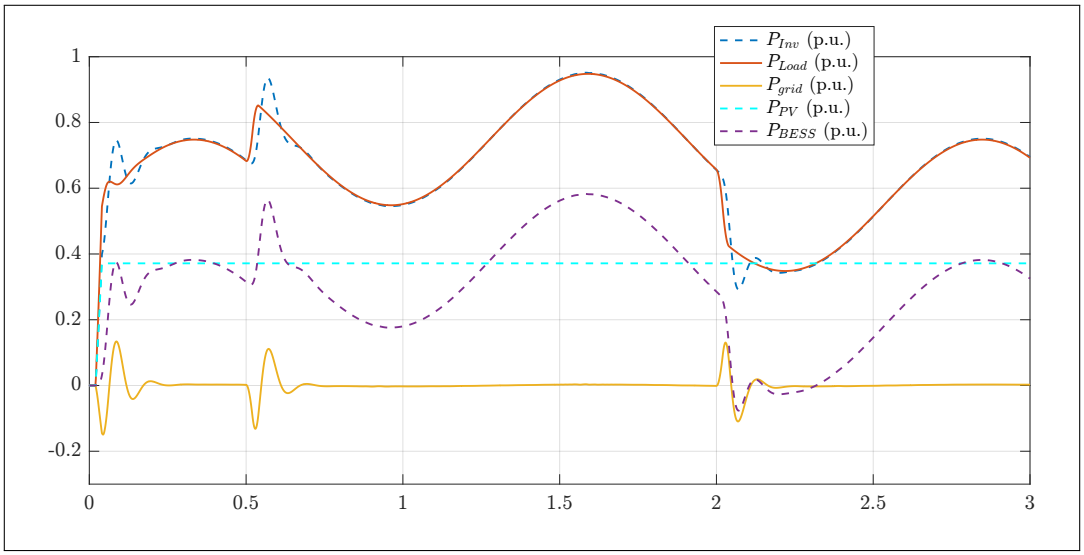

Figure B-2: HESS overall power flow response dynamic unbalanced load demand.

B.3 Laboratory Test Setup

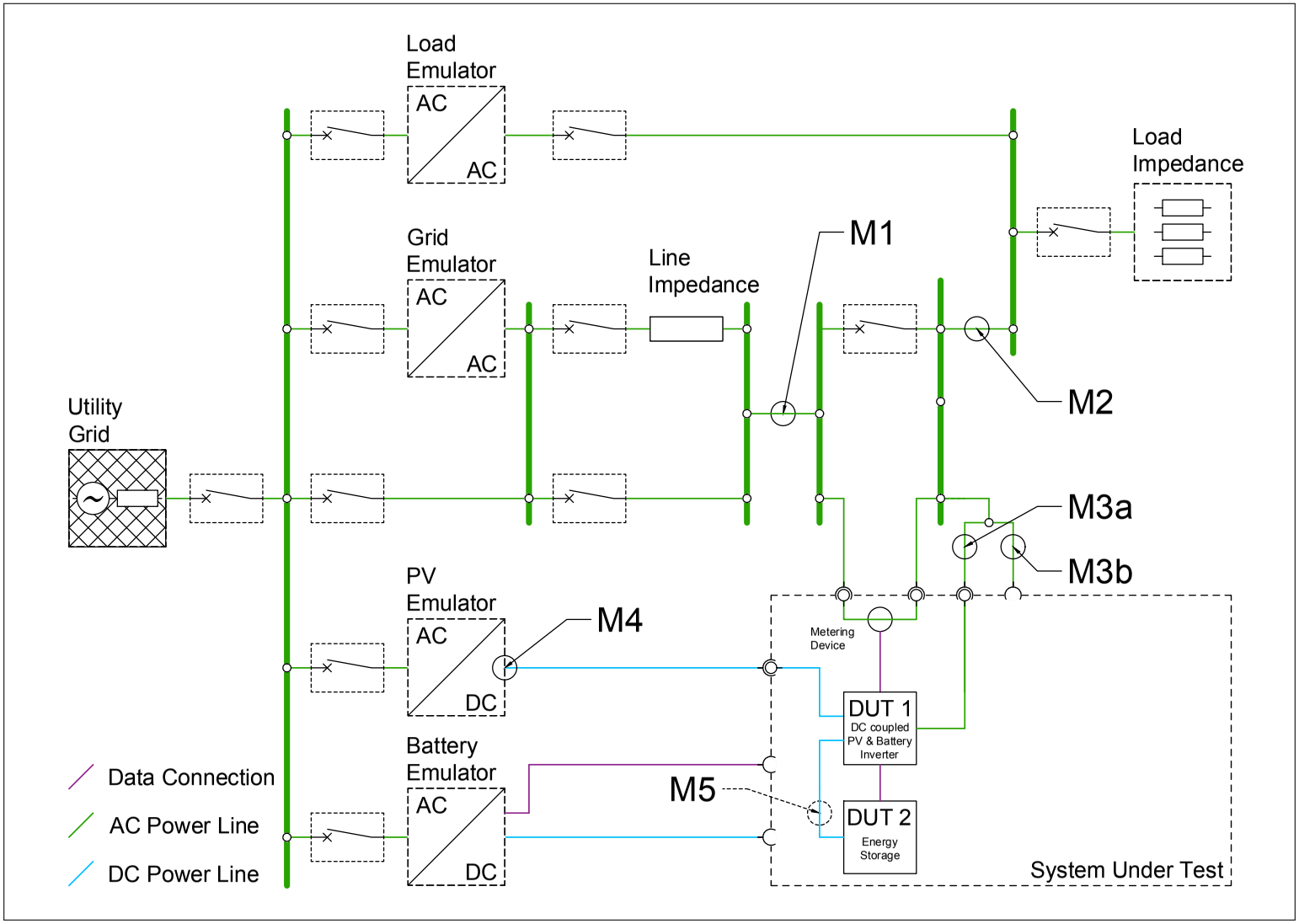

Figure B-3: Laboratory test setup. (AIT, 2016)

Bibliography

[1] Nicola Femia, Giovanni Petrone, Giovanni Spagnuolo, and Massimo Vitelli. *Power Electronics and Control Techniques for Maximum Energy Harvesting in Photovoltaic Systems*. CRC Press, December 2012. ISBN 978-1-4665-0691-6.

[2] M. C. Mira, A. Knott, O. C. Thomsen, and M. A. E. Andersen. Boost converter with combined control loop for a stand-alone photovoltaic battery charge system. pages 1–8, June 2013.

[3] M. Z. Daud, A. Mohamed, M. Z. Che Wanik, and M. A. Hannan. Performance evaluation of grid-connected photovoltaic system with battery energy storage. pages 337–342, December 2012.

[4] O. Tremblay, L. A. Dessaint, and A. I. Dekkiche. A Generic Battery Model for the Dynamic Simulation of Hybrid Electric Vehicles. pages 284–289, September 2007.

[5] W. Xiao, W. G. Dunford, P. R. Palmer, and A. Capel. Regulation of Photovoltaic Voltage. *IEEE Transactions on Industrial Electronics*, 54(3):1365–1374, June 2007. ISSN 0278-0046.

[6] Junhong Zhang. *Bidirectional DC-DC power converter design optimization, modeling and control*. PhD thesis, Virginia Polytechnic Institute and State University, 2008.

[7] Dong Ho Lee, S. R. Lee, and F. C. Lee. An analysis of midpoint balance for the neutral-point-clamped three-level vsi. 1:193–199 vol.1, May 1998. ISSN 0275-9306.

[8] A. Yazdani and R. Iravani. *Voltage-Sourced Converters in Power Systems: Modeling, Control, and Applications*. Wiley, 2010. ISBN 9780470551561.

[9] A. Reznik, M. G. Simões, A. Al-Durra, and S. M. Muyeen. Filter design and performance analysis for grid-interconnected systems. *IEEE Transactions on Industry Applications*, 50(2):1225–1232, March 2014. ISSN 0093-9994.

[10] M. K. Mishra, A. Joshi, and A. Ghosh. Control schemes for equalization of capacitor voltages in neutral clamped shunt compensator. *IEEE Transactions on Power Delivery*, 18(2):538–544, April 2003. ISSN 0885-8977.

[11] A. Timbus, M. Liserre, R. Teodorescu, and F. Blaabjerg. Synchronization methods for three phase distributed power generation systems - an overview and evaluation. pages 2474–2481, June 2005. ISSN 0275-9306.

[12] E. Adzic, M. Adzic, J. Tomic, and V. Katic. Improved phase-locked loop for distributed power generation systems. pages 323–328, Sept 2011. ISSN 1949-047X.

[13] R. Teodorescu and M. Liserre. *Grid Converters for Photovoltaic and Wind Power Systems*. Wiley - IEEE. Wiley, 2011. ISBN 9781119957201.